GFZ

POTSDAM
Helmholtz-Gemeinschaft

A.G. Pavelyev,
J. Wickert, T. Schmidt, V.N. Gubenko,
S.S. Matyugov, A.A. Pavelyev, V.A. Anufriev

Innovative technique for global control of layered and wave structures in the atmosphere and ionosphere by use of the CHAMP and FORMOSAT-3/COSMIC GPS radio occultation data base

Scientific Technical Report STR08/04

DOI:10.2312/GFZ.b103-08040

Imprint

GeoForschungsZentrum Potsdam
a Helmholtz Centre

Telegrafenberg
D-14473 Potsdam

e-mail: postmaster@gfz-potsdam.de
www: http://www.gfz-potsdam.de

Printed in Potsdam, Germany
April 2008

ISSN 1610-0956

This text is available in electronic form:
http://www.gfz-potsdam.de/bib/zbstr.htm

DOI:10.2312/GFZ.b103-08040

A.G. Pavelyev, J. Wickert, T. Schmidt,

V.N. Gubenko, S.S. Matyugov, A.A. Pavelyev, V.A. Anufriev

INNOVATIVE TECHNIQUE FOR GLOBAL CONTROL OF LAYERED AND WAVE STRUCTURES IN THE ATMOSPHERE AND IONOSPHERE BY USE OF THE CHAMP AND FORMOSAT-3/COSMIC GPS RADIO OCCULTATION DATA BASE

Final report 2007 of a research contract between the

INSTITUTE OF RADIO ENGINEERING AND ELECTRONICS OF THE

RUSSIAN ACADEMY OF SCIENCES (IRE RAS), Moscow

and

GeoForschungsZentrum Potsdam (GFZ)

Scientific Technical Report STR 08/04

2008

DOI:10.2312/GFZ.b103-08040

CONTENTS

DOI:10.2312/GFZ.b103-08040

DOI:10.2312/GFZ.b103-08040

INTRODUCTION

The report contains a description of main results obtained within the research contract between IRE RAS and GFZ Potsdam and results of investigation during period November-December 2007 – the third stage of the contract. The objectives of investigation included (1) elaboration and verification of an innovative phase acceleration-refraction attenuation technique to locate layered and wave structures in the ionosphere and atmosphere; (2) elaborating of a new technique for identification of wave origin of temperature and density fluctuations and determination of the intrinsic frequency of internal gravity waves in the Earth's stratosphere from radio occultation (RO) data; presentation of a technique for evaluating the vertical profiles of the phase, amplitude, horizontal wind perturbations, intrinsic phase speed, kinetic and potential energy of atmospheric waves; (3) maps of waves parameters in the ionosphere and atmosphere showing their regional, seasonal and diurnal variations with aim to establish connections with solar and meteorological activity.

The revealed possibility to measure the intrinsic frequency of internal gravity waves (from a single RO vertical profile of the refractivity (density) and/or temperature) is important for application of RO method to study the energy and kinetic momentum vertical fluxes associated with internal gravity waves at the different altitudes in the atmosphere.

In the first section a new method is introduced to locate layered structures in the ionosphere and atmosphere and establishing the origin of the RO signal scintillations observed at mesospheric and stratospheric altitudes in the trans-ionospheric satellite-satellite line. This method can be considered, in essence, as a radio-holographic because it allows one to obtain resolution ~ 100 km in the horizontal direction along the RO ray. This method is based on a connection between the phase path excess and intensity

DOI:10.2312/GFZ.b103-08040

changes in the GPS radio-holograms registered on board LEO satellite. An important useful feature of this connection consists in a possibility to separate influence of the absorption and refraction attenuation effects in the GPS radio-holograms by use of combined analysis of the amplitude and phase data. Two equations are obtained in section 1 which connect the amplitude and phase part of GPS radio-holograms. The first equation indicates equivalence between the variations of the phase path excess acceleration $a = d^2\Phi(t)/dt^2$ and refraction attenuation $X(t)$. The second equation connects the high-frequency part of the phase path excess variations $\Phi_l(t)$ with intensity changes $X(t)-1$ of the RO signal. Obtained relationships allow one to recalculate the normalized (relative to the free space level) intensity variations in GPS radio-hologram to the phase path excess variations and vice versa. It is also important that the form of the phase path excess variations $\Phi_l(t)$ is similar to the form of the intensity variations $X(t)-1$. The revealed connections between the phase and amplitude are validated in the first section by analysis of the CHAMP RO data.

In the second section a new technology is introduced for estimating of the internal waves parameters from RO signal scintillations. From one side this technique is based on the fundamental dispersion and polarization relationships with aim to find the horizontal wind perturbations and the intrinsic phase speed associated with internal gravity waves. From another side a new analysis technique is proposed to identify the observed fluctuations as wave-induced, assuming the gravity wave saturation condition. This technique is used for determination of the key parameter – the intrinsic frequency of gravity waves. This technique is based upon a comparison of the experimental and theoretical values of the relative amplitude threshold. The theoretical amplitude threshold, assuming a minimum Richardson number of 1/4, is a function of f/ω, where f and ω are the inertial and intrinsic frequencies, correspondingly. The theoretical

DOI:10.2312/GFZ.b103-08040

threshold values are confined from zero to unity. In the case, when this criterion is satisfied, and the analyzed fluctuations are identified as wave-induced, then the intrinsic frequency of a monochromatic gravity wave can be determined from a single occultation event. The results of determination of the intrinsic frequency and other characteristics of internal gravity waves, propagating in the Earth's stratosphere are presented and discussed.

In the third section the examples of the internal wave breaking at the altitudes between 38 and 50 km are presented in the first time for the RO practice. The maps of the geographical distributions and seasonal dependence of the atmospheric wave activity with global coverage for period 2001 – 2003 are presented. These data reveal an asymmetry in the distribution of the wave activity at the 12 km level in the atmosphere. The maximal wave activity occurs in the summer polar region. At the 14–16 km levels, the wave activity is centered in the moderate latitudes both in the Northern and Southern Hemisphere. At 18 and 20 km levels, most of the internal wave's activity is concentrated in the equatorial areas. The local seasonal dependences are clear for some regions, e.g., Siberia at the height of 14 km in the winter, with a low wave activity and a high wave activity in the summer.

In the forth section it is shown that the RO signal variations are indicator of plasma disturbances in the near-Earth space. The RO index of ionospheric activity R_i is introduced which is in good agreement with changes in the hourly index of *DST* related to the solar wind. The R_i index is equal to the ratio of the number of the RO events with the S_4 value, averaged at the altitudes above 40 km, and greater than the selected level, to the total number of RO events in the investigated area for a certain time interval (e.g., for a day). The maps of the geographical and seasonal distribution of the intense RO amplitude scintillations with high values of the index S_4, relevant to the time period

DOI:10.2312/GFZ.b103-08040

May 2001-July 2004, indicate the areas with intense ionospheric disturbances and demonstrate connection with solar activity. The analysis indicates importance of GPS RO studies for revealing of the interrelations between solar activity and natural processes in the ionosphere and mesosphere.

In conclusion the main results are given.

DOI:10.2312/GFZ.b103-08040

1. PHASE-REFRACTION ATTENUATION TECHNIQUE AND ITS VERIFICATION BY USE OF CHAMP RADIO OCCULTATION DATA

1.1. INVESTIGATION OF LAYERED STRUCTURES IN THE NEAR-EARTH SPACE: BACKGROUND

The origin of sporadic plasma structures in the near-Earth space are related to wave activity in the mesosphere, ionosphere, and mesosphere, effects of variations in the ionizing solar radiation at different wavelengths, and solar wind interaction with the Earth's magnetosphere [e.g., *Yizengaw et al.*, 2006]. Localization and estimation of the electron density distribution in the plasma disturbances in the ionosphere have been done previously by tomographic and radio-holographic methods by use of the radio signals in trans-ionospheric satellite-to-Earth links [*Kunitsyn and Tereshchenko*, 2003, and references therein]. The phase variations during propagation of the high-accuracy Global Navigation Satellite System (GPS) signals make it possible to sound the topside ionosphere/plasmasphere based on measurements from the Low Earth Orbiter (LEO) satellites [*Heise et al.*, 2002]. Therefore, the GPS/GLONASS satellite navigational system with more than 50 satellites, which are located in circular orbits with an inclination of about 70° and a height of ~20000 km above the ground surface and emit at wavelengths of 19 and 24 cm, makes it possible to globally observe the processes in the Earth's plasma sheath above the LEO satellite [*Yizengaw et al.*, 2005, 2006].

The radio signals emitted by GPS at two carrier frequencies (f_1= 1575.42 MHz and f_2= 1227.6 MHz) are currently used in radio occultation (RO) studies of the F- and E- layers below the LEO satellite [*Hajj and Romans*, 1998; *Schreiner et al.*, 1999; *Vorob'ev et al.*, 1999, *Wickert et al.*, 2001; *Gorbunov et al.*, 2002; *Sokolovskiy et al.*, 2002], and especially sporadic E-layers of the ionosphere [*Igarashi et al.*, 2001; 2002, *Hocke et al.*, 2001, 2002; *Pavelyev et al.*, 2002; 2003; *Wickert et al.*, 2004a, *Wu et al.*,

DOI:10.2312/GFZ.b103-08040

2005]. These investigations are concentrated on the ionospheric influence on highly precise GPS radio signals [*Pavelyev et al.,* 2005a,b, *Liou et al.,* 2005], and on the determination of the vertical distribution of electron density in the lower ionosphere as function of altitude [*Igarashi et al.*, 2001; 2002, *Hocke et al.*, 2001, 2002; *Pavelyev et al*., 2002; 2003; *Wickert et al*., 2004a]. The information on the electron density distribution in the lower ionosphere is important source for estimation of the off-equatorial height-integrated conductivity [*Kelley et al.*, 2004]. All these investigations are important for modernization of the published information on the morphology of the ionosphere and ionospheric processes [*Kelley*, 1989].

The RO technique differs significantly as compared with ionospheric tomography methods. The RO sounding is fulfilled from nearly constant direction in contrast with tomographic methods, which sound the propagation medium from different directions [*Kunitsyn and Tereschenko*, 2003]. In essence, the RO technique is designed for investigation of the layered structures in the propagation medium under an assumption of spherical symmetry. The electron density, found under the assumption of the spherical symmetry, is assigned to the tangent point *T* (ray perigee) on a ray trajectory *GTL* connecting the GPS and LEO satellites, practically coinciding at GPS frequencies with the projection *Q* of the center of spherical symmetry *O* on the line of sight *GQL* from GPS to LEO (Fig. 1.1) [*Hajj et al.*, 2002]. In general, the assumption of the spherical symmetry cannot be applied directly to locate sporadic ionospheric disturbances [*Wickert et al*., 2004a; *Pavelyev et al.,* 2005a, *Liou et al.,* 2005].

The investigations provided by *Wu et al*. [2005], *Pavelyev et al.* [2005b] and *Wickert et al.* [2004b], showed that the reasonable global morphology and occurrence of plasma disturbances and sporadic E_s-layers in the ionosphere may be produced on a monthly and seasonal basis by analysis of the phase and amplitude variations of the

DOI:10.2312/GFZ.b103-08040

CHAMP RO signal. However, it is unclear up until now how to estimate the location of the plasma layers in the lower ionosphere by the RO method [*Wickert et al.,* 2004a]. Apparently, a possibility of the RO method to locate the plasma disturbances depends on their type.

Gorbunov et al. [2002] and *Sokolovskiy et al*. [2002] applied the Back Propagation (BP) radio-holographic method for RO data analysis to locate ionospheric disturbances in the E- and F-layer of the ionosphere. *Wickert et al*. [2004a] introduced a new approach for estimation of the electron density in sporadic plasma structures in the ionosphere. This approach is based on the assumption of an inclined plasma layer. *Wickert et al*. [2004a] indicated a difficulty in evaluating the location of an inclined plasma layer and resolving uncertainty in its location between the parts GT and TL of the ray trajectory GTL (Fig. 1.1).

In this section we introduce a new method of locating the sporadic layered structures in the ionosphere and establishing the origin of the RO signal scintillations observed at the mesospheric and stratospheric altitudes in the trans-ionospheric satellite-satellite line. We demonstrate a relation between solar activity and variations in RO signal intensity by use of the CHAMP RO data.

1.2. INNOVATIVE PHASE – REFRACTION ATTENUATION TECHNIQUE FOR MEASURING PARAMETERS OF THE NEAR-EARTH SPACE BY USE OF RO DATA

The scheme of the radio occultation experiment in the trans-ionospheric satellite-to-satellite link is shown in Fig. 1.1. Radio waves emitted by the GPS satellite (point *G*) arrive at a receiver on board the LEO satellite (point *L*) along the ray *GTL*, where *T* is the tangent point in the atmosphere (or ionosphere). Point *O* is the center of the spherical symmetry of the Earth's atmosphere and ionosphere. Point *O* coincides with

DOI:10.2312/GFZ.b103-08040

the local center of curvature of the Earths surface (ellipsoid) in the plane *LGO* (Fig. 1.1) [*Hajj et al.*, 2002]. At point *T*, the direction *OT* is perpendicular to the ray *GTL*, and the gradient of refractivity *N(h)* is perpendicular to the ray trajectory *GTL* (Fig. 1.1). At point *T*, the ray's distance from the Earth's surface *h* is minimal. The projection of point *T* on the Earth's surface determines the coordinates of the RO region: latitude φ and longitude λ_l. Records of the RO signal *E(t)* along the LEO trajectory at two GPS frequencies f_1=1575.42 MHz and f_2=1227.6 MHz are two 1-D radio-holograms which contain the amplitudes $A_1(t)$ and $A_2(t)$, respectively, along the phase path excesses $\Phi_1(t)$ and $\Phi_2(t)$ of the radio field as functions of time.

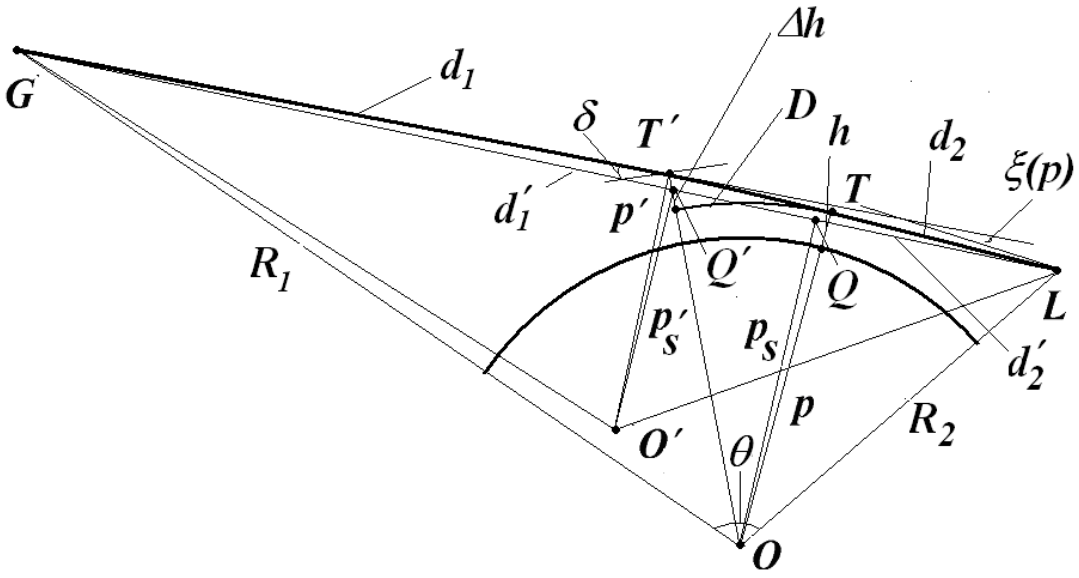

Fig. 1.1. Scheme of trans-ionospheric satellite-to-satellite link.

The vertical velocity of the occultation beam path $v_\perp$ is usually about 2 km/s in the RO experiments. This value of $v_\perp$ is many times greater than those corresponding to the motion of layers in the ionosphere and atmosphere. Therefore, the satellite radio-holograms contain quasi-instantaneous image of the Earth environment in the RO region. The radio-holographic methods elaborated by *Hocke et al.* [1999], *Igarashi et al.* [2000, 2001], *Pavelyev et al.* [2002, 2004], *Gorbunov* [2002] and *Jensen et al.* [2003] can be applied to the radio-holograms analysis with aim to obtain the vertical

DOI:10.2312/GFZ.b103-08040

resolution about of 60 m. In this report we introduce a new technique to obtain resolution in the horizontal direction, i.e. along the ray GTL (Fig. 1.1). This new technique can be applied for the case when one might account for the horizontal gradients in the ionosphere. To achieve this aim we will use a discovered connection between the phase and amplitude variations in the satellite radio-holograms.

According to existing RO technique the phase variations of the RO signal can be applied to determine the impact parameter *p* of the ray trajectory *GTL* and the bending angle $\xi(p)$ (Fig. 1.1) by use of known satellite trajectory data [*Hajj et al.*, 2002]. Then, the electron density $N_e(p)$ in the ionosphere and the vertical profiles of refractivity $N(p)$ in the neutral atmosphere can be determined by different methods based on the Abel transform [*Steiner et al.*, 1999; *Hocke et al.*, 2001; *Pavelyev et al.*, 2002, 2003; *Igarashi et al.*, 2002]. The altitude *h* of the point *T* can be determined from the known values of the Earth curvature radius a_e, impact parameter *p*, and refractivity $N(p)$ under assumption of spherical symmetry with the center at point *O* [*Hajj et al.*, 2002]. The amplitude variations of the RO signals are also used to determine the vertical gradient of the refractivity $dN(h)/dh$ and electron density $dN_e(h)/dh$ [*Igarashi et al.*, 2002; *Liou et al.*, 2002]. Note that at GPS frequencies the refractivity is small and the location of the point *T* in the upper atmosphere and ionosphere practically coincides with the projection of the center of spherical symmetry *O* on the line of sight direction *GL* – point *Q* (Fig. 1.1). Therefore, in the upper atmosphere and ionosphere the height *h* of the ray perigee *T* can be calculated directly by use of a known location of the spherical symmetry center *O* and trajectory data.

Horizontal gradients in the ionosphere can cause additional variations in the amplitude and phase of the RO signal and change the location of the center of spherical symmetry [*Wickert et al.*, 2004a]. As a consequence, one can observe significant

DOI:10.2312/GFZ.b103-08040

variations of the amplitude and phase of the RO signals in the 40–80 km altitude interval of the ray perigee *T*, in which the expected contributions from neutral gas or electron density in the RO signal changes are negligible at both GPS frequencies [*Sokolovskiy et al*., 2002; *Wu et al*., 2005]. *Wickert et al*. [2004a] introduced a hypothesis that the origin of intense variations in the amplitude of the RO signal in this altitude interval of the ray perigee can be related to the influence of the inclined layered structures, which displaces the tangent point on a ray path trajectory *GTL* (Fig. 1.1) to a new position *T′*. The new location of the tangent point (Fig. 1.1) can appear as a result of the effect of regular horizontal gradients in the ionospheric *E*- and *F*-regions and, possibly, in the lower magnetosphere. At a new tangent point *T′*, located at a distance *D* relative to point *T*, the intense refractivity gradient in the inclined layered structure is perpendicular to the ray *GTL*, and the height *h* is changed by magnitude $\Delta h = D^2/r$, where *r* is the distance *OT* [*Wickert et al*., 2004a] (Fig. 1.1). The sign of the horizontal displacement *D* of point *T* is positive when the point *T′* is located between *T* and *G*, and is negative in the opposite case, when *T′* is located between *T* and *L* (Fig. 1.1). The elevation angle δ of the inclined structure relative to the local horizontal direction is equal to $\delta = D/r$ (Fig. 1.1).

Radio wave propagation in the inclined layered structures can be described by a model of locally spherical symmetric layer [*Pavelyev et al.*, 1996], which relates the amplitude and phase variations in different sections of a ray path of the RO signal with parameters of the near-Earth medium. According to this model, the phase path of the radio waves is more sensitive to long-scale variations in refractivity, whereas the amplitude is sensitive to the refractivity gradients at the tangent points on the RO signal trajectory. Despite the dependence on noise of a receiver and receiving antenna and variations in the emitted power and antennas gain, the RO signal amplitude is a

DOI:10.2312/GFZ.b103-08040

valuable source of information about characteristics of the near-Earth medium [*Sokolovskiy et al.*, 2002; *Liou et al.*, 2002].

To establish the origin of the amplitude scintillations in the 40–80 km height interval of ray perigee *T*, it is necessary to analyze the connections between the phase and amplitude variations of the RO signal. The radio-physical model of the locally spherical symmetric layer permits one to obtain an important connection between the phase and amplitude variations of the radio wave propagating through a layered medium [*Pavelyev et al.*, 1996, 1997, 2004]. To establish this connection, we will use the relations obtained formerly [*Pavelyev et al.*, 2002, 2004; *Liou et al.*, 2006] between the phase-path excess $\Phi(p)$ and the refraction attenuation X of the radio waves propagating in a spherical symmetric medium with the center of symmetry located in point O (Fig. 1.1)

$$\Phi(p)= L(p)+\kappa(p) - R_0 , \quad L(p) = d_1+ d_2+ p\xi(p), \tag{1.1}$$

$$X(p)=pR_0^2[R_1R_2\, d_1d_2\, \sin\theta\,/\,\partial\theta/\partial p\,/]^{-1}, \tag{1.2}$$

$$\partial\theta/\partial p=d\xi/dp-(1/d_1+1/d_2), \tag{1.3}$$

$$L(p) =(R_1^2-p^2)^{1/2}+(R_2^2-p^2)^{1/2}+p\xi(p),\ R_0 =(R_1^2-p_s^2)^{1/2}+(R_2^2-p_s^2)^{1/2}, \tag{1.4}$$

$$d_1=(R_1^2-p^2)^{1/2},\ d_2=(R_2^2-p^2)^{1/2}, \tag{1.5}$$

where $\kappa(p)$ is the main refractivity part of the phase path excess, $\xi(p)=-d\kappa(p)/dp$ is the refraction angle, $\theta(p)$ is the central angle, p, p_s are the impact parameter of the ray trajectory *GTL*, and the line of sight *GQL*, respectively, R_0 , R_1, R_2 are the distances *GL*, *OG*, and *OL*, correspondingly, $L(p)$ is the distance *GABL*, and d_1, d_2 are two short lengths: *GA* and *BL*, which are approximately equal to *GQ* and *QL* (Fig. 1.1). The refraction angle $\xi(p)$ is connected with the central angle θ (Fig. 1.1):

$$\theta=\pi+\xi(p)-\sin^{-1}(p/R_1)-\sin^{-1}(p/R_2),\ \theta=\pi-\sin^{-1}(p_s/R_1)-\sin^{-1}(p_s/R_2), \tag{1.6}$$

DOI:10.2312/GFZ.b103-08040

$$\xi(p)=\sin^{-1}(p/R_1)+\sin^{-1}(p/R_2)-\sin^{-1}(p_s/R_1)-\sin^{-1}(p_s/R_2) \quad (1.7)$$

Two different expressions (1.6) for the central angle θ can be used to obtain connections between the impact parameters p_s and p and the refraction angle $\xi(p)$. From equations (1.1) and (1.6), one can obtain by differentiation of the phase excess $\Phi(p)$ and the central angle θ on time the relationship connecting the Doppler frequency of the RO signal with the impact parameters p and p_s:

$$d\Phi(p)/dt=(p-p_s)d\theta/dt+(d_1-d_{1s})R_1^{-1}dR_1/dt+(d_2-d_{2s})R_2^{-1}dR_2/dt \quad (1.8)$$

$$d\theta/dt=\partial\theta/\partial p_s dp_s/dt-p_s[(d_{1s}R_1)^{-1}dR_1/dt+(d_{2s}R_2)^{-1}dR_2/dt],$$

$$d_{1s}=(R_1^2-p_s^2)^{1/2},\ d_{2s}=(R_2^2-p_s^2)^{1/2}, \quad (1.9)$$

where d_{1s} , d_{2s} are the distances GQ and QL, correspondingly, (Fig. 1.1). After substitution of the equation (1.9) in equation (1.8) one can obtain:

$$d\Phi(p)/dt=-(p-p_s)\{(1/d_{1s}+1/d_{2s})dp_s/dt+(p^2-p_s^2)\{R_1dR_1/dt[d_{1s}(d_{1s}+d_1)(pd_{1s}+p_sd_1)]^{-1}+$$

$$R_2dR_2/dt[d_{2s}(d_{2s}+d_2)(pd_{2s}+p_sd_2)]^{-1}\}\} \quad (1.10)$$

Equations (1.6) – (1.10) are valid for general case of the non-circular orbits of the GPS and LEO satellites. Equation (1.10) can be simplified under condition:

$$/(1/d_{1s}+1/d_{2s})dp_s/dt/>>/(p^2-p_s^2)\{R_1dR_1/dt[d_{1s}(d_{1s}+d_1)(pd_{1s}+p_sd_1)]^{-1}+$$

$$R_2dR_2/dt[d_{2s}(d_{2s}+d_2)(pd_{2s}+p_sd_2)]^{-1}\}/ \quad (1.11)$$

which is valid if $/(p-p_s)dR_{1,2}/dt/<<p_s/dp_s/dt/$. This inequality is valid for all practical RO situations. Under indicated approximation one can obtain from equation (1.10) a formula for estimation of the difference $p-p_s$ on the Doppler frequency $F_d=d\Phi(p)/dt$:

$$F_d=d\Phi(p)/dt=-(p-p_s)(1/d_{1s}+1/d_{2s})dp_s/dt \quad (1.12)$$

The values p_s, dp_s/dt, d_{1s} , d_{2s} can be delivered from the orbital data, and the phase delays $\Phi_{1,2}(p)$ are the objects of measurements and given in the phase parts of radio-holograms at frequencies f_1 and f_2. Therefore, one may obtain (after the ionospheric

DOI:10.2312/GFZ.b103-08040

correction) the dependence of the refraction angle ξ on the impact parameter p and then by use of an Abel inversion retrieve the vertical profiles of the refractivity $N(h)$, pressure $P(h)$, temperature $T(h)$, humidity $e(h)$ and electron density in the ionosphere $N_e(h)$ [Hajj, et al., 2002]. Below we will consider new relationships, which connect the phase acceleration $a=d^2\Phi(t)/dt^2$, Doppler frequency $F_d(t)$ and refraction attenuation of radio waves $X(t)$. Under conditions

$$|p-p_s| << p_s \tag{1.13}$$

$$|(p-p_s)d(\partial\theta/\partial p_s)/dt| << |(dp/dt-dp_s/dt)\cdot\partial\theta/\partial p_s|, \tag{1.14}$$

by use of equation $dp/dt-dp_s/dt \approx [X(t)-1]dp_s/dt$ (*Liou et al.*, 2006), one can obtain from (1.12):

$$1-X(t)=ma, \tag{1.15}$$

$$1-X(t)=mdF_d(t)/dt, \tag{1.16}$$

$$m=q/(dp_s/dt)^2, \tag{1.17}$$

$$q=d_1d_2/(d_1+d_2),\ d_1+d_2=R_0. \tag{1.18}$$

Equations (1.15), (1.16) indicate equivalence between the variations of the phase path excess acceleration a, derivative of the Doppler frequency $F_d(t)$, and refraction attenuation $X(t)$. Usually parameters m and dp_s/dt are known from the orbital data because the location of the spherical symmetry centre O and its projection on the line of sight – point Q are known, and the distance GT d_1 and TL d_2 can be easily estimated as $d_{1,2}=(R_{1,2}^2-p^2)^{1/2}$ (Fig. 1.1). Therefore, equation (1.15) gives a possibility to recalculate the phase acceleration a to the refraction attenuation X_a. This is useful for excluding the systematic errors from the phase and/or amplitude data, and for the estimation of the absorption in the atmosphere. The refraction attenuation X_a is determined from the amplitude data as a ratio of the intensity of radio signal propagating through the atmosphere $I_a(t)$ to its intensity in free space I_s:

DOI:10.2312/GFZ.b103-08040

$$X_a(t)=I_a(t)/I_s \qquad (1.19)$$

Thus, the experimental value X_a contains both the refractive and absorption contributions. However, the phase acceleration depends on the refraction effect only. This gives a possibility to determine the absorption in the atmosphere $Y(t)$ as a ratio:

$$Y(t)=X_a(t)/X_p(t),\ X_p(t)=1-ma, \text{ or } X_p(t)=1-mdF_d(t)/dt. \qquad (1.20)$$

This possibility is a high practical importance because in future satellite RO missions the measurement of the absorption effects due to water vapor and minor atmospheric gas constituents is planed, and the difficulties will consist of removing the refraction attenuation effect from the amplitude data. Equation (1.21) indicates the feasible way to solve this problem. Also the relationship (1.21) may be useful for estimation the conditions for communication in the Ku/K bands between two LEO satellites in a radio occultation geometry [*Martini et al.*, 2006].

In reality the phase variations of the RO signal as function of time $\Phi(t)$ at each GPS frequency f_1 and f_2 contain slowly and quickly changing parts $\Phi_u(t)$ and $\Phi_l(t)$:

$$\Phi(t)=\Phi_u(t)+\Phi_l(t) \qquad (1.21)$$

After substitution of formula (1.21) in equation (1.15) one can obtain:

$$1-X(t)=m[d^2\Phi_u(t)/dt^2+d^2\Phi_l(t)/dt^2]\approx m\,d^2\Phi_l(t)/dt^2, \qquad (1.22)$$

Equation (1.22) is valid under condition:

$$|d^2\Phi_u(t)/dt^2|<<|d^2\Phi_l(t)/dt^2|,$$

which is fulfilled because the influence of irregularities in the atmosphere and ionosphere is far below the effect of the standard atmosphere (or ionosphere) near the ray perigee. The vertical velocity of the RO beam is about 2 km/s this value is many times greater than the speed of layered structures in the ionosphere and atmosphere. Thus the layered structures in the atmosphere and lower ionosphere can be detected because high frequency modulation of the phase $\Phi_l(t)$. Therefore in the case of the

DOI:10.2312/GFZ.b103-08040

wave structures in the atmosphere and ionosphere one can consider their contribution to the phase excess variations as quasi-periodical process and presenthe second derivative $d^2\Phi_l(t)/dt^2$ in the form:

$$d^2\Phi_l(t)/dt^2 \approx -\omega_0^2\Phi_l(t),\ \omega_0^2 = 4\pi^2 v_\perp^2/\lambda_v^2, \qquad (1.23)$$

where $v_\perp$ – is the vertical velocity of the RO ray near the perigee T (Fig.1), ω_0^2 – is the parameter, depending on the vertical structure of the lower ionosphere (or atmosphere). Parameter ω_0^2 may be presented for the case of quasi-periodical layered structure having the vertical period λ_v in the form:

$$\omega_0^2 = 4\pi^2 v_\perp^2/\lambda_v^2. \qquad (1.24)$$

After substitution of expressions (1.23), (1.24) in equation (1.15) with accounting for relations (1.17) and (1.18) one can obtain:

$$X(t)-1 = c_0\Phi_l(t),\ c_0 = m\omega_0^2,\ c_0 = k_v^2 q,\ k_v^2 = 4\pi^2/\lambda_v^2,\ q = d_1 d_2/R_0, \qquad (1.25)$$

where c_0 – is the coefficient depending on the vertical structure of the ionosphere or atmosphere near the ray perigee, k_v is the vertical wave number of the vertical quasi-periodical structure in the ionosphere (atmosphere), d_1, d_2 are the distances along the ray TLG from the point L and G up to the ray perigee T, respectively, R_0 is the distance GL (Fig. 1.1). Equation (1.25) connects the high-frequency part of the phase path excess variations $\Phi_l(t)$ with intensity changes $X(t)-1$ of the RO signal. It is important that equation (1.25) allows one to recalculate the intensity variations of the GPS radio-holograms to the phase path excess variations and vice versa. It is also important that the form of the phase path excess variations $\Phi_l(t)$ is similar to the form of the intensity variations $X(t)-1$. One can estimate parameter c_0 by comparison of the amplitude and phase variations of RO signal, and then it is possible by use of trajectory data to find the vertical size of the layered structure. It follows from equations (1.24) and (1.25) that variations of the intensity of RO signal are proportional to the phase

DOI:10.2312/GFZ.b103-08040

path excess oscillations and inversely proportional to the second power of the vertical period of layered structure.

As follows from our analysis the practical algorithm for revealing the contribution of the lower ionosphere in the phase data can be described by equation:

$$\Phi_l(t)=\Phi(t)-<\Phi(t)>, \quad (1.26)$$

where $<\Phi(t)>$ denotes the trend in the phase data connected with influence of the regular vertical refactivity profiles in the atmosphere or upper ionosphere. Alternative approach to find $<\Phi(t)>$ consists in averaging of the phase path excess over a sliding interval, the size of the sliding averaging interval must be long enough to account for the long-scale influence of the atmosphere or upper ionosphere.

At the GPS frequencies, the absorption effect in RO experiment caused mainly by the atmospheric oxygen is about 2-3 db in the lower troposphere and is small in the upper troposphere and stratosphere. Therefore equations (1.15)-(1.17) are useful to control the deflections from the spherical symmetry by use of a joint analysis of the amplitude and phase variations in the RO signal. Note, that equations (1.15) – (1.18) are valid for a general case when the horizontal gradients in the ionosphere displace the tangent point T by distance D from its standard position to T′ and the local center of spherical symmetry from O to O′ (Fig. 1).

Equation (1.15) describes important connection between the variations of the phase path excess acceleration $a= d^2\Phi(t)/dt^2$ and refraction attenuation $X(t)$. Usually during RO experiments parameter m (eq. (1.17), (1.18)) is a slowly changing function of time. Parameter dp_s/dt can be found from trajectory data, describing the motions of the GPS and LEO satellites relative to the center of spherical symmetry – point O (Fig. 1):

$$dp_S/dt=v+(w-v)d_{1S}/R_0, \quad (1.27)$$

DOI:10.2312/GFZ.b103-08040

where v, w are the velocity components of the GPS and LEO satellites, respectively, which are perpendicular to the straight line GL in the plane GOL. The components v, w are positive when oriented in direction to the point O and are negative in the opposite case. In principle equations (1.15)-(1.18) can be used to find the distance LT d_{2s} from simultaneous observation of the phase and intensity variations of radio wave. To achieve this, one can find m from (1.15) as a ratio of the intensity changes to the phase acceleration variations and then the distance d_{2S} can be evaluated from the relationship:

$$d_{2S}=2mw^2[1+2\beta(v/w-1)+(1-4\beta v/w)^{1/2}]^{-1},\ \beta=mw^2/R_0, \tag{1.28}$$

Relation (1.28) is a cornerstone for location of the tangent point T (or locally spherical symmetric layers) in the propagation medium.

Therefore, if the magnitude m will be estimated from the experimental data, it is possible to find the new value of distance $T'L$ d_2' and thus to locate the new tangent point T' relative to the point T (or L). For the determination of the parameter m from the experimental data, we can assume that the value m is a slowly changing function of time. If the noise is very small, the averaging is not necessary and the parameter m can be determined directly from equation (1.15) as a ratio:

$$m=[1-X(t)]/a. \tag{1.29}$$

In the presence of noise, the value $m(t_k)$ corresponding to some instant of time t_k can be determined as a ratio of average of the squared refraction attenuation and phase acceleration variations:

$$m(t_k)=\{\sum_{i=k-M}^{i=k+M}[X(t_i)-1]^2/\sum_{i=k-M}^{i=k+M}[a(t_i)]^2\}^{1/2}, \tag{1.30}$$

DOI:10.2312/GFZ.b103-08040

where $2M$ is a number of samples for averaging, and $X(t_i)$, $a(t_i)$ are the current values of the refraction attenuation and phase acceleration variations, respectively, at the time instant t_i. Equation (1.30) is valid if there is a full correlation between the refraction attenuation and the phase acceleration according to equation (1.15). In real conditions, there are different sources of amplitude and phase variations of the RO signal (e.g. turbulence, multipath propagation, etc), which do not obey equation (1.15). However, the amplitude and phase variations corresponding to the inclined layered structures in the atmosphere and ionosphere may obey relationship (1.15). Then, the parameter m can be determined from a correlation relationship:

$$m(t_k)=\sum_{i=k-M}^{i=k+M}[1-X(t_i)]a(t_i)/\sum_{i=k-M}^{i=k+M}[a(t_i)]^2. \qquad (1.31)$$

Relationship (1.31) describes parameter m as the correlation coefficient between the refraction attenuation $X(t_i)-1$ and the phase acceleration $a(t_i)$.

Equations (1.30) and (1.31) give different estimations for parameter m, respectively. Then, by use of equation (1.28), one can estimate the displacement $D=d_2'-d_2=d_2'-(R_2^2-p^2)^{1/2}$. In the case of full correlation between the refraction attenuation and phase acceleration, the influence of the layered structures prevails, the magnitudes of the parameter m and displacement D can be evaluated exactly.

1.3. ORIGIN OF THE AMPLITUDE AND PHASE VARIATIONS

A description of the CHAMP RO mission is given in various publications [e.g., *Wickert et al., 2001*]. The data archives used in this work may be accessed at: http://isdc.gfz-potsdam.de/champ. Results of the CHAMP RO measurement of the phase and amplitude of the GPS signals are shown in Fig. 1.2 for the RO event № 0001, September 21, 2003, at 13 h 21 m of local time with the geographical coordinate 83.4° S latitude and 161.8° W longitude. The height h of point T evaluated from a standard

DOI:10.2312/GFZ.b103-08040

model of the Earth atmosphere [*Pavelyev et al.,* 1996] is depicted on the horizontal axis in Fig. 1.2. The plotted points correspond to sampling frequency 50 Hz. The height-sampling interval is about 30 m, depending on the vertical RO beam velocity. The curves 1 and 2 indicate

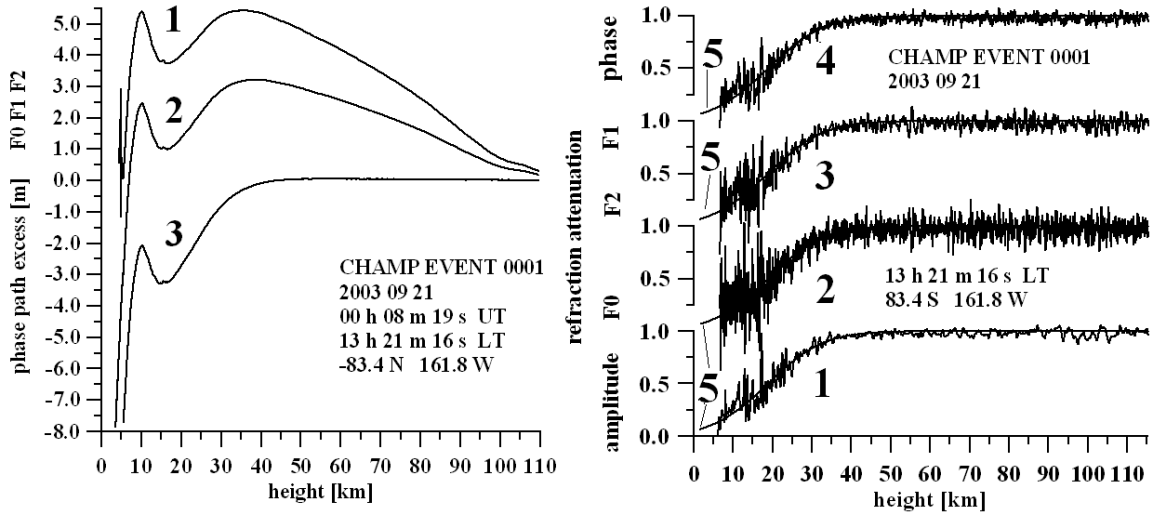

Fig. 1.2. An example of the CHAMP measurements. Left panel: the phase path excess residuals F1 and F2 as functions of height (curves 1 and 2, respectively). The phase path excess residuals F1 and F2 have been calculated by subtracting the phase excess evaluated by use of the refractivity model of the neutral atmosphere from the measured phase excesses F1 and F2. The phase path excess residual F0 (curve 3) has been obtained after ionospheric correction, i.e. after excluding the ionospheric influence by a linear combination of the phase path excesses residuals at the frequencies F1 and F2. Right panel: the refraction attenuation of the radio waves (curves 1–4) obtained from the amplitude (curve 1) and phase (curves 2–4) data. Smooth curves 5 indicate the result of modeling of the refraction attenuation by use of the refractivity model of the neutral atmosphere.

results of measurements of the phase path excesses at two GPS frequencies F2 and F1, respectively (Fig. 1.2, left panel). For a better comparison, the phase path excess calculated by use of the refractivity model [*Pavelyev et al.,* 1996] has been subtracted from the phase path excesses F1, F2, and F0 (curves 1 – 3 in Fig. 1.2, left panel). The phase path excess residual F0 (curve 3, Fig. 1.2, left panel) has been obtained after ionospheric correction, i.e., after excluding the ionospheric influence by linear combination of the phase path excesses residuals at the frequencies F1 and F2. The

DOI:10.2312/GFZ.b103-08040

phase residuals corresponding to the neutral gas (curve 3 in Fig. 1.2, left panel) are changing from −1 m at the 30 km altitude to −8 m at the 5 km altitude. These values correspond to a distinction of the vertical profile of refractivity in the polar atmosphere from the altitude profile of the refractivity used for simulation of the phase excess. Curve 1 in Fig. 1.2, right panel, demonstrates the refraction attenuation variations calculated by use of the amplitude data at the first GPS frequency F1. Curves 2–4 in the Fig. 1.2, right panel, indicate the results of estimating of the refraction attenuation by use of equation (1.15) from the phase excess data at the frequencies F2 and F1 (curve 3 and 4, respectively) and the phase excess data F0 obtained after ionospheric correction. For the calculation of the refraction attenuation from the phase excess data, the coefficient m in equation (1.15) has been evaluated using the satellites orbital data, which include the position and velocities of the GPS and LEO satellites relative to the center of spherical symmetry – point O (Fig. 1). Smooth curves 5 describe the results of modeling of the refraction attenuation. The good correspondence between the refraction attenuations obtained from the amplitude and phase data is seen in Fig. 1.2, right panel (curves 1–4). Also the results of modeling of the refraction attenuation coincide well with experimental data. Thus, we may conclude that relationship (1.15) is valid in the RO experiments up to altitudes about 30–40 km.

The relationship (1.15) opens a new way to measure the refraction attenuation in different kinds of RO experiments including the investigation of the planetary atmospheres. Thus, the phase acceleration has the same importance for the RO experiments as the well-known Doppler frequency. Note that by use of the phase data one can correct the amplitude data for systematic errors caused by the trends in the antenna gain and direction, and the receiver’s noise variations.

DOI:10.2312/GFZ.b103-08040

The interesting feature of the phase acceleration consists in the diminishing of the ionospheric influence. The slow ionospheric trend, which is clearly seen in Fig. 1.2 (left panel, curves 1 and 2), introduces a systematic error in the phase path excesses at the frequencies F1 and F2. This error is more than contribution of the neutral component in the upper stratosphere. However, the slow ionospheric trend is not prominent in the refraction attenuation (Fig. 1.2, right panel) because of the effect of double differentiation on time. The theoretical values of the refraction attenuation (curves 5 in Fig. 1.2, right panel), calculated without accounting for the ionospheric influence, agree with the experimental curves 1–4 obtained from the amplitude and phase data. In principle, this differential effect can be used to develop a new tool for ionospheric correction. However, this topic is beyond the scope of this report.

Below we will consider a possibility to use the relationship (1.15) to locate the tangent point *T* on the ray *GTL* (Fig. 1). When the RO beam moves through the lower stratosphere and troposphere, the location of the tangent point *T* is near to the projection *Q* of the center of the spherical symmetry – point *O* on the line of sight *GL* (Fig. 1). The position of point *T* in this case can be determined based on the known values of the impact parameters p and p_s assuming the center of spherical symmetry coinciding with point *O* (Fig. 1). However, when the RO beam is going through the mesosphere and upper stratosphere the vertical gradients corresponding to the influence of neutral component of the atmosphere are weak and the tangent point *T* can be displaced along the ray *GL* to zone where more significant gradients of the refractivity are perpendicular to the ray *GL*. This may occur because of the influence of the inclined plasma layers in the E- or F-layers of the ionosphere [*Wickert et al.*, 2004a,b]. In this case, the center of local spherical symmetry is displaced to point *O′* and its projection to the line of sight will be disposed at point Q′ (Fig. 1). The new location of the tangent

DOI:10.2312/GFZ.b103-08040

point will coincide with point T' at the distance D from tangent point T (Fig. 1). The value m in (1.15)–(1.18) depends on the distance D. Therefore, there exists a possibility to determine the distance D as a difference between the distance $Q'L$ and QL. The distance QL can be determined from the satellites orbital data. The distance $Q'L$ can be found from equation (1.28) by use of the experimental parameter m.

To check a possibility of measuring the distance D, we will consider the CHAMP data relevant to the equatorial RO events 0136 (January 14, 2003, at 14 h 40 m of local time at the geographical coordinate 3.2° S latitude and 3.8° E longitude) and 0023 (September 21, 2003, at 17 h 52 m of local time at the geographical coordinate 6.3° S

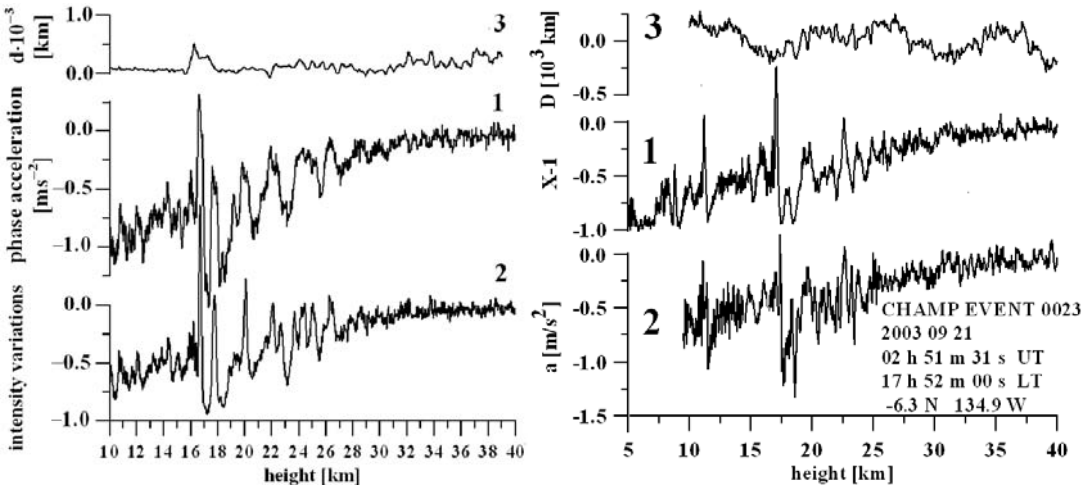

Fig. 1.3. Phase acceleration a and refraction attenuation $X–1$ at the first GPS frequency F1 (curves 1 and 2, respectively) for two CHAMP RO events: № 0136 on January 14, 2003 (left panel) and № 0023 on September 21, 2003 (right panel). The deflection of the point T along the ray TL from its standard location D is indicated by curves 3.

latitude and 139.4° W longitude), which are shown in Fig. 1.3 for the 10–40 km (left panel) and 5–40 km (right panel) height interval, respectively. The phase acceleration a calculated as the second temporal derivative of the phase-path excess and intensity variations $X–1$ at the frequency F1 are shown in Fig. 1.3 (curves 1 and 2, respectively). As seen in Fig. 1.3, there is a good correspondence between variations of the phase acceleration and intensity of the RO signal. The coefficient m is different in the RO

DOI:10.2312/GFZ.b103-08040

events № 0136 and № 0023. The average ratio of the refraction attenuation and the phase acceleration *m* is about 1.0 [m/s^2] in the 5–40 km height interval for the RO event 0136. This value *m* relevant to the event 0023 (Fig. 1.3, right panel) is about 1.5 times greater than that for the RO event 0136, January 14, 2003 (Fig. 1.3, left panel). This indicates that connection of the phase acceleration *a* and the refraction attenuation *X–1* (equation (1.15)) is valid in the RO measurements. Curve 3 in Fig. 1.3 indicates the deflection of point *T* from its standard location in the atmosphere. The deflections in the direction to point *G* or to point *L* are positive or negative, respectively. Deflection of point *T* in the 10–20 km interval of altitude from its standard position is small ~±150 km. This indicates the atmospheric origin of the phase and amplitude variations of the RO signal. At the altitudes above 30 km, one can see some displacements of point *T* connected with possible influence of the ionosphere (curve 3, Fig.3).

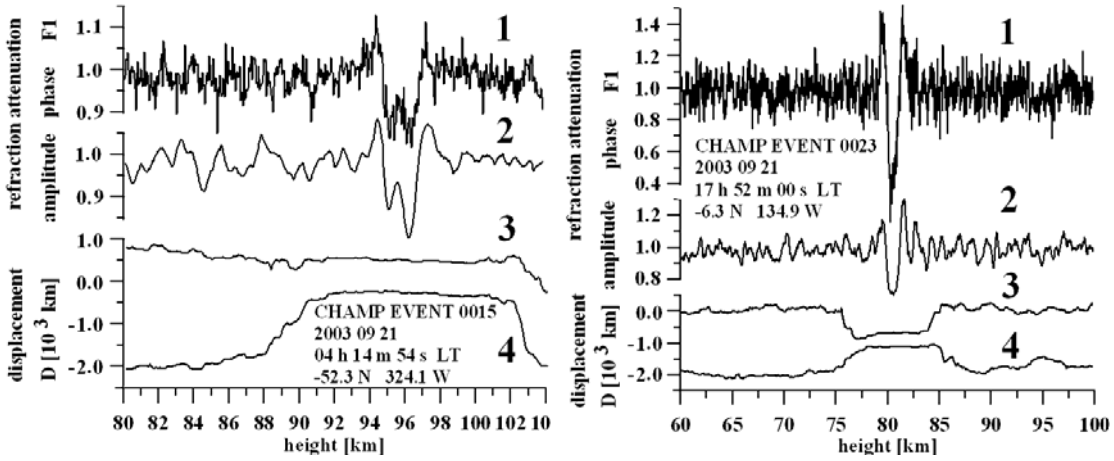

Fig. 1.4. Comparison of the refraction attenuation of the radio waves found from the phase and amplitude data (curves 1 and 2) with results of distance *D* estimation by use of equations (1.30) (curve 3) and (1.31) (curve 4) for the CHAMP RO event 0015, September 21, 2003 (coordinate 52.3 S, 324.1 W, 04 h 14 m 54 s LT) (left panel) and 0023, September 21, 2003 (coordinate 6.3 S, 134.9 W, 17 h 52 m 00 s LT) (right panel).

A correlation between the refraction attenuation and phase acceleration is clearly seen in the 10–30 km altitude interval as shown above. Slow regular changes of the refraction attenuation and phase acceleration introduce the main contribution to this

DOI:10.2312/GFZ.b103-08040

correlation. Below 10 km altitude, this correlation is destroyed by multipath propagation of the radio waves in the troposphere. Above 30 km altitudes, the ionospheric effect becomes important. Below we will consider a possibility to use the ionospheric effect to locate the ionospheric layers.

Table 1.1. Displacement D and correction Δh in the height of tangent point

Height h [km]	Distance D [km]	$\Delta h = d^2/2r$ [km]	Refraction attenuation (F1 phase data) X_p	Refraction attenuation (F1 amplitude data) X_a	Ratio m refraction attenuation /phase acceleration variations [s^2/m]
95.746	52.9	.21	.8987	.8956	.3762
95.700	9.3	.00	.9010	.9000	.3685
95.655	-26.5	.05	.9031	.9038	.3621
95.610	61.5	.29	.9096	.9065	.3776
95.564	8.6	.00	.9094	.9086	.3683
95.519	-121.7	1.15	.9051	.9102	.3452
95.474	43.5	.14	.9145	.9122	.3744
95.428	28.9	.06	.9143	.9127	.3718
95.383	-121.5	1.15	.9098	.9146	.3452
95.338	-14.5	.01	.9152	.9154	.3641
95.292	47.0	.17	.9201	.9179	.3749
95.247	-105.4	.86	.9179	.9216	.3480
95.201	-59.2	.27	.9239	.9256	.3561
95.156	64.9	.32	.9323	.9298	.3780
95.111	-179.1	2.50	.9317	.9373	.3349
95.065	-33.8	.08	.9428	.9434	.3605

The examples of the refraction attenuation recalculated from the amplitude and phase data are shown in Fig. 1.4 (curves 1 and 2) for the CHAMP RO event 0015, September 21, 2003 (coordinate 52.3 S, 324.1 W, 04 h 14 m 54 s LT) (left panel) and 0023, September 21, 2003 (coordinate 6.3 S, 134.9 W, 17 h 52 m 00 s LT) (right panel). The forms of the refraction attenuations X_a and X_p found from the amplitude and phase data are similar and indicated the ionospheric layers at the altitudes 95 km and 80 km (Fig. 1.4, left and right panels, respectively). The width of both ionospheric layers, as

DOI:10.2312/GFZ.b103-08040

estimated from curves 1 and 2 in Fig. 1.4, is about 2 km. The altitude 80 km is unusual for the ionospheric layers. Thus, in this case the location of the center of spherical symmetry is displaced and the altitude of the ionospheric layer must be recalculated. The results of estimation of the upper and lower boundaries for displacement D are indicated by curves 3 and 4, correspondingly, for the CHAMP RO events 0015 (Fig. 1.4, left panel) and 0023 (Fig. 1.4, right panel). For the event 0015, the upper and lower boundaries for displacement D near altitude 95 km are about 450 km and −500 km (curves 3 and 4, Fig. 1.5, left panel).

Near the center of layer at 95 km (Fig. 1.5, left panel), one can measure the parameter m without averaging by use of equation (1.29) and, then, find the displacement D from (1.28). The results of determination of the parameter m, displacement D and correction to the altitude of the layer Δh are given in the Table 1.1 as function of the altitude h of the point T. Also the refraction attenuations X_a and X_p calculated from the amplitude and phase data under assumption of the spherical symmetry with the center at point O (Fig. 1) are given in the Table 1.1. The refraction attenuations X_a and X_p are nearly equal, thus indicating the smallness of displacement D. The displacement D as seen from the second column of the Table 1.1 is changing in the −180 km - +65 km interval and the corresponding variations of correction to the altitude Δh in average are about 0.3 km. Therefore, results of direct measurement of the parameter m by use of equation (1.29) confirm the values of altitude of the sporadic E-layer at the height 95.5 km with displacement $D \sim -30$ km of point T' from standard position of point T corresponding to location of the center of spherical symmetry in the point O (Fig. 1).

The altitude 80 km observed in the event 0023 (Fig. 1.5, right panel, curves 1 and 2) is unusual for the center of the sporadic ionospheric layer. Thus, in this case, the location

DOI:10.2312/GFZ.b103-08040

of the center of spherical symmetry is displaced and the altitude of the ionospheric layer must be recalculated. The large difference (about two times) between the refraction attenuations X_a and X_p calculated from the amplitude and phase data under the assumption of the spherical symmetry with the center at point *O* (Fig. 1) (curves 1 and 2 in Fig. 1.5, right panel) supports this conclusion. The curves 3 and 4 (Fig. 1.5, right panel) indicate the displacement *D* in the interval from –600 km (upper boundary) to –900 km (lower boundary). A more careful investigation by use of equation (1.30) gives value *D* in the –680 km –630 km interval, and correction to the

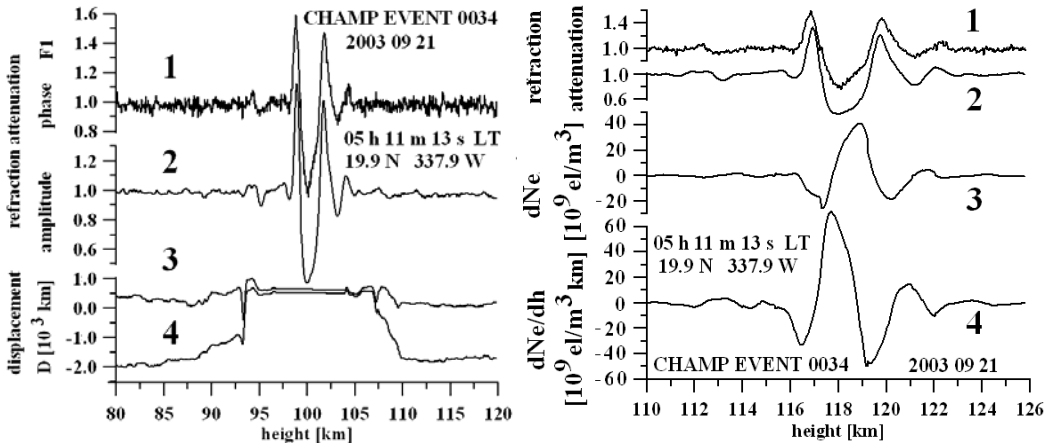

Fig. 1.5. Left panel: Comparison of the refraction attenuation of the radio waves found from the phase and amplitude data (curves 1 and 2) with results of distance *D* estimation by use of equations (1.30) (curve 3) and (1.31) (curve 4) for the CHAMP RO event 0034, September 21, 2003 (coordinate 19.9 N 227.9 W, 05 h 11 m 13 s LT) as function of the altitude of the ray perigee *T h*. Right panel: Comparison of the refraction attenuation of the radio waves found from the phase and amplitude data (curves 1 and 2) with results of estimation of the electron density and its vertical gradient variations as function of the real altitude of the sporadic E-layer $h+\Delta h$.

altitude Δh is about 30 km. Thus, the real height of the sporadic E-layer is about 110 km. The layer is displaced by 650 km to the receiver from the tangent point T (Fig. 1) and has inclination δ to the local horizontal direction of about 6º. The height of the sporadic E-layer is increased in the receiver direction. The lower boundary of the horizontal length of the sporadic E-layer L_e can be estimated from the relationship L_e

DOI:10.2312/GFZ.b103-08040

$\approx \Delta d/\delta$ where Δd is the layer width estimated on the dependence of the refraction attenuation on height. For the event 0023 (Fig. 1.5, right panel), the value $\Delta d \approx 3.5$ km and the horizontal length of the E-layer is greater than 35 km.

Another example of an intensive sporadic E-layer is given in Fig. 1.5, left panel (CHAMP RO event 0034, September 21, 2003, 05 h 11 m 13 s LT, 19.9 N 227.9 W). The curves 1 and 2 (Fig. 1.5, left panel) indicate the refraction attenuations X_a and X_p, respectively, as the functions of the altitude h of the ray perigee T (Fig. 1). The curves 3 and 4 demonstrate the upper and lower boundaries, respectively, for displacement D (Fig. 1.5, left panel). As seen in Fig. 1.5 (left panel), both minimums in the refraction attenuations found from the amplitude and phase data correspond to the height $h \approx 100$ km of the ray perigee T (Fig. 1). The upper and lower boundaries of the displacement D are nearly coinciding and equal to 500 km (curves 3 and 4, Fig. 1.5, left panel)). This value of the distance D corresponds to the location of the tangent point T' in the sporadic E-layer between the transmitter G and the ray perigee T (Fig. 1) at the altitude $h+\Delta h$ where $\Delta h \approx 18$ km. By use of the theoretical relationships published by *Liou et al.* [2006], it is possible to retrieve the variations of the electron density $dN_e(h)$ and its gradient $dN_e(h)/dh$ from the variations of the refraction attenuation, indicated by curves 1 and 2 in Fig. 1.5. Results of restoration of the electron density $dN_e(h)$ and its gradient $dN_e(h)/dh$ are shown in Fig. 1.5, right panel, by curves 3 and 4, respectively. The electron density variations are concentrated at the altitudes 116–120 km in the interval ± 30 [10^9el/m^3] and the vertical gradient of the electron density changes in the ± 60 [10^9el/m^{3}km] interval. The maximum in the electron density variation is about of 40 [10^9el/m^3] and is displaced by 1.5 km relative to the minimum of the refraction attenuation disposed at the 118 km altitude. The maximum in the vertical gradient of

DOI:10.2312/GFZ.b103-08040

the electron density is about 70 [10^9el/m^{3}km] and locates by 0.5 km below relative to the minimum of the refraction attenuation.

1.4. CONNECTION BETWEEN THE REFRACTION ATTENUATION AND PHASE VARIATIONS

As follows from our analysis the practical algorithm for revealing the contribution of the lower ionosphere in the phase data can be described by equation:

$$\Phi_l(t)=\Phi(t)-<\Phi(t)>, \tag{1.32}$$

where $<\Phi(t)>$ denotes the trend in the phase data connected with influence of the upper ionosphere. This trend can be find by linear or parabolic approximation of the phase data in the 40 – 130 km altitude interval. This approach was suggested by *Igarashi et al.*, 2000, and *Pavelyev et al.*, 2002 for analysis of wave structures in the upper ionosphere. Alternative approach to find $<\Phi(t)>$ consists in averaging of the phase path excess over a sliding interval, the size of the sliding averaging interval must be long

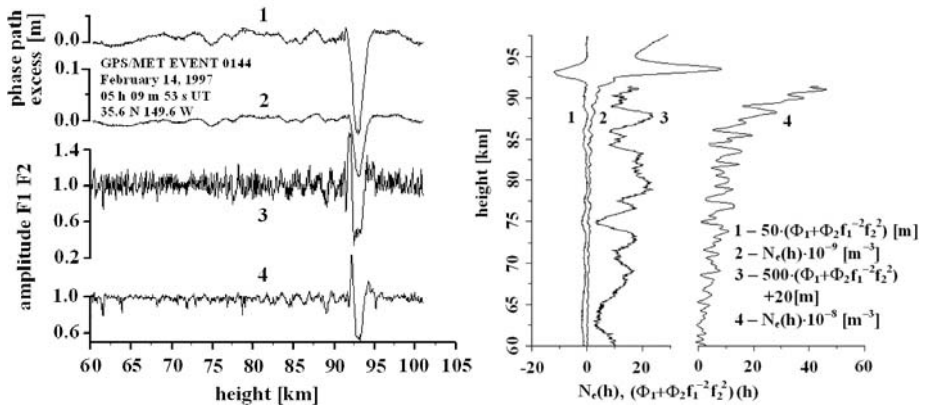

Fig. 1.6. Left panel: Comparison of the amplitude and phase path excesses at two frequencies f_1 and f_2. Curve 1 and 2 correspond to variations of the phase excess at frequency f_2 and f_1, respectively. Curve 3 and 4 describe the corresponding changes in the amplitude of RO signal at frequency f_2 and f_1, respectively. Right panel: Results of restoration of the vertical profile of electron density from phase data. Curve 1 and curve 3 correspond to combined value of the phase path excess Φ_1, Φ_2 calculated by use of formulas: $50\cdot(\Phi_1+\Phi_2 f_1^{-2} f_2^{2})$ [m], $500\cdot(\Phi_1+\Phi_2 f_1^{-2} f_2^{2})+20$ [m], respectively. Curve 2 and curve 4 describe to the vertical profile of the refractivity $N_e(h)\cdot 10^{-9}$ [m^{-3}] and $N_e(h)\cdot 10^{-8}$ [m^{-3}], correspondingly.

DOI:10.2312/GFZ.b103-08040

enough to account for the long-scale influence of the upper ionosphere. Results of application of formula (1.32) for finding connections between the amplitude and phase variations are shown in Fig. 1.6 for GPS/MET RO event with intense sporadic E-layer (February 14, 1997, latitude 35.6° N, longitude 149.6° W, 19 h 10 m LT). Comparison of the amplitude $A_{1,2}(t)$ and phase path excesses $\Phi_{l1,2}(t)$ at two frequencies f_1 and f_2 are shown in Fig. 1.6, left panel. The phase path excesses $\Phi_{l1,2}(t)$ corresponding to contribution of the lower ionosphere have been calculated by use of equation (1.32) from experimental data $\Phi_{1,2}(t)$ and parabolic approximation of the phase trends $<\Phi_{1,2}(t)>$, in the 60 – 105 km altitude interval. Curve 1 and 2 in Fig. 1.6 (left panel) correspond to variations of the phase excesses $\Phi_{l1,2}(t)$ at frequency f_2 and f_1, respectively. Curve 3 and 4 in Fig. 1.6 (left panel) describe the corresponding changes in the amplitude of RO signal at frequency f_2 and f_1, respectively. Comparison of the amplitude and phase variations in Fig. 1.6 (left panel) reveals their similarity in the 92-95 km altitude interval, which correspond to intense sporadic E-layer. Therefore these data indicate the practical importance of the revealed connection (1.25). Results of restoration of the vertical profile of electron density from phase data $\Phi_{l1,2}(t)$ by use of Abel transform are given in Fig. 1.6, right panel. Curve 1 and curve 3 correspond to combined value of the phase path excess Φ_1, Φ_2 calculated by use of formulas: $50\cdot(\Phi_1+\Phi_2 f_1^{-2} f_2^{2})$ [m], $500\cdot(\Phi_1+\Phi_2 f_1^{-2} f_2^{2})+20$ [m], respectively. Curve 2 and curve 4 describe to the vertical profile of the refractivity $N_e(h)\cdot 10^{-9}$ [m^{-3}] and $N_e(h)\cdot 10^{-8}$ [m^{-3}], correspondingly. As follows from Fig. 1.6, right panel, the maximum in the electron density $N_e(h) \approx 35\cdot 10^9$ [m^{-3}] is observed near the 93 km altitude. The data shown in Fig.

DOI:10.2312/GFZ.b103-08040

1.6 support and verify suggested method proposed for determination of the sporadic E-layer parameters.

2. DETERMINATION OF THE INTRINSIC FREQUENCY AND OTHER WAVE PARAMETERS FROM A SINGLE VERTICAL TEMPERATURE OR DENSITY PROFILE

2.1. PROBLEM STATEMENT

In order to examine internal gravity wave characteristics the small-scale fluctuations of normalized temperature in the Earth's stratosphere are analyzed by use of RO data. An analysis technique is proposed to identify the observed fluctuations with wave-induced ones, assuming gravity wave shear saturation. This technique is based upon a comparison of the experimental and theoretical values of the relative amplitude threshold which is defined as the wave amplitude required for shear instability. The theoretical amplitude threshold, assuming a minimum Richardson number of 1/4, is a function of f/ω, where f and ω are inertial and intrinsic frequencies, correspondingly. The theoretical threshold values are confined from zero to unity. In the case when this criterion is satisfied for its experimental counterpart and the analyzed fluctuations are positively identified as wave-induced, then the intrinsic frequency of the monochromatic gravity wave can be determined from only a single vertical temperature (or density) profile measurement. The results of the determination of the intrinsic frequency and other characteristics of internal gravity waves are presented and discussed.

Spectral characterization of the gravity wave field assumes that the wave field is composed of many components at various scales. Analysis of the temperature variations found from RO experiments allows to measure the statistical characteristics of internal waves in the atmosphere [*Steiner and Kirchengast,* 2000; *Tsuda et al.*, 2000; *Tsuda and Hocke,* 2002]. In many cases, however, the vertical profiles of temperature

DOI:10.2312/GFZ.b103-08040

or velocity exhibit only a single dominant wave structure over a certain altitude range. Evidence for a discrete or "narrow spectral", rather than a "broad spectral" description of the local wave field comes from many studies. Balloon, lidar, radar, and rocket data provide evidence of discrete events [*Fritts and Alexander*, 2003].

RO (RO) measurements of the altitude profiles of temperature or density in Earth's stratosphere can be used for the investigation of discrete wave structures. The advantages of RO observations are that this technique can furnish atmospheric profiles with global spatial coverage and high vertical resolution, and under all weather conditions. However, the observed temperature or density variations can alternatively be connected with internal gravity waves (IGW), turbulence, or stable layers. To extract conclusive results from these observations it is necessary to have an IGW identification criterion and to know the value of intrinsic frequency.

The aim of this section is to formulate the identification criterion for a low-frequency wave which saturates via shear instability. For a positively identified wave, an analysis technique to determine the intrinsic frequency and other wave parameters from a single temperature or density profile is proposed.

2.2. THEORETICAL RELATIONSHIPS

Assuming an adiabatic inviscid process and small scale motions, the perturbation equations for atmospheric motions can be derived from the fundamental equations for the atmospheric dynamics such as the equation of motion, first law of thermodynamics, continuity equation and equation of state for an ideal gas [*Fritts and Alexander*, 2003]. If a gravity wave is a plane wave, the dispersion relation of a gravity wave can be derived when $f^2 < \omega^2 < N^2$ and $m^2 >> 1/(4H^2)$, as follows:

DOI:10.2312/GFZ.b103-08040

$$\frac{\omega^2}{k^2+l^2} = \frac{N^2}{m^2} \cdot \frac{1-\omega^2/N^2}{1-f^2/\omega^2}, \tag{2.1}$$

where $H \simeq 7$ km is the scale height in the middle atmosphere, N is the Brunt-Vaisala, f the inertial, and ω the intrinsic frequency (frequency observed in the frame moving with the background flow) of the wave. The inertial frequency (the Coriolis parameter) f is defined as $f=2\Omega\cdot sin\phi$, where $\Omega = 7.292\cdot10^{-5}$ rad/s is the Earth rotation rate and ϕ is latitude. The intrinsic frequency can be written as $\omega = (k^2 + l^2)^{1/2} (c - \bar{u})$, where c is the horizontal phase velocity of the gravity wave and $\bar{u}$ is the horizontal mean wind speed in the direction of wave propagation. The parameters k, l and m represent the horizontal and vertical wavenumbers. We can make $l = 0$ by taking the x axis oriented along the direction of propagation of the wave.

The polarization relations for gravity waves can be derived from the basic equations as follows:

$$v' = -i \cdot \frac{f}{\omega} \cdot u' , \tag{2.2}$$

$$w' = -\frac{k}{m} \cdot u' , \tag{2.3}$$

where u' and v' are the complex perturbations for the parallel and perpendicular components of wave-induced horizontal wind relative to the wave propagation direction, w' is the complex perturbations for the wave-induced vertical wind. The prime ($'$) and the overbar denote the perturbation and mean quantities, respectively. There are simple relationships between the complex and real physical perturbations. For example, the real perturbation correspondent to u' is $Re\ u'$, and the real perturbation amplitude $|u'|$ is $[(Re\ u')^2+(Im\ u')^2]^{1/2}$. Equation (2.2) shows that the phase difference between u' and v' is 90°, and the ratio of amplitudes $|v'|/|u'|$ is proportional to

DOI:10.2312/GFZ.b103-08040

f/ω, indicating that the tip of the horizontal wind vector of a gravity wave draws an elliptical locus, and that the gravity wave is a transverse wave.

For an atmosphere in hydrostatic equilibrium where the fractional pressure fluctuations can be neglected relative to those in temperature and density, the amplitudes of normalized density and temperature perturbations can be computed from the ideal gas law and are approximately equal for a wave [*Gardner et al*., 1998]. For medium-frequency or low-frequency waves ($\omega^2 << N^2$), the following approximate polarization relations are simultaneously valid in this case [*Eckermann et al*., 1995]:

$$|u'| \approx \frac{g}{N} \cdot \frac{|\rho'|}{\overline{\rho}} \cdot \left(1 - f^2/\omega^2\right)^{-1/2} , \tag{2.4}$$

$$|u'| \approx \frac{g}{N} \cdot \frac{|T'|}{\overline{T}} \cdot \left(1 - f^2/\omega^2\right)^{-1/2} , \tag{2.5}$$

where $|\rho'|/\overline{\rho}$ and $|T'|/\overline{T}$ are the amplitudes of normalized density and temperature perturbations, respectively, and $|u'|$ is the horizontal velocity perturbation amplitude. The more detailed discussion of the restrictions connected with (2.4) and (2.5) can be found in the work of *Pavelyev et al.* [2004]. Observations of wind and temperature fluctuations in the middle atmosphere, attributed to internal gravity waves, have shown the amplitudes to increase with altitude, but more slowly than implied by the decrease in density in the absence of dissipation [*Fritts*, 1984]. Linear saturation theory was first used to address gravity wave instability and turbulence production, and the assumption implicit in this theory is that any wave amplitude in excess of a threshold value will lead to instability and the production of turbulence that acts to prevent further growth of the wave amplitude.

The relative amplitude threshold – a (scaled by the intrinsic phase speed, see below) is defined as the wave amplitude required for instability. It is assumed that the

DOI:10.2312/GFZ.b103-08040

nominal threshold amplitudes for dynamical and convective instability are those which yield $Ri < 1/4$ and $Ri < 0$, respectively, with the local Richardson number (Ri) defined to be [*Fritts and Rastogi*, 1985]:

$$Ri = \frac{N^2}{u_z'^2 + v_z'^2}, \tag{2.6}$$

where u'_z and v'_z are the local wind shears. For most intrinsic frequencies the two threshold amplitudes are nearly identical and equal to unity, departing significantly only for $\omega \sim f$. It was suggested by *Fritts* [1984] and shown by *Dunkerton* [1984] and *Fritts and Rastogi* [1985] that wave motions can be dynamically unstable (as measured along a vertical axis) at substantially smaller wave amplitudes for intrinsic frequencies near the inertial frequency due to the transverse shear in the velocity field of such motions. In the case when $\omega^2 << N^2$, the theoretical amplitude threshold a for shear instability assuming a minimum Richardson number of 1/4 is given by *Fritts and Rastogi* [1985] and *Fritts* [1989]:

$$a = \frac{|u'|}{|c - \bar{u}|} = \frac{2 \cdot \left(1 - f^2/\omega^2\right)^{1/2}}{1 + \left(1 - f^2/\omega^2\right)^{1/2}}. \tag{2.7}$$

As a function of f/ω, this threshold a falls from unity to zero when the ratio f/ω changes from zero ($\omega^2 >> f^2$) to unity ($\omega \sim f$). Thus, when $\omega^2 << N^2$, the following condition for a is valid:

$$1 > a > 0. \tag{2.8}$$

2.3. IDENTIFICATION OF THE OBSERVED FLUCTUATIONS AS WAVE-INDUCED AND METHOD OF THE INTRINSIC FREQUENCY DETERMINATION

In order to identify the observed "wavelike" temperature (or density) fluctuations with wave-induced ones we, initially, determine the experimental value of relative amplitude threshold a_e. If the a_e value satisfies the condition (2.8), then we can

DOI:10.2312/GFZ.b103-08040

assume that observed fluctuations are due to a wave. In this case, the equation (2.7) gives the possibility to determine the f/ω ratio. Note that the criterion (2.8) for the identification of IGW from observations is necessary, but not sufficient, because the observed perturbations may result from processes other than gravity waves. For example, these may be due to thin stable layers or random measurement errors. However, inspection of the raw data shows that stable layers produce, as a rule, large impulsive temperature (or density) bursts with small enough vertical scales. The role of measurement noise for gravity wave characteristics obtained from RO temperature retrievals of GPS was discussed by *Marquardt and Healy* [2005]. They showed that for realistic noise levels, temperature fluctuations can be safely interpreted as originating from small-scale atmospheric waves in the altitude region below 30 km and for wavelengths above 2 km. For noise levels typical for GPS/MET, standard deviations are below or at most in the order of 1 K below 30 km altitude, and the contribution of noise to the power spectral density is by two orders of magnitudes smaller for vertical wavelengths above 2 km [Marquardt and Healy, 2005]. This consideration leads us to the conclusion that observed temperature (or density) fluctuations in the low stratosphere may generally be related to gravity waves when the a_e value of relative amplitude threshold obeys the relation:

$$1 > a = a_e > 0. \qquad (2.9)$$

For the above mentioned reasons, the criterion (2.9) for the IGW identification may be considered not only necessary, but sufficient at least below 30 km altitude where the noise appears unable to account for observed fluctuations. In the opposite case, when $a_e > 1$, the observed fluctuations can also be connected with a thin stable layer or turbulence. The main idea of the experimental determination of the relative amplitude threshold a_e is as follows. By using the definition of the intrinsic horizontal phase

DOI:10.2312/GFZ.b103-08040

speed $|c\text{-}\bar{u}|$ and equation (2.1), in the case when $\omega^2 << N^2$, one may obtain the relation:

$$\left|c-\bar{u}\right| = \frac{\omega}{|k|} = \frac{N}{|m|}\cdot\left(1-f^2/\omega^2\right)^{-1/2} = N\frac{\lambda_z}{2\pi}\cdot\left(1-f^2/\omega^2\right)^{-1/2}, \tag{2.10}$$

where $\lambda_z = 2\pi / |m|$ is the vertical wavelength. Substituting the expression for $|u'|$ from (2.4) or (2.5) into (2.7), and taking into account (2.9) and (2.10), one can find:

$$a_e = \frac{g|m|}{N^2}\cdot\frac{|\rho'|}{\bar{\rho}} = \frac{2\pi\cdot g}{\lambda_z N^2}\cdot\frac{|\rho'|}{\bar{\rho}} = \frac{2\left(1-f^2/\omega^2\right)^{1/2}}{1+\left(1-f^2/\omega^2\right)^{1/2}}, \tag{2.11}$$

$$a_e = \frac{g|m|}{N^2}\cdot\frac{|T'|}{\bar{T}} = \frac{2\pi\cdot g}{\lambda_z N^2}\cdot\frac{|T'|}{\bar{T}} = \frac{2\left(1-f^2/\omega^2\right)^{1/2}}{1+\left(1-f^2/\omega^2\right)^{1/2}}. \tag{2.12}$$

Because all parameters included in the left part of equations (2.11) and (2.12) can be restored from RO measurements of density or temperature, so it enables to determine experimentally the relative amplitude threshold a_e.

[10] When the observed wavelike variations $\rho'/\bar{\rho}$ or $T'/\bar{T}$ are positively identified and the experimental value a_e can be found, the expression (2.11) or (2.12) allows to determine the intrinsic frequency of the internal gravity wave:

$$\omega = \frac{f}{2}\cdot\frac{2-a_e}{\left(1-a_e\right)^{1/2}}. \tag{2.13}$$

In addition, this simple relation holds:

$$\left(1-f^2/\omega^2\right)^{1/2} = \frac{a_e}{2-a_e}. \tag{2.14}$$

On substituting Eq. (2.14) into Eq. (2.10), for intrinsic horizontal phase speed $|c\text{-}\bar{u}|$ we can obtain:

DOI:10.2312/GFZ.b103-08040

$$\left|c-\bar{u}\right| = \frac{N}{|m|}\cdot\frac{2-a_e}{a_e} = \frac{\lambda_z N}{2\pi}\cdot\frac{2-a_e}{a_e}\,. \tag{2.15}$$

According to the definition of intrinsic vertical phase speed W_ϕ, and using the expression (2.13), we have:

$$W_\Phi = \frac{\omega}{|m|} = \frac{f}{2|m|}\cdot\frac{2-a_e}{(1-a_e)^{1/2}} = \frac{\lambda_z f}{4\pi}\cdot\frac{2-a_e}{(1-a_e)^{1/2}}\,. \tag{2.16}$$

Taking into account the relations (2.7), (2.9) and (2.15), the amplitude of velocity perturbations $|u'|$ may be found:

$$|u'| = a_e\left|c-\bar{u}\right| = \frac{N}{|m|}\cdot(2-a_e) = \frac{\lambda_z N}{2\pi}\cdot(2-a_e)\,. \tag{2.17}$$

One can find the other perturbation amplitudes, $|v'|$ and $|w'|$, by using the expressions (2.2), (2.3), (2.10), (2.13), (2.15) and (2.17):

$$|v'| = \frac{f}{\omega}\cdot|u'| = 2\frac{N}{|m|}(1-a_e)^{1/2} = \frac{\lambda_z N}{\pi}(1-a_e)^{1/2}\,, \tag{2.18}$$

$$|w'| = \frac{|k|}{|m|}\cdot|u'| = \frac{f\cdot a_e}{2|m|}\cdot\frac{2-a_e}{(1-a_e)^{1/2}} = \frac{\lambda_z f\cdot a_e}{4\pi}\cdot\frac{2-a_e}{(1-a_e)^{1/2}}\,. \tag{2.19}$$

The horizontal wave number k and the horizontal wavelength λ_x can be found from (2.13) and (2.15):

$$|k| = \frac{\omega}{\left|c-\bar{u}\right|} = \frac{|m|}{2}\cdot\frac{f}{N}\cdot\frac{a_e}{(1-a_e)^{1/2}} = \frac{\pi\cdot f}{\lambda_z N}\cdot\frac{a_e}{(1-a_e)^{1/2}}\,, \tag{2.20}$$

$$\lambda_x = \frac{2\pi}{|k|} = 4\pi\frac{N}{f}\cdot\frac{(1-a_e)^{1/2}}{a_e\cdot|m|} = 2\frac{\lambda_z N}{f}\cdot\frac{(1-a_e)^{1/2}}{a_e}\,. \tag{2.21}$$

DOI:10.2312/GFZ.b103-08040

The relative amplitude threshold and other wave parameters can be experimentally determined by this method when the altitude profile of the Brunt-Vaisala frequency is known. We computed the Brunt-Vaisala frequency, *N*, by evaluating [*Lindzen,* 1981]:

$$N^2 = \frac{g}{T} \cdot \left(\frac{\partial T}{\partial z} + \frac{g}{c_p} \right), \tag{2.22}$$

where $g/c_p = 9.8 \cdot 10^{-3}$ K/m. Thus, the analysis of RO data on the basis of the proposed technique allows to expand considerably the base of determined wave parameters. We assume that this technique can be also applied to any vertical temperature (or density) profile measured by other than RO methods.

2.4. UNCERTAINTIES FOR ESTIMATED WAVE PARAMETERS AND THE EXPERIMENTAL EXAMINATION OF THE TECHNIQUE PROPOSED

In order to find uncertainties for estimated wave parameters, we need to first obtain the uncertainty of such key parameter as the relative amplitude threshold a_e. We assume that the statistical error (the standard deviation) of the temperature is equal to δT, the vertical resolution of temperature data is δh, and small sinusoidal temperature perturbations $T'(h)$ of vertical wavelength λ_z take place in the atmosphere. If $|T'|$ is the wave amplitude and L is the height interval for wave observations, then the uncertainty of the wave amplitude $\delta|T'|$ and that of the wavelength $\delta\lambda_z$ can be derived from the measurement errors δT and δh as:

$$\delta|T'| \approx \left(\frac{\lambda_z}{L} \right)^{1/2} \delta T \ , \tag{2.23}$$

$$\delta\lambda_z \approx \left(\frac{\lambda_z}{L} \right)^{1/2} \delta h \ . \tag{2.24}$$

DOI:10.2312/GFZ.b103-08040

It is important to note that the major part of the resulting error for a_e is due to the uncertainties in estimation of N^2. Since we assume that wave-induced variations of N^2 are present in the atmosphere, then the simple background estimate $\overline{N^2}$ can be used for substitution into (2.12) in order to determine a_e. For the calculation of $\overline{N^2}$ we apply (2.22) to the background ($\overline{T}$) profile. Although the error of $\overline{N^2}$ may be very small, the basic error source is the wave-induced scatter of N^2 over its local mean $\overline{N^2}$ because a "true" value of N^2, implied in (2.11) or (2.12), is not exactly known. The upper error limit of this "true" value is estimated as the standard deviation of N^2, assuming that sinusoidal temperature perturbations with the amplitude $|T'|$ and vertical wavelength λ_z take place in the atmosphere. In this case, the relative uncertainty in the Brunt-Vaisala frequency squared $\delta N^2/N^2 \approx \delta N^2/\overline{N^2}$ can be expressed from (2.22) as:

$$\frac{\delta N^2}{N^2} \approx \pi\sqrt{2}\cdot\frac{|T'|}{\lambda_z}\cdot\left(\frac{\partial\overline{T}}{\partial z}+\frac{g}{c_p}\right)^{-1} . \tag{2.25}$$

Following to *Squires* (1968) and taking into account (2.12) and (2.23)-(2.25), we obtain the expression for the relative uncertainty $\delta a_e/a_e$ in the amplitude threshold a_e:

$$\begin{aligned}\frac{\delta a_e}{a_e} &\approx \left[\left(\frac{\delta|T'|}{|T'|}\right)^2+\left(\frac{\delta\lambda_z}{\lambda_z}\right)^2+\left(\frac{\delta N^2}{N^2}\right)^2\right]^{1/2} \approx \\ &\approx \left[\frac{\lambda_z}{L}\left(\frac{\delta T}{|T'|}\right)^2+\frac{\lambda_z}{L}\left(\frac{\delta h}{\lambda_z}\right)^2+2\pi^2\left(\frac{|T'|}{\lambda_z}\right)^2\cdot\left(\frac{\partial\overline{T}}{\partial z}+\frac{g}{c_p}\right)^{-2}\right]^{1/2} .\end{aligned} \tag{2.26}$$

Here we introduce a variable X as $X=\delta a_e/a_e$. One can see from (2.9) that there are some additional limitations for the a_e value in the case when the relative uncertainty X is found. These can be expressed as:

DOI:10.2312/GFZ.b103-08040

$(1+X)\ a_e < 1,$ (2.27)

$(1-X)\ a_e > 0.$ (2.28)

In the case of small or moderate measurement errors ($X<1$) when the condition (2.28) is automatically satisfied, we have limitations for the experimental a_e value, namely:

$(1+X)^{-1} > a_e > 0.$ (2.29)

The expression (2.29) states that not only a_e, but also $(a_e-\delta a_e)$ and $(a_e+\delta a_e)$ values satisfy to condition (2.9). This implies that we have reliable estimates of wave parameters because standard deviations of these are limited in this case. Using (2.13)-(2.21), the statistical errors of other wave parameters can be easy obtained from the error of the amplitude threshold in (2.26). For example, the uncertainty of the intrinsic frequency can be directly found from (2.13):

$$\frac{\delta\omega}{\omega} \approx \frac{a_e \cdot \delta a_e}{2(1-a_e)(2-a_e)} \approx \frac{X \cdot a_e^2}{2(1-a_e)(2-a_e)}\ . \tag{2.30}$$

Taking into account $2\cdot\delta N/N=\delta N^2/N^2$ we obtain the expressions for the relative uncertainty of each estimated parameter:

$$\frac{\delta|c-\bar{u}|}{|c-\bar{u}|} \approx \left[\left(\frac{\delta\lambda_z}{\lambda_z}\right)^2 + \left(\frac{\delta N^2}{2N^2}\right)^2 + \left(\frac{2X}{2-a_e}\right)^2\right]^{1/2}, \tag{2.31}$$

$$\frac{\delta W_\Phi}{W_\Phi} \approx \left[\left(\frac{\delta\lambda_z}{\lambda_z}\right)^2 + \left(\frac{\delta\omega}{\omega}\right)^2\right]^{1/2} \approx \left[\left(\frac{\delta\lambda_z}{\lambda_z}\right)^2 + \left(\frac{X \cdot a_e^2}{2(1-a_e)(2-a_e)}\right)^2\right]^{1/2}, \tag{2.32}$$

$$\frac{\delta|u'|}{|u'|} \approx \left[\left(\frac{\delta\lambda_z}{\lambda_z}\right)^2 + \left(\frac{\delta N^2}{2N^2}\right)^2 + \left(\frac{X \cdot a_e}{2-a_e}\right)^2\right]^{1/2}, \tag{2.33}$$

$$\frac{\delta|v'|}{|v'|} \approx \left[\left(\frac{\delta\lambda_z}{\lambda_z}\right)^2 + \left(\frac{\delta N^2}{2N^2}\right)^2 + \left(\frac{X \cdot a_e}{2-2a_e}\right)^2\right]^{1/2}, \tag{2.34}$$

DOI:10.2312/GFZ.b103-08040

$$\frac{\delta\lambda_x}{\lambda_x} \approx \frac{\delta|k|}{|k|} \approx \left[\left(\frac{\delta\lambda_z}{\lambda_z} \right)^2 + \left(\frac{\delta N^2}{2N^2} \right)^2 + \left(\frac{X(2-a_e)}{2(1-a_e)} \right)^2 \right]^{1/2}, \tag{2.35}$$

$$\frac{\delta|w'|}{|w'|} \approx \left[\left(\frac{\delta\lambda_z}{\lambda_z} \right)^2 + \left(\frac{X\left(3a_e^2 - 6a_e + 4\right)}{2(1-a_e)(2-a_e)} \right)^2 \right]^{1/2}. \tag{2.36}$$

As is seen from obtained expressions, the relative uncertainty of such parameters as ω, W_ϕ, v', λ_x, k and w' can be very large when the a_e values are close to unity. In this case, the application of this technique is less effective because of deterioration of accuracy.

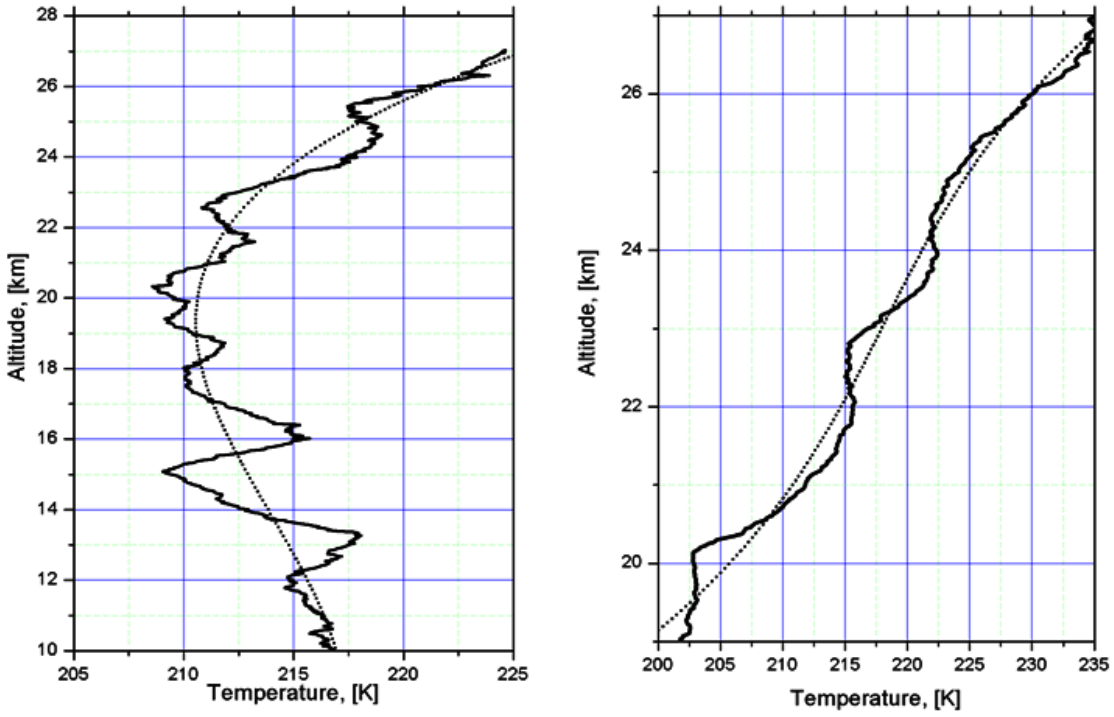

Fig. 2.1. Temperature profiles retrieved from RO events (FORMOSAT-3) observed on 23 April 2006 in the southern (left panel) and northern (right panel) atmosphere. The coordinates of the sounded regions were 57.8° S; 295.1° W (south) and 19.2° N; 290.4° W (north). The original (solid) and their background (dotted) profiles were used for gravity wave analysis.

In order to demonstrate the practical application of the proposed analysis technique, let us consider the GPS/FORMOSAT-3 RO retrievals of temperature profiles in the Earth's stratosphere. Fig. 2.1 shows two temperature profiles observed

DOI:10.2312/GFZ.b103-08040

on 23 April 2006. The coordinates of the sounded regions, shown in Fig. 2.1, were 57.8° S; 295.1° W (left panel) and 19.2° N; 290.4° W (right panel), respectively. The original (solid) and their background (dotted) profiles within the height ranges, indicated in Fig. 2.1, were used for gravity wave analysis. Using radio holographic method [*Hocke et al.*, 1999; *Pavelyev et al.*, 2004], we obtained original temperatures with the random error $\delta T \simeq 0.4$ K and vertical resolution $\delta h \simeq 100$ m. In order to find the background temperature profile a third-order polynomial was fitted to the original profile within the height interval L of wave observations. On the basis of original (T) and background $(\overline{T})$ profiles, we computed the normalized temperature fluctuation profiles $\left(T'/\overline{T}\right)$ by the usual expression $T'/\overline{T} = \left(T - \overline{T}\right)/\overline{T}$.

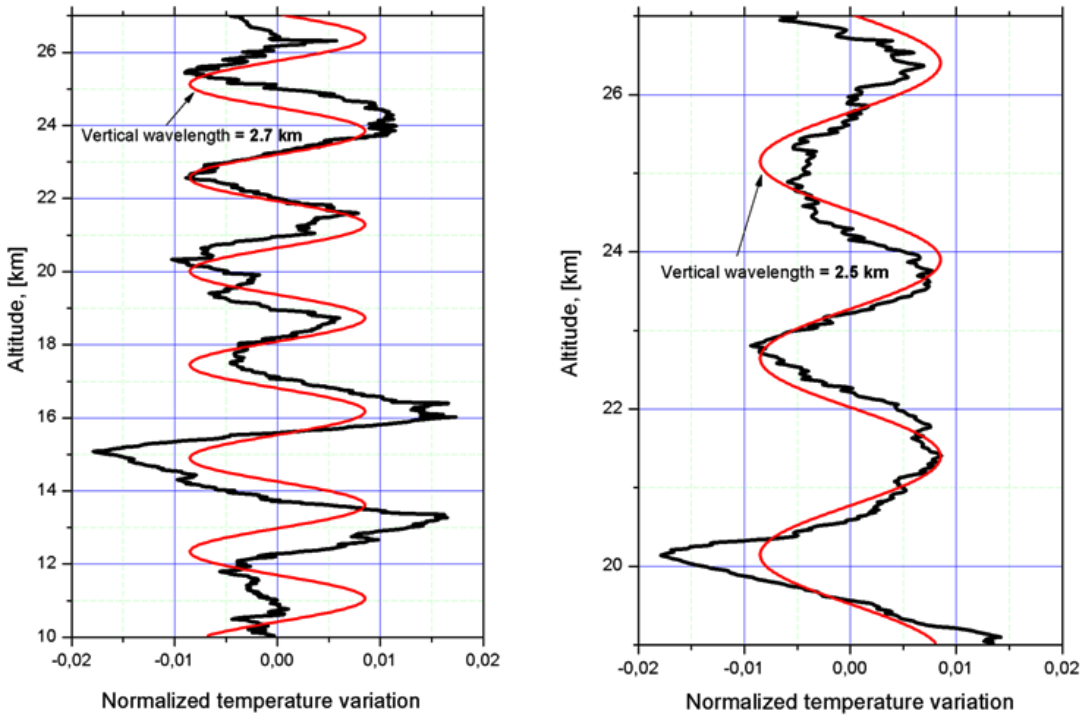

Fig. 2.2. Altitude dependences of the normalized temperature perturbations observed in the RO sounding of the southern (left panel) and northern (right panel) atmosphere. The model sine functions (smooth curves shown superimposed) were fitted to the measured profiles.

DOI:10.2312/GFZ.b103-08040

In Fig. 2.2 we show the altitude series of normalized temperature perturbations $T'/\overline{T}$. The model sine functions (smooth curves shown superimposed) were fitted to measured profiles, and they are represented for comparison and for evaluation of the normalized temperature perturbation amplitudes $|T'|/\overline{T}$ and vertical wavelengths λ_z. As is seen from Fig. 2.2, the values of amplitude $|T'|/\overline{T}$ are very close and equal to 0.0085, and the wavelengths are somewhat different and equal to 2.7 and 2.5 km in the two sessions. For the determination of the relative amplitude thresholds a_e, the Brunt-Vaisala frequency was derived from the expression (2.22). In order to ensure a good estimate of *N*, we computed its background profile for each session based on the

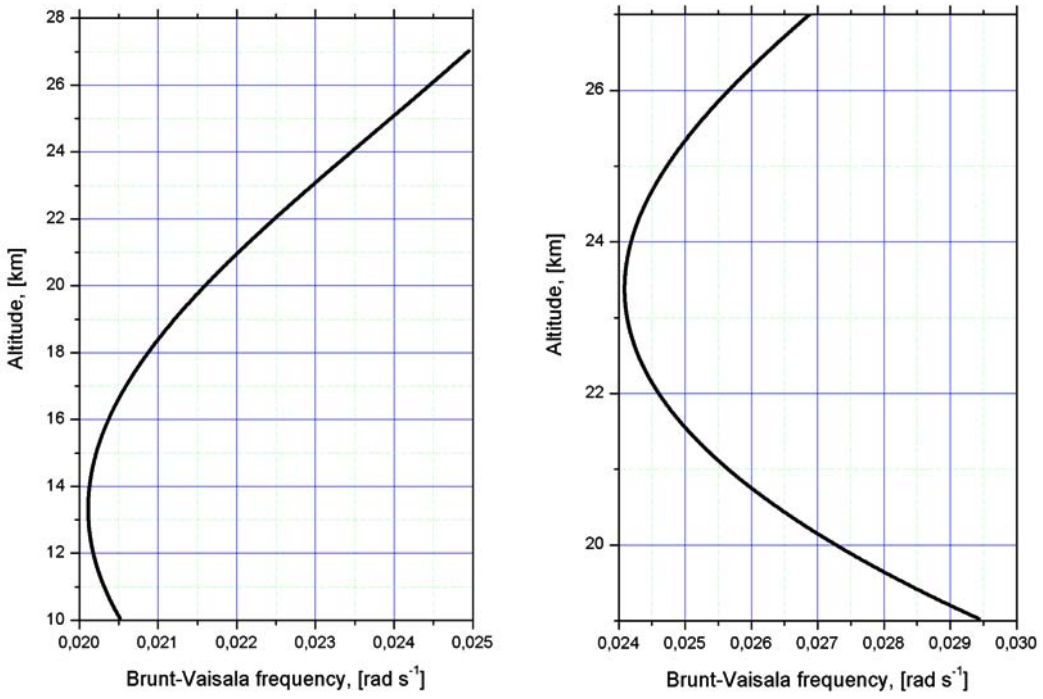

Fig. 2.3. Brunt-Vaisala frequencies computed from the mean temperature profiles for the southern (left panel) and northern (right panel) atmosphere. The constant *N* magnitudes of 0.0215 and 0.025 rad/s were used for the calculation of the experimental values a_e in the southern and northern atmosphere, correspondingly.

corresponding mean temperature profile (see Fig. 2.1). Fig. 2.3 shows plots of *N* profiles for the two sounded regions and confirms that the *N* value is weakly sensitive

DOI:10.2312/GFZ.b103-08040

to actual thermal structure and well represented by a constant for the investigated height ranges. For the calculation of the experimental values a_e, we thus took reasonable constant values of N = 0.0215 rad/s (Fig. 2.3, left panel) and N=0.025 rad/s (Fig. 2.3, right panel).

Let us obtain some estimates of uncertainties followed from (2.23)-(2.26). As an example, we will consider the first sounded region (southern atmosphere). We have here:

$L \simeq 17$ km, $|T'| \simeq 1.785$ K, $\lambda_z \simeq 2.7$ km, $N \simeq 0.0215$ rad/s, $\delta T \simeq 0.4$ K, $\delta h \simeq 100$ m.

Substituting these values into (2.23)-(2.26), we obtain:

$$\delta\lambda_z/\lambda_z \simeq 1.5\%,\ \delta|T'|/|T'| \simeq 8.9\%,\ \delta N^2/N^2 \simeq 29.4\%,\ X = \delta a_e/a_e \simeq 30.7\%.$$

These results show that the $\delta N^2/N^2$ term gives the main contribution into the relative uncertainty of a_e. Note that substitution of the obtained X value into (2.29) allows to find the range reliable estimates of a_e in this case: $a_e < 0.76$.

Based on above-mentioned temperature data and using obtained expressions, we computed the wave parameters for the two sounded regions.

Table 2.1. Wave parameters found from GPS/FORMOSAT-3 RO retrievals of temperature profiles in two regions of the Earth's stratosphere. The coordinates of sounded regions and the time of observations are indicated. Relative uncertainties of determined parameters are also shown

No	λ_z, km	$\lvert T'\rvert/\overline{T}$	$N\cdot10^2$, rad/s	a_e	f/ω	$\omega\cdot10^4$, rad/s	$\lvert c-\bar{u}\rvert$, m/s	$\lvert u'\rvert$, m/s	$\lvert v'\rvert$, m/s	λ_x, km	$W_\Phi\cdot10^3$ m/s	$\lvert w'\rvert\cdot10^3$ m/s
23 April 2006 (57.8° S; 295.1° W). Relative uncertainties (%) are shown on line 2												
1	2.7	0.0085	2.15	0.42	0.96	1.44	34.8	14.6	14.1	1524	61.7	25.9
2	1.5	8.9	14.7	30.7	2.9	2.9	41.6	16.9	18.5	44.4	3.3	33.7
23 April 2006 (19.2° N; 290.4° W). Relative uncertainties (%) are shown on line 4												
3	2.5	0.0085	2.50	0.33	0.98	0.51	49.4	16.6	16.2	6078	20.3	6.8
4	2.2	12.5	15.9	34.2	1.7	1.7	44.1	17.4	18.2	45.7	2.8	36.0

In Table 2.1 we have summarized all the wave parameters and their relative uncertainties. We see that the wave characteristics can be obtained from a single temperature profile.

DOI:10.2312/GFZ.b103-08040

For the experimental examination of the efficiency of the analysis technique proposed, we used the results of the simultaneous temperature and wind velocity measurements obtained in a high-resolution balloon experiment [*Cot and Barat*, 1986], where a nearly monochromatic and long-period wave propagating upward in the stratosphere was identified. From all the data, *Cot and Barat* [1986] have estimated the mean characteristics of the wave, such as the vertical and horizontal wavelengths, ratio f/ω, vertical and horizontal wave-induced velocity amplitudes, intrinsic vertical and horizontal phase speeds, temperature perturbation amplitude. By using the temperature data only, we reconstructed the ratio f/ω and other wave parameters.

Table 2.2. Summary of observed wave parameters [Cot and Barat, 1986] and those reconstructed from temperature data. Relative deviations between observed and reconstructed wave parameters are indicated

λ_z, km	$\lvert T'\rvert$,K	$\overline{T}$, K	N, rad/s	a_e	f/ω	$\omega\cdot10^4$, rad/s	$\lvert c-\bar{u}\rvert$, m/s	$\lvert u'\rvert$, m/s	λ_x, km	W_Φ, m/s	$\lvert w'\rvert$, m/s
Parameters observed by *Cot and Barat* [1986]											
1.0	1.0	231.5	0.02	–	0.8	1.25	5.2	3.3	260	0.020	0.013
Basic parameters for reconstruction				Parameters reconstructed from temperature data							
1.0	1.0	231.5	0.02	0.67	0.86	1.16	6.3	4.2	341	0.018	0.012
–	–	–	–	Relative deviations of observed and reconstructed wave parameters, %							
				–	7.5	7.2	21.2	27.3	31.2	10.0	7.7

In Table 2.2 we give observed wave parameters [*Cot and Barat*, 1986], our reconstruction results, and relative deviations of observed and reconstructed wave parameters. An intercomparison between observed and reconstructed wave parameters shows good agreement. It is seen from the values given in Table 2.2 that the relative deviations of the reconstructed parameters are not larger than 31%. The best agreement is found for such parameters as f/ω, ω, W_ϕ, $|w'|$ which are reproduced with relative deviations ≤10%. Thus, we have shown that reasonable estimates of wave characteristics can be obtained from a single temperature profile in the case when the wave is positively identified.

DOI:10.2312/GFZ.b103-08040

2.5. SUMMARY

The analysis technique of the experimental determination of the IGW intrinsic frequency from the RO temperature vertical profiles is proposed for the case of a positively identified wave which saturates via dynamical instability. The suggested method is most effective in the case of low IGW frequencies ($\omega \sim f$), when the experimentally determined parameter a_e appreciably differs from unity. The analysis of RO data on the basis of the proposed method allows one to expand considerably the base of determined wave parameters. This method can be applied for the analysis of vertical temperature (or density) profiles measured by other than RO techniques.

3. STUDYING INTERNAL WAVES IN THE ATMOSPHERE ON A GLOBAL SCALE

3.1. METHODS FOR INVESTIGATION OF THE INTERNAL WAVES

Atmospheric waves have been a subject of intensive research activities in recent years because of their various effects and major contributions to atmospheric circulation, structure, and variability [*Fritts and Alexander*, 2003]. Apart from occasionally intense lower-atmospheric effects, the major wave influences occur in the middle atmosphere, between ~ 10 and 110 km altitudes because of decreasing density and increasing wave amplitudes with altitude [*Fritts and Alexander*, 2003]. There are different kinds of atmospheric waves with various mechanisms of generation and diverse areas of existence [*Alexander et al.*, 2000]. For example, the equatorial Kelvin waves are of planetary scale in the zonal direction with periods of several days to a few weeks. They are particularly important for the dynamics of the middle atmosphere in the tropical regions [*Alexander et al.*, 2000]. Mountain waves are excited due to orographic influence on strong wind flow [*Eckermann and Preusse*, 1999]. Mountain waves are a partial case of the internal gravity waves (GWs), which exist over a very

DOI:10.2312/GFZ.b103-08040

broad area in the Earth atmosphere and ionosphere [*McFarlane*, 1997]. The GWs play a decisive role in transporting energy and momentum, in contributing turbulence and mixing, and in affecting the atmospheric circulation and temperature regime [*Fritts and Alexander*, 2003]. The GWs generate drag, whose contribution is significant for accurate climate and weather forecasting models [*Ebel*, 1984, *Fritts and Alexander*, 2003]. However, up till now global models that include parametrized gravity wave effects have an excessively broad range of tuning parameters [*Alexander and Rosenlof*, 2003]. Therefore, the experimental data obtained at different altitudes over the Earth globe during long time periods are necessary to establish realistic models describing wave activities in the atmosphere and ionosphere. Radiosonde and rocketsonde GWs measurements, balloon soundings, radar observations, and lidar studies have been limited to ground-based sites [*Eckermann et al.*, 1995, *Steiner and Kirchengast*, 2000, *Tsuda et al.*, 2004, *Wang et al.*, 2005] mainly over specific land parts of the Northern and Southern Hemispheres.

Radically new technology incorporates the high-precision GPS radio signals at two frequencies F1=1575.42 and F2=1227.6 MHz for internal waves investigation. The small satellite (e.g., MicroLab-1, launched into a near polar circular orbit of about 750 km altitude) carried a laptop sized GPS receiver for remote sensing of the atmosphere and ionosphere by limb sounding method [*Ware et al.*, 1996, *Feng and Herman*, 1999]. The advantages of space-borne observations of earth atmosphere by the GPS radio signals propagating through the stratosphere are that the RO technique can recover atmospheric profiles above oceans as well as above land with high vertical resolution (<0.4 km) and accuracy (<1 K in temperature within the upper troposphere and lower stratosphere) [*Anthes et al.*, 2000, *Kuo et al.*, 2000]. The vertical wavelength of internal waves is usually far below the horizontal wavelength so that the RO method is well

DOI:10.2312/GFZ.b103-08040

adopted to observe the internal waves. Nowadays, new satellite missions CHAMP, SAC-C, GRACE, and FORMOSAT-3/COSMIC have been launched for global RO monitoring of the meteorological processes in the atmosphere and phenomena in the ionosphere [*Reigber et al.*, 2005, *Hajj et al.*, 2004]. Statistical noise in the phase path excess of the GPS RO signals is roughly ±1 mm at the distance 30,000 km [*Pavelyev et al.*, 2002]. A new amplitude technology has been proposed and validated to find the vertical gradients of the refractivity and temperature in the atmosphere with high accuracy and spatial resolution, which is important for the GW investigation [*Pavelyev et al.*, 2002, *Liou et al.*, 2002, 2003].

The amplitude channel of the radio hologram can be used separately from the phase channel to obtain information on the vertical distribution of the refractivity, temperature, and its vertical gradient in the upper troposphere and stratosphere [*Pavelyev et al.*, 2002, 2003, *Liou et al.*, 2003]. Additional information may be retrieved (in the case of GW) on the quantitative characteristics of the wave processes: vertical distribution of the horizontal wind perturbations and its gradient. Below we will consider in detail the method for retrieving the GW parameters from the measurements of the amplitude variations of the GPS RO signal by using the CHAMP RO data.

DOI:10.2312/GFZ.b103-08040

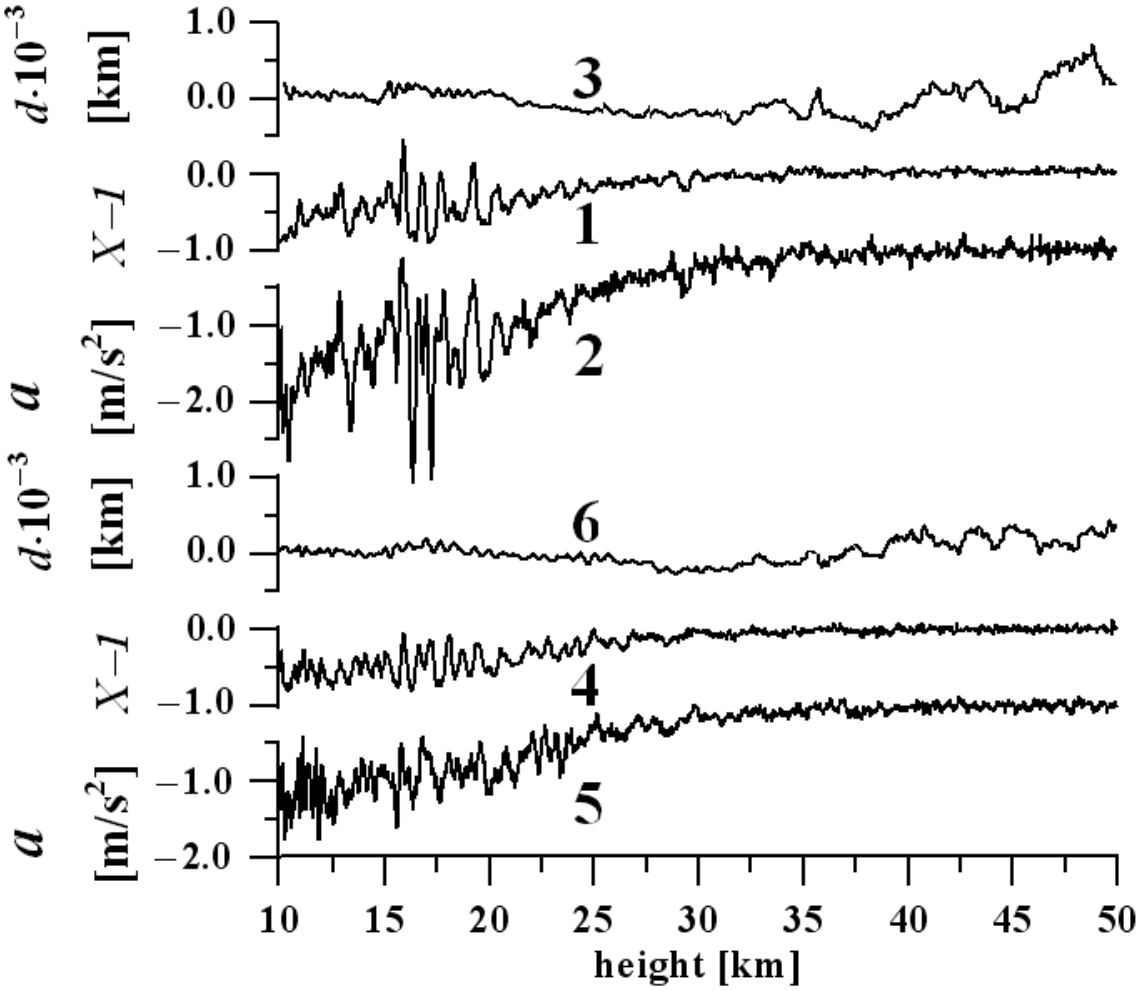

Fig. 3.1. Intensity variations *X–1* (curves 1 and 4), phase acceleration *a* (curves 2 and 5), and distance *d* (curves 3 and 6) at the first GPS frequency F1. Curves 1–3 and 4–6 correspond to the CHAMP RO events № 0140 (02 h 35 m 34 s LT, 21.9 N 172.5 W) and № 0001 (02 h 09 m 51 s LT, 15.9 N 330.0 W), January 23 and 24, 2003, respectively.

We select the amplitude variations observed in the RO events № 0140 and № 0001 shown in Fig. 3.1 (curves 1 and 4). The location of the tangent point T in these events does not have significant variations in the horizontal direction at the altitudes between 10 and 45 km (as seen in Fig. 3.2, curves 3 and 6).

DOI:10.2312/GFZ.b103-08040

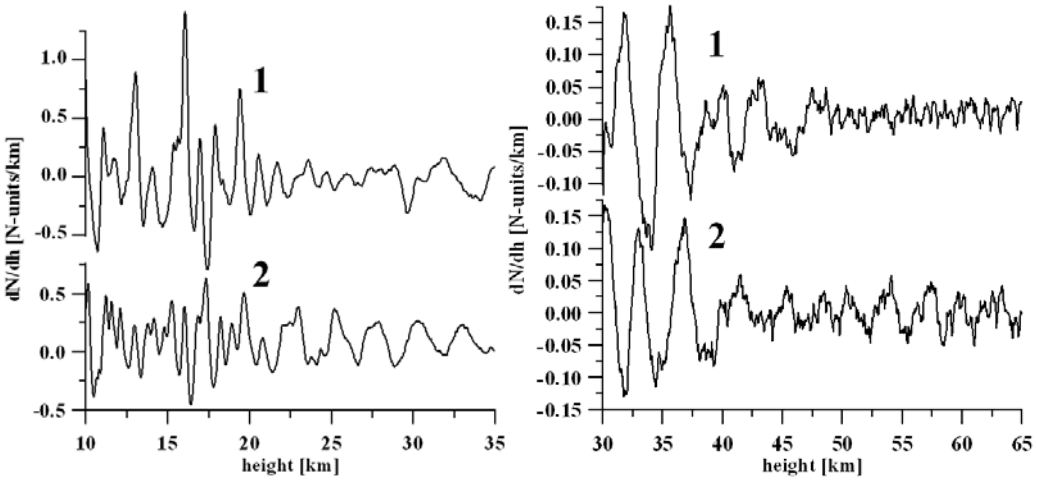

Fig. 3.2. Vertical gradient of refractivity perturbations at the first GPS frequency F1 in the 10–30 km (left) and 30–65 km height interval (right). Abrupt changes in the amplitude and phase of the refractivity perturbations are seen between the altitudes 38 km-40 km (curves 1 and 2, right panel) and 45 km-50 km (curve 1, right panel). These altitudes are relevant to wave breaking levels in the atmosphere. Curves 1 and 2 correspond to the CHAMP RO events № 0140 (02 h 35 m 34 s LT, 21.9 N 172.5 W) and № 0001 (02 h 09 m 51 s LT, 15.9 N 330.0 W), January 23, 2003, respectively.

As follows, the amplitude variations observed in the RO events № 0001 and № 0140 are connected with wave structures in the neutral gas. The amplitude variations can be recalculated to the perturbations in the vertical refractivity gradient *dN(h)/dh* [*Pavelyev et al.*, 2002, 2004; *Liou et al.*, 2006]. Variations of the vertical gradient of refractivity retrieved from the RO amplitude data are shown in Fig. 3.2 for the CHAMP RO events № 0140 and № 0001, January 23, 2003 (curves 1 and 2, respectively). The wave structure is clearly seen in the perturbations of the vertical refractivity gradient in the 10 km–65 km interval (curve 1 and 2, left and right panels in Fig. 3.2). The vertical period of the wave structure grew from 0.8 km-1.0 km in the 8 km-25 km interval to 2 km-4 km in the 30 km-40 km interval. Abrupt changes in the amplitude and phase of the refractivity perturbations are seen between the altitudes 38-40 km (curves 1 and 2, right panel) and 45–50 km (curve 1, right panel). These altitudes are relevant to wave breaking levels in the atmosphere. Note that the wave breaking areas are directly observed in the first time by GPS occultation method.

DOI:10.2312/GFZ.b103-08040

As followed from the analysis of data presented in Fig. 3.1 and Fig. 3.2, the amplitude variations of the RO signal are the radio-hologram of the atmospheric internal waves. In addition, the altitude profiles of the vertical gradient of refractivity are the 1-D images of the vertical structure of the internal wave in the atmosphere. These images do not depend on the nature or origin of the internal waves. One can restore from the 1-D images the altitude profiles of the phase and amplitude of the internal wave, which can be useful for establishing the nature, origin, and vertical distributions of the internal wave parameters. To establish the vertical profiles of the amplitude and phase of the internal wave, it is useful to apply the Hilbert transform [*Rabiner and Gold*, 1978]. Application of the Hilbert transform gives an analytic presentation of the real signal *t(h)*:

$$t(h)=Re\{a_t(h)exp[i\Phi_t(h)]\} \qquad (3.1)$$

where *t(h)* is a real signal, for example, the perturbations of the vertical gradient of refractivity *dN(h)/dh*, shown in Fig. 3.2, $a_t(h)$ and $\Phi_t(h)$ (real functions) are the amplitude and phase of the real signal *t(h)*.

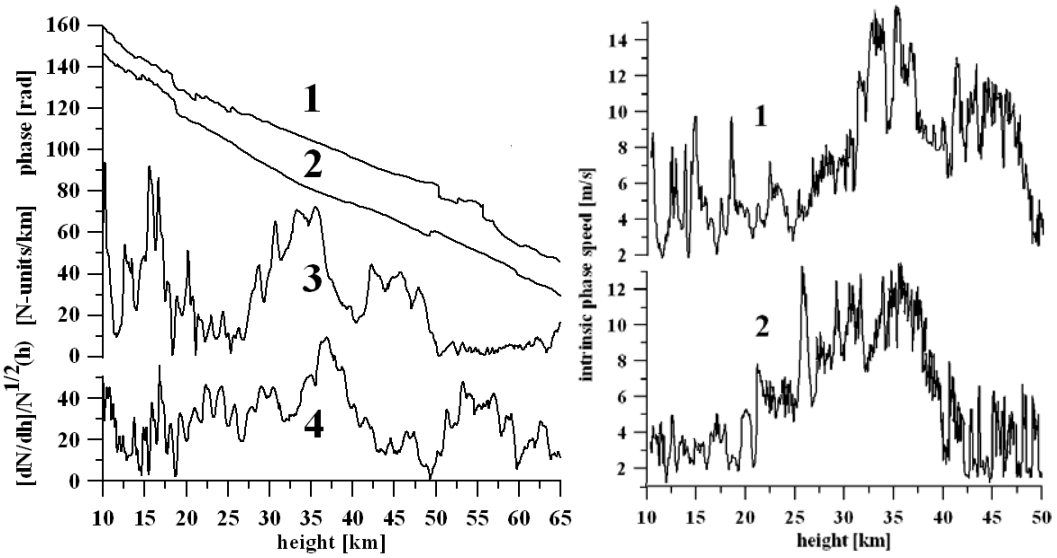

Fig. 3.3. Left panel: vertical profiles of the phase (curves 1 and 2) and amplitude (curves 3 and 4) of the GW for the CHAMP RO events № 0140 (curves 1 and 3) and № 0001 (curves 2 and 4). Right panel: altitude dependence of the intrinsic phase speed of the GW. Curves 1 and 2 correspond to the CHAMP RO events № 0140 (02 h 35 m 34

DOI:10.2312/GFZ.b103-08040

s LT, 21.9 N 172.5 W) and № 0001 (02 h 09 m 51 s LT, 15.9 N 330.0 W), January 23, 2003, respectively

The results of the computations of the vertical profiles of the amplitude and phase of the wave structures in the atmosphere are presented in Fig. 3.3, left panel, in graphical form with the variations in phase [rad] and the vertical gradient of refractivity *dN/dh(h)[N-units/km]*, normalized to the square root of the background refractivity $N(h)^{1/2}$, as ordinate, and the height *h* [km] as abscissa. Note that the RO method gives only a "momentary photo" of the internal wave. Therefore, the phase of the internal wave restored from the RO data may be presented as an increasing or decreasing with height because the direction of propagation of internal wave is not determined directly. The phases (curves 1 and 2 in Fig. 3.3, left panel) have been chosen as diminishing with height because usually the energy in the GW goes in the vertical direction. This corresponds to a downward increasing of the phase of the GW. The variations of the phase and normalized gradient of refractivity are presented in Fig. 3.3, left panel, for two CHAMP RO events № 0140 and № 0001 (curves 1, 3 and 2, 4, respectively). Curves 1, 2 and 3, 4 (Fig. 3.3) indicate the phase and amplitude dependences of the GW on height, correspondingly. The amplitude of the GW is at its maximum in the 10 km–20 km interval. The height intervals between 38 km and 40 km with abrupt changes in the amplitude can be considered as the boundaries of the GW breaking areas (curves 3 and 4 in Fig. 3.3, right panel). The general form of the GW phase as a function of height (curves 1, 2, Fig. 3.3, right panel) reveals a decrease in the vertical spatial frequency of the GW in the 20 km–40 km interval (this is in response to an increase in the spatial period of the GW). The abrupt changes in the phase (curve 1 and 2 in Fig. 3.3, right panel) conform to the height 38 km–40 km and 45 km–50 km, where the amplitude of the GW (curve 3 and 4 in Fig. 3.3, right panel) is below the noise level,

DOI:10.2312/GFZ.b103-08040

and the coherence in the GW disappears. These regions can correspond to the wave breaking altitudes where the energy of the GW is transmitted to the turbulent structures within the stratosphere.

The most possible source of the observed waves with vertical period 0.8 km-4.0 km (Fig. 3.1 and Fig. 3.2) is the GW activity [*Steiner and Kirchengast*, 2000; *Tsuda et al.*, 2000; *Tsuda and Hocke*, 2002]. If the observed wave structures are caused by the GW activity, the temperature variations can be related with the horizontal wind perturbations by means of the GW polarization equations. The changes in the vertical period of temperature variations can be connected with variations in the intrinsic phase speed of the GW using its dispersion relationship. Below we use for analysis the dispersion and polarization relationships, which are valid for the medium-frequency cases, when the intrinsic frequency of the GW is greater than the inertial frequency *f*, but is well below the buoyancy frequency ω_b. The GW dispersion relation has the form [*Eckermann et al*., 1995]:

$$\lambda_v = 2\pi \mathbf{v}_i / \omega_b, \; v_i = \left| c - U\cos\varphi \right| \qquad (3.2)$$

where λ_v is the vertical wavelength of the GW, U is the background wind speed, c denotes the ground-based GW horizontal phase speed, and φ is the azimuth angle between the background wind and the GW propagation vectors. Equation (3.2) connects the vertical wavelength λ_v with the intrinsic phase speed of the GW v_i, which can be measured by an observer moving with the background wind velocity [*Eckermann et al.*, 1995]. A GW polarization relation was published previously [*Lindzen*, 1981, *Senft and Gardner*, 1981]. These relations links the complex amplitude of the temperature, *t(h)*, and refractivity perturbations, $\Delta N(h)$, with the horizontal wind perturbations *v(h)* in GW:

$$v = Re[ig/(T_b \omega_b) t(h)] = -Re[ig/(N(h)\omega_b)\Delta N(h)] \qquad (3.3)$$

DOI:10.2312/GFZ.b103-08040

where $\omega_b^2 = g/T_b\Gamma$, $\Gamma = \partial T_b/\partial h + 9.8^o/km$, g is the gravity acceleration, and T_b, $N(h)$ are the background temperature and refractivity vertical distributions, respectively. The functions T_b, N, and ω_b in equations (3.2) and (3.3) may be estimated using the average values of atmospheric parameters expected in the RO region. To find the function $v(h)$ from equation (3.3), one can implement the Hilbert transform [Rabiner and Gold, 1978]. The function $v(h)$ can further be restored from (3.3) as imaginary part of analytic signal by employing the Hilbert transform (3.1) to the perturbations $\Delta N(h)$ found by integration of the variations of the vertical gradient of refractivity $dN(h)/dh$.

If the observed amplitude variations are caused by the propagating GW, one can estimate the intrinsic phase speed of the GW v_i by use of the relationship (3.2) after differentiating the GW phase $\Phi(h)$ (curves 1 and 2 in Fig. 3.2) on height h and finding the vertical wavelength of the GW, λ_v. The results of the intrinsic phase speed evaluation are shown in Fig. 3.3, right panel, for the CHAMP RO events № 0001 and № 0140 (curves 1 and 2, respectively). As seen in Fig. 3.3, right panel, the value $v_i(h)$ changes in the 2 m/s -16 m/s interval. The sharp variation of the intrinsic phase speed near the altitude of about 40 km can be related to the boundary of a GW breaking area.

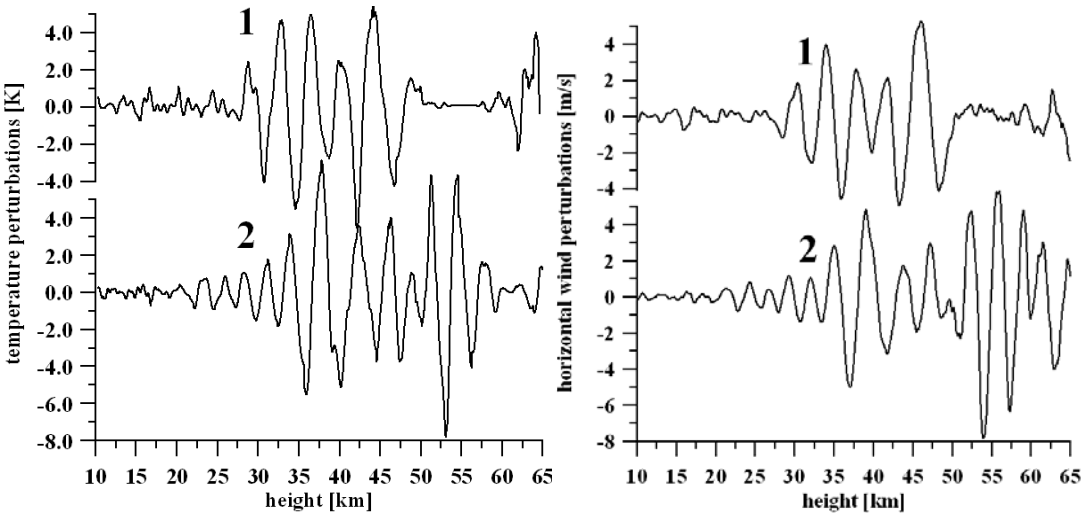

Fig. 3.4. The temperature perturbations (left panel) and the horizontal wind variations (right panel) caused by propagation of the GW. Curves 1 and 2 correspond to

DOI:10.2312/GFZ.b103-08040

the CHAMP RO events № 0140 (02 h 35 m 34 s LT, 21.9 N 172.5 W) and № 0001 (02 h 09 m 51 s LT, 15.9 N 330.0 W), January 23, 2003, respectively.

The perturbations in the vertical refractivity gradient *dN(h)/dh* can be recalculated by integration to the perturbations in the refractivity *ΔN(h)*, and, then, by use of (3.3), to variations of the temperature and horizontal wind perturbations *v*. The variations in temperature *t(h)* and horizontal wind perturbations *v* retrieved from the amplitude data are indicated for the CHAMP RO events № 0140 and № 0001 in Fig. 3.4, (curves 1 and 2, correspondingly). From the analysis of Fig. 3.4 (right panel), the horizontal wind perturbations increase with the height from ±1 m/s (10 km–20 km interval) to ±5 m/s (30 km–65 km interval). The temperature fluctuates from ±0.2 K – ±1.0 K (10 km-20 km interval) to ±4 K (30 km–65 km interval) (Fig. 3.4, left panel). The vertical period of the temperature and horizontal wind perturbations increases from 0.8 km (10 km–20 km interval) to 4 km (35 km–40 km interval).

3.2. SEASONAL AND GEOGRAPHICAL DISTRIBUTIONS OF INTERNAL WAVE ACTIVITY AT DIFFERENT ALTITUDES IN THE ATMOSPHERE

It is important to note that the amplitude variations are sensitive to the internal waves of different kind (GW, Kelvin waves, and other types having small vertical periods). Below we will do analysis, which is valid for all types of the internal waves having small vertical periods. We will characterize the internal wave activities at different altitudes in the atmosphere by the amplitude of the Hilbert Transform *q(h) [N-units/km]*, which is associated with the perturbation portion of the refractivity's vertical gradient. This parameter is useful for observing the distribution of the internal wave activity over a global scale.

DOI:10.2312/GFZ.b103-08040

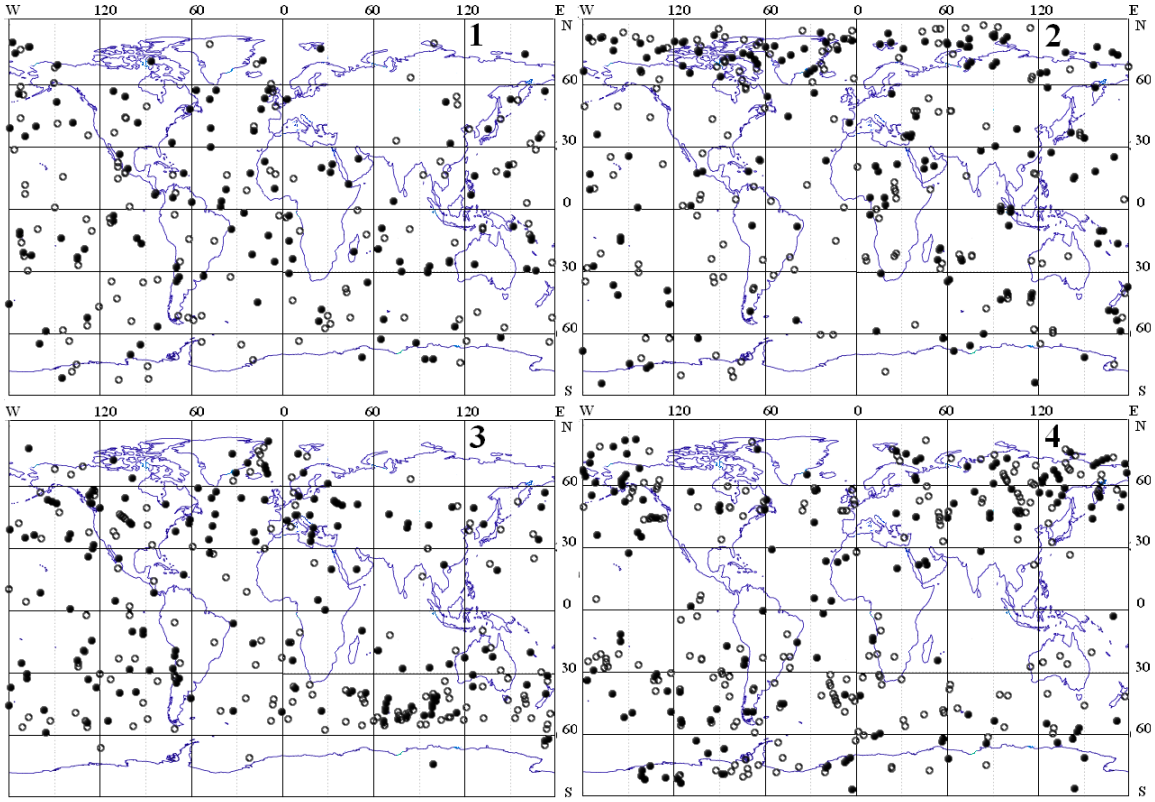

Fig. 3.5. Seasonal and geographical distribution of internal wave activity with amplitudes greater than 1.0 N-units/km (panels 1 and 2, height 12 km) and 0.6 N-units/km (panels 3 and 4, height 14 km) in the lower stratosphere for period November 19 – December 03, 2002 (panels 1 and 3) and June 29 – July 13, 2003 (panels 2 and 4).

Amplitude variations of the CHAMP RO signals provide an important picture of the wave activity in the 12 km-20 km interval with global coverage. This is illustrated in Fig.2.5 – 2.7 for period November 2002 – July 2003. The geographical distribution of the wave structures with amplitudes greater than 1.0 and 0.6 *N-units/km* is demonstrated in Fig. 3.5 for the 12 km (panels 1 and 2) and 14 km altitudes (panels 3 and 4), respectively, for period November 19 – December 03, 2002 (panels 1 and 3) and June 29 – July 13, 2003 (panels 2 and 4). The general structure of the wave activity reveals interesting features, which are dependent on the season. Essentially, the wave activity is uniformly distributed at a height level of 12 km in the equatorial areas. In the North Polar regions, there is a clear seasonal dependence with the maximum activity during the local summer (Fig. 3.5, panels 1 and 2). At the height of 14 km, the wave

DOI:10.2312/GFZ.b103-08040

activity is concentrated in the middle latitudes mainly between 30º and 60º in both hemispheres (Fig. 3.5, panels 3 and 4). The seasonal dependence is evident for some regions: Siberia has a low wave activity in the winter and a high wave activity in the summer at the 14 km altitude. The wave activity above the North Atlantic region is weak during the summer period at the 14 km level (Fig. 3.5, panels 3 and 4). This may be connected to the weak meteorological activity that is dominant in the troposphere within this region in the considered period of time. By contrast with North Atlantic area, the strong activity is seen in the North-Eastern part of the Asian continent and above the North America during period June 29 – July 13, 2003 at the 14 km altitude (Fig. 3.5, panel 4).

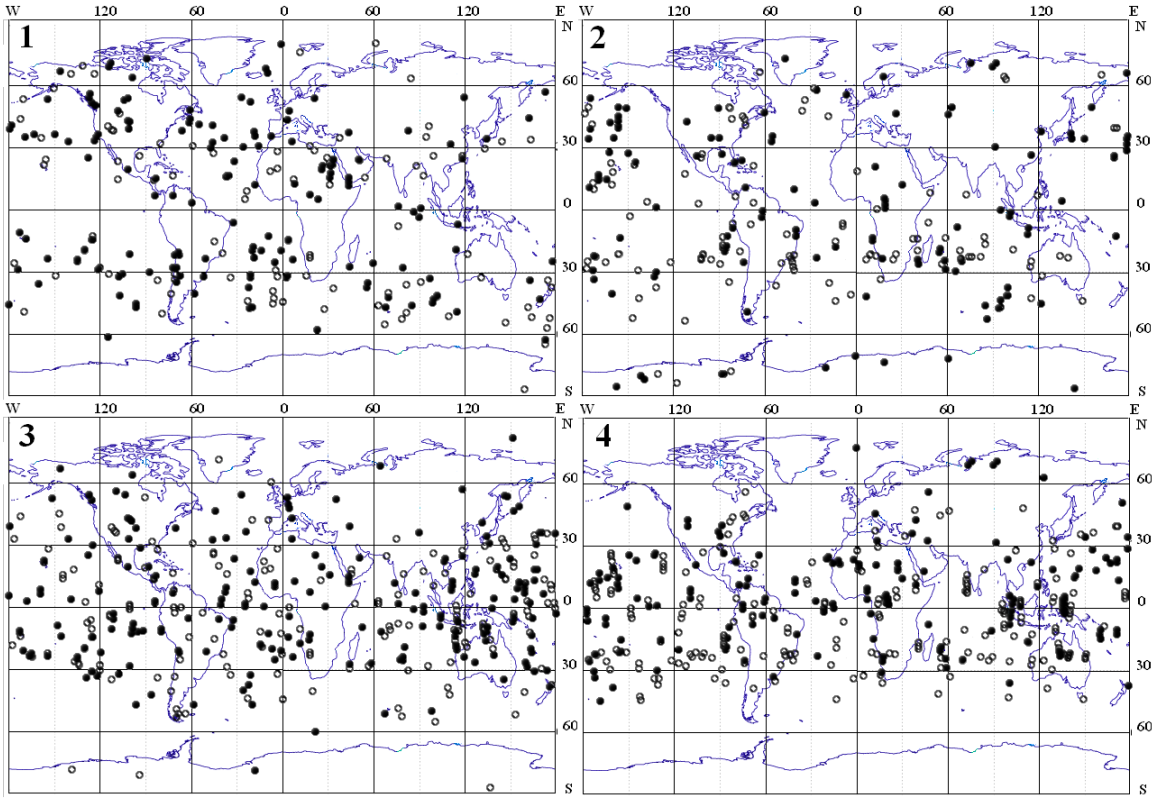

Fig. 3.6. Seasonal and geographical distribution of internal wave activity with amplitudes greater than 0.6 N-units/km in the lower stratosphere for period November 19 – December 03, 2002 (panels 1 and 3) and June 29 – July 13, 2003 (panels 2 and 4). Panels 1 and 2; 3 and 4 correspond to 16 km and 18 km altitude, respectively.

DOI:10.2312/GFZ.b103-08040

The seasonal and geographical distributions of internal wave activity at 16 and 18 km altitudes are demonstrated in Fig. 3.6 for period November 19 – December 03, 2002 (panels 1 and 3) and June 29 – July 13, 2003 (panels 2 and 4). Panels 1 and 2; 3 and 4 in Fig. 3.6 correspond to 16 km and 18 km altitude, respectively. At the 16 km altitude (Fig. 3.6, panels 1 and 2), the latitude dependence is week as compared with the same one at the 14 km altitude (Fig. 3.5, panels 3 and 4). However, some features, resembling concentration of wave activity in the middle latitudes, are seen in Fig. 3.6, panel 1, between the west longitudes 60º and 180º. At the 18 km altitude, the wave activity is concentrated in the tropical areas mainly between the 30º South and 30º North latitudes (Fig. 3.6, panels 3 and 4). Concentrations of wave activity are observed between the 120º and 180º east

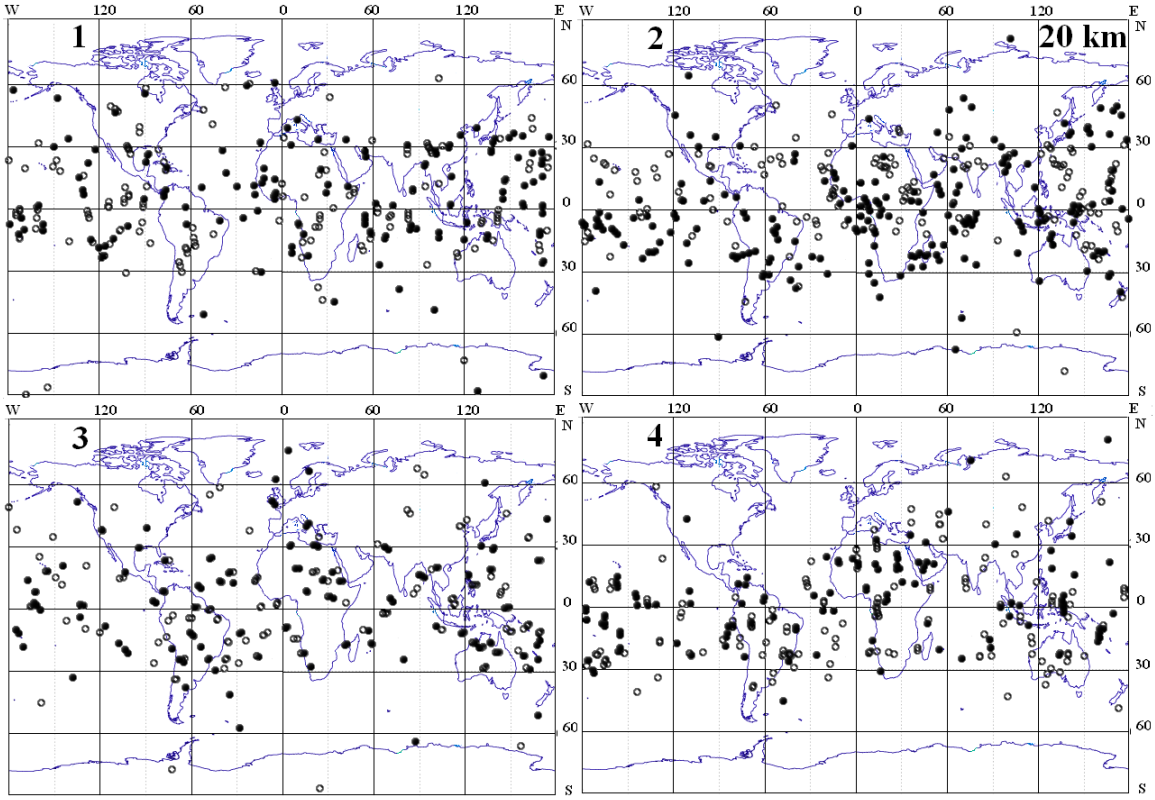

Fig. 3.7. Seasonal and geographical distributions of the wave activity with amplitudes greater than 0.6 N-units/km at the 20 km altitude for periods November 03 – November 18, 2002 (panel 1); December 20, 2002 – January 15, 2003 (panel 2); March 31, 2003 – April 14, 2003 (panel 3); June 29, 2003 – July 13, 2003 (panel 4).

DOI:10.2312/GFZ.b103-08040

longitudes (Fig. 3.6, panel 4). As follows from Fig. 3.5 and Fig. 3.6 the areas with high wave activity are displaced to the equator when the altitude increases from 12 to 18 km. Seasonal and geographical distributions of the wave activity with amplitudes greater than 0.6 N-units/km at the 20 km level are shown in Fig. 3.7 for periods November 03 – November 18, 2002 (panel 1); December 20, 2002 – January 15, 2003 (panel 2); March 31, 2003 – April 14, 2003 (panel 3); and June 29, 2003 – July 13, 2003 (panel 4). As seen from Fig. 3.7, the main part of wave activity is concentrated between ±30º of North latitude. Inside this region, the geographical distribution is changing from nearly uniform, not depending on the longitude (panels 1 and 3, November 2002 and April 2003), up to clearly concentrated in the areas near to Africa and South America (panel 2, December 2002, January 2003). This may be connected with a different origin of the wave activity: e.g. convection mechanism can prevail in the first case (panel 1 and 3 in Fig. 3.6), and the influence of mountain waves can be a cause of concentration of wave activity near Africa and South America (panel 2 in Fig. 3.6). As follows from Fig. 3.5 – 3.7, the GPS occultation signals give important information on geographical and seasonal activity of the internal waves at different altitudes in the atmosphere on a global scale.

DOI:10.2312/GFZ.b103-08040

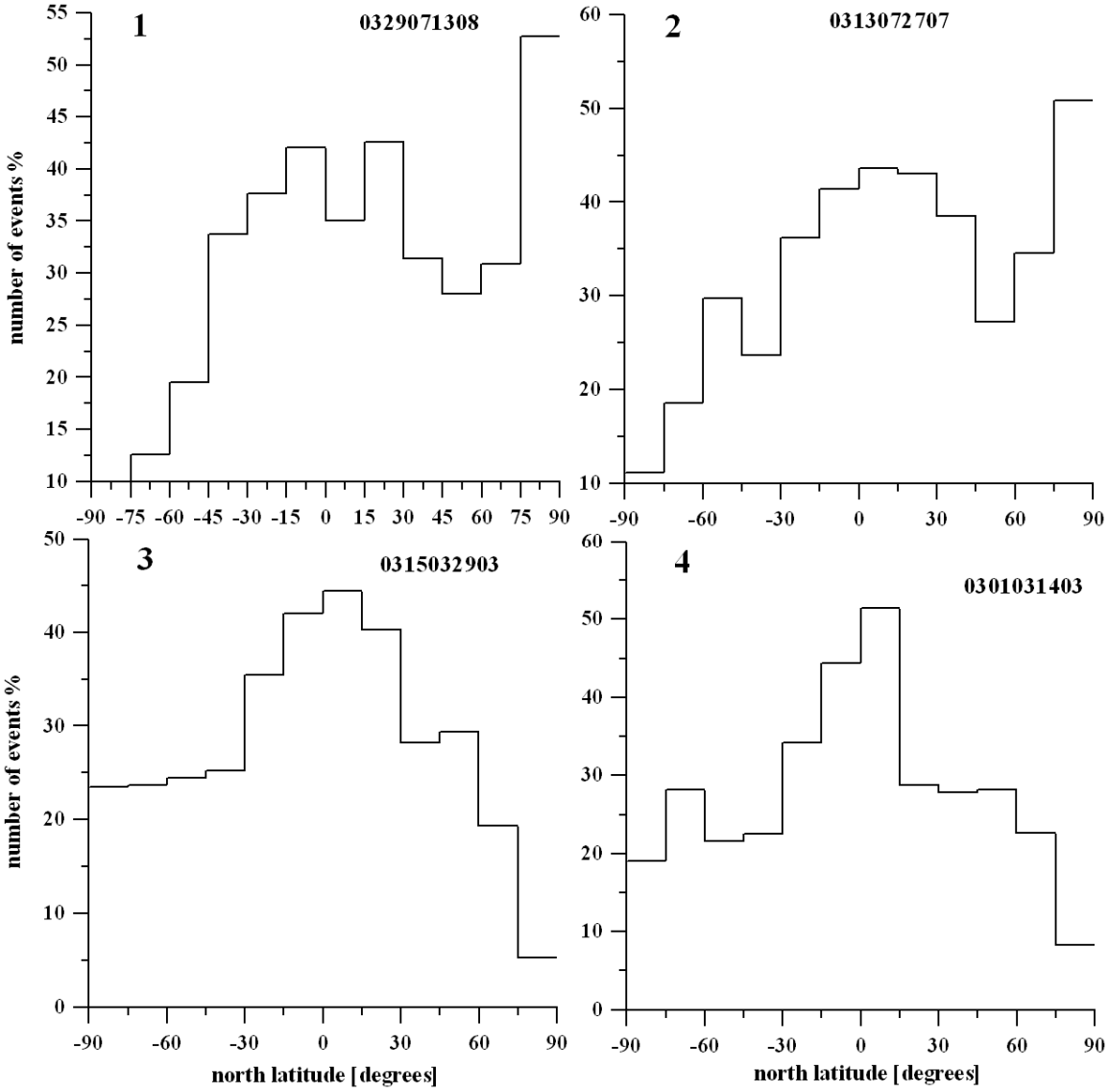

Fig. 3.8. Histograms of the wave activity with amplitudes *q* greater than 0.6 N-units/km at the 12 km level for periods July 29 – August 13, 2003 (panel 1); July 13, 2003 – July 27, 2003 (panel 2); March 15, 2003 – March 29, 2003 (panel 3); and March 01, 2003 – March 14, 2003 (panel 4).

The results of statistical analysis of the latitudinal and seasonal distributions of the wave activity can be seen in Fig. 3.8 – 3.12. The histograms of the latitude distribution of the strong CHAMP RO amplitude events with *q>0.6 N-units/km* for the 12–18 km and with *q>0.24 N-units/km* for the 20 km level are given in Fig. 3.8 – 3.12. The number of the strong RO events normalized by the overall number of the RO events in the corresponding latitude interval 15° in length is displayed on the vertical axes, and the north latitude is plotted along the horizontal axes in Fig. 3.8 – 3.12. Fig.

DOI:10.2312/GFZ.b103-08040

3.8 corresponds to periods from the North Hemisphere late summer time (July 29 – August 13, 2003 (panel 1); July 13, 2003 – July 27, 2003 (panel 2)); till the North Hemisphere early springtime (March 15, 2003 – March 29, 2003 (panel 3); and March 01, 2003 – March 14, 2003 (panel 4)). Following the analysis of the data shown in Fig. 3.8, there is an asymmetry in distribution of the wave activity at the 12 km level in the atmosphere. The maximal wave activity occurs in the summer Arctic polar region (Fig. 3.8, panels 1 and 2). High level of wave activity is also observed in the tropical and subtropical latitudes between 45º South and 45º North latitudes (panels 1 – 4 in Fig. 3.8). There is an apparent increase in the wave activity during early autumn period in the Antarctic polar region (panels 3 and 4 in Fig. 3.8). The minimum wave activity is observed in the polar region's winter period: Arctic, panels 1 and 2, and Antarctic, panels 3 and 4 in Fig. 3.8, respectively.

DOI:10.2312/GFZ.b103-08040

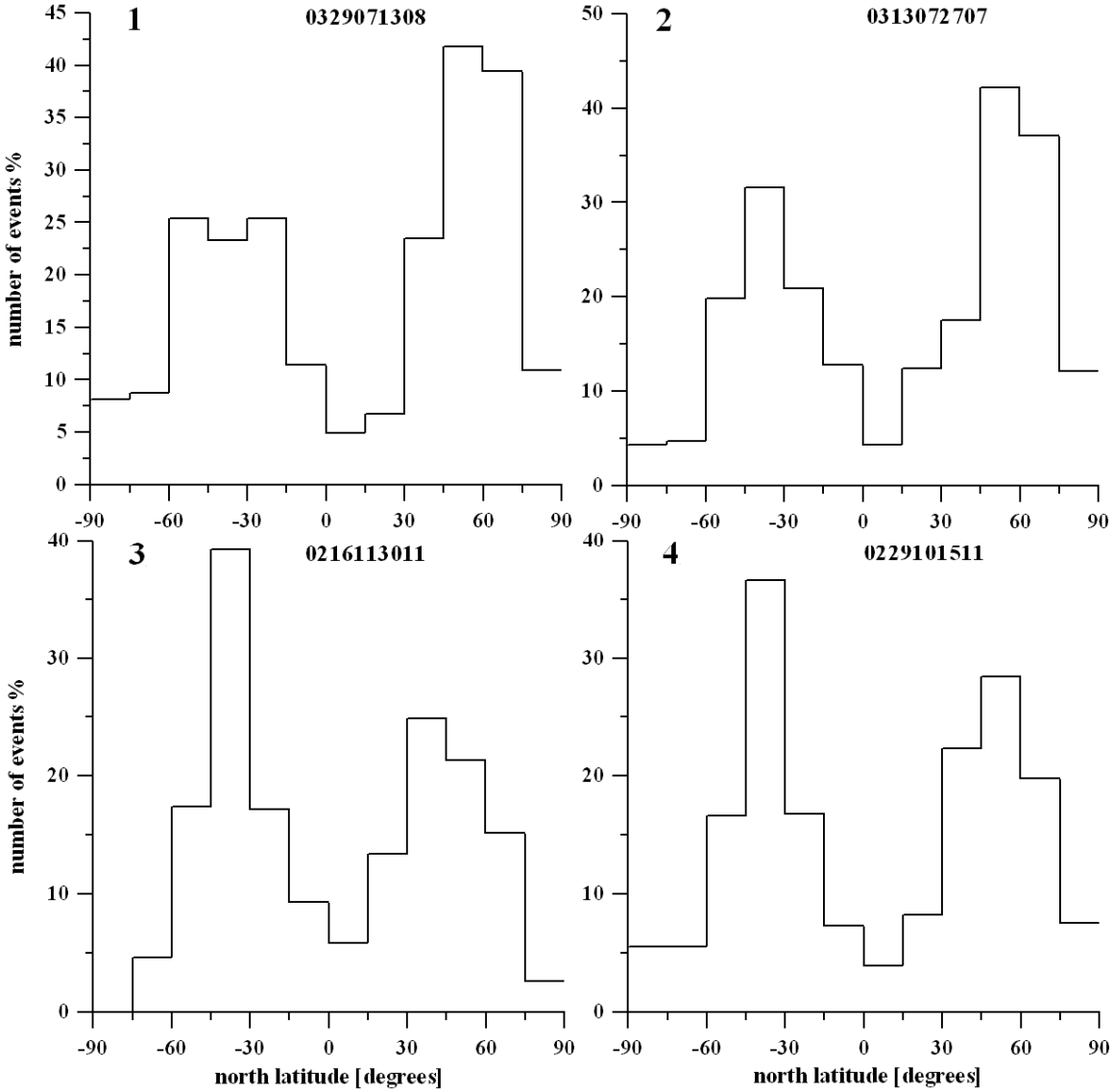

Fig. 3.9. Histograms of the wave activity with amplitudes *q* greater than 0.6 N-units/km at the 14 km level for periods July 29 – August 13, 2003 (panel 1); July 13, 2003 – July 27, 2003 (panel 2); November 16, 2002 – November 30, 2002 (panel 3); and October 29, 2002 – November 15, 2002 (panel 4).

Histograms of the wave activity at the 14 km level with amplitudes greater than 0.6 N-units/km are shown in Fig. 3.9 for periods July 29 – August 13, 2003 (panel 1); July 13, 2003 – July 27, 2003 (panel 2); November 16, 2002 – November 30, 2002 (panel 3); and October 29, 2002 – November 15, 2002 (panel 4). The geographical and seasonal distributions of the wave activity at the 14 km latitude are essentially different from those

DOI:10.2312/GFZ.b103-08040

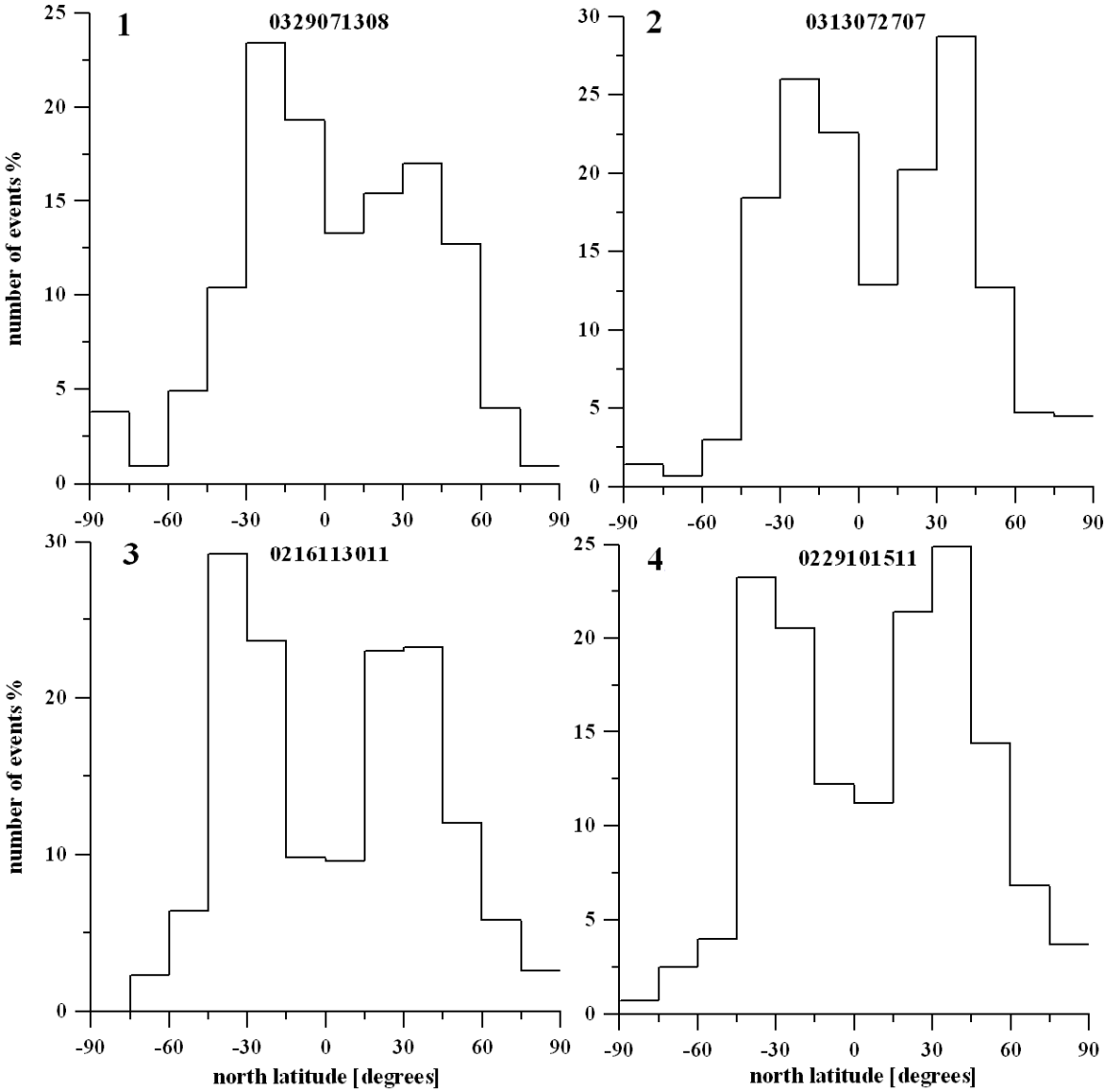

Fig. 3.10. Histograms of the wave activity with amplitudes *q* greater than 0.6 N-units/km at the 16 km level for periods July 29 – August 13, 2003 (panel 1); July 13, 2003 – July 27, 2003 (panel 2); November 16, 2002 – November 30, 2002 (panel 3); and October 29, 2002 – November 15, 2002 (panel 4).

at the 12 km level (Fig. 3.8 and Fig. 3.9, panels 1 – 4). The main part of the wave activity is concentrated from 15º to 60º interval in the middle latitudes in both North and South Hemispheres. In the equatorial areas between ±15º North latitude, one can note a minimal level of wave activity. The amplitude of the wave activity depends on time. For example, it is more intense in the North Hemisphere in July-August 2003 (panels 1 and 2 in Fig. 3.9) and in the South Hemisphere in November 2002 (panels 3

DOI:10.2312/GFZ.b103-08040

and 4 in Fig. 3.9). This indicates an existence of different periods in the global scintillations of the internal wave intensity in the stratosphere.

Histograms of the wave activity at the 16 km altitude with amplitudes greater than 0.6 N-units/km are shown in Fig. 3.10 for periods July 29 – August 13, 2003 (panel 1); July 13, 2003 – July 27, 2003 (panel 2); November 16, 2002 – November 30, 2002 (panel 3); and October 29, 2002 – November 15, 2002 (panel 4). The form of the latitude distribution of the internal wave activity as seen in Fig. 3.10 (panels 1–4) is similar to data shown in Fig. 3.9 (panels 1–4) with the difference that the latitude positions of maximums and minimums in Fig. 3.10 are displaced relative to the locations shown in Fig. 3.9. As follows from comparisons panels 1 and 2, and 3 and 4 in Fig. 3.10, period of variations of the maximums of the wave activity is about of one month.

Histograms of the wave activity at the 18 km altitude with amplitudes greater than 0.6 N-units/km are shown in Fig. 3.11 for periods July 29 – August 13, 2003 (panel 1); July 13, 2003 – July 27, 2003 (panel 2); November 16, 2002 – November 30, 2002 (panel 3); and October 29, 2002 – November 15, 2002 (panel 4). The histograms in Fig. 3.11 (panels 1–4) reveal the concentration of the wave activity in the tropical areas with maximal values at the equator. The seasonal influence is seen in slightly different forms of histograms relevant to the summer and winter hemispheres. Some deflections of main part of histograms in the North and South directions may be seen (Fig. 3.11, panels 1–4). As follows from Fig. 3.11 (panels 1–4), the wave activity at the 18 km altitude depends faintly on time. It follows from Fig. 3.11 that the source of the wave activity at the 18 km altitude is more stable as compared with those at the 12–16 km altitudes.

DOI:10.2312/GFZ.b103-08040

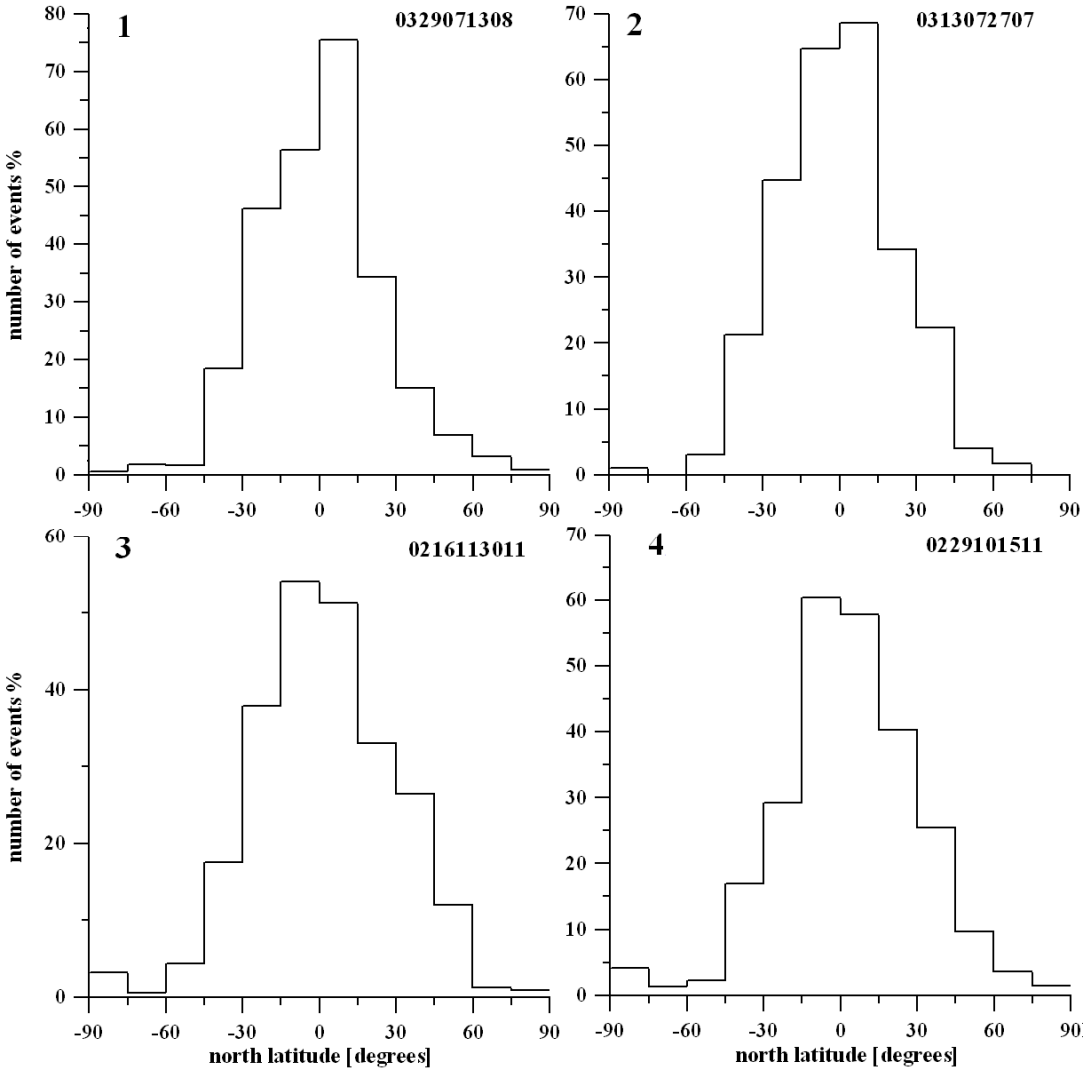

Fig. 3.11. Histograms of the wave activity with amplitudes *q* greater than 0.6 N-units/km at the 18 km level for periods July 29 – August 13, 2003 (panel 1); July 13, 2003 – July 27, 2003 (panel 2); November 16, 2002 – November 30, 2002 (panel 3); and October 29, 2002 – November 15, 2002 (panel 4).

Histograms of the wave activity at the 20 km altitude with amplitudes greater than 0.6 N-units/km are shown in Fig. 3.12 for periods July 29 – August 13, 2003 (panel 1); July 13, 2003 – July 27, 2003 (panel 2); November 16, 2002 – November 30, 2002 (panel 3); and October 29, 2002 – November 15, 2002 (panel 4). At the 20 km altitude, the wave activity is principally bounded in the ±30º North latitude interval. It does not indicate the essential seasonal dependence as seen in Fig. 3.12, panels 1–4. However, one may observe

DOI:10.2312/GFZ.b103-08040

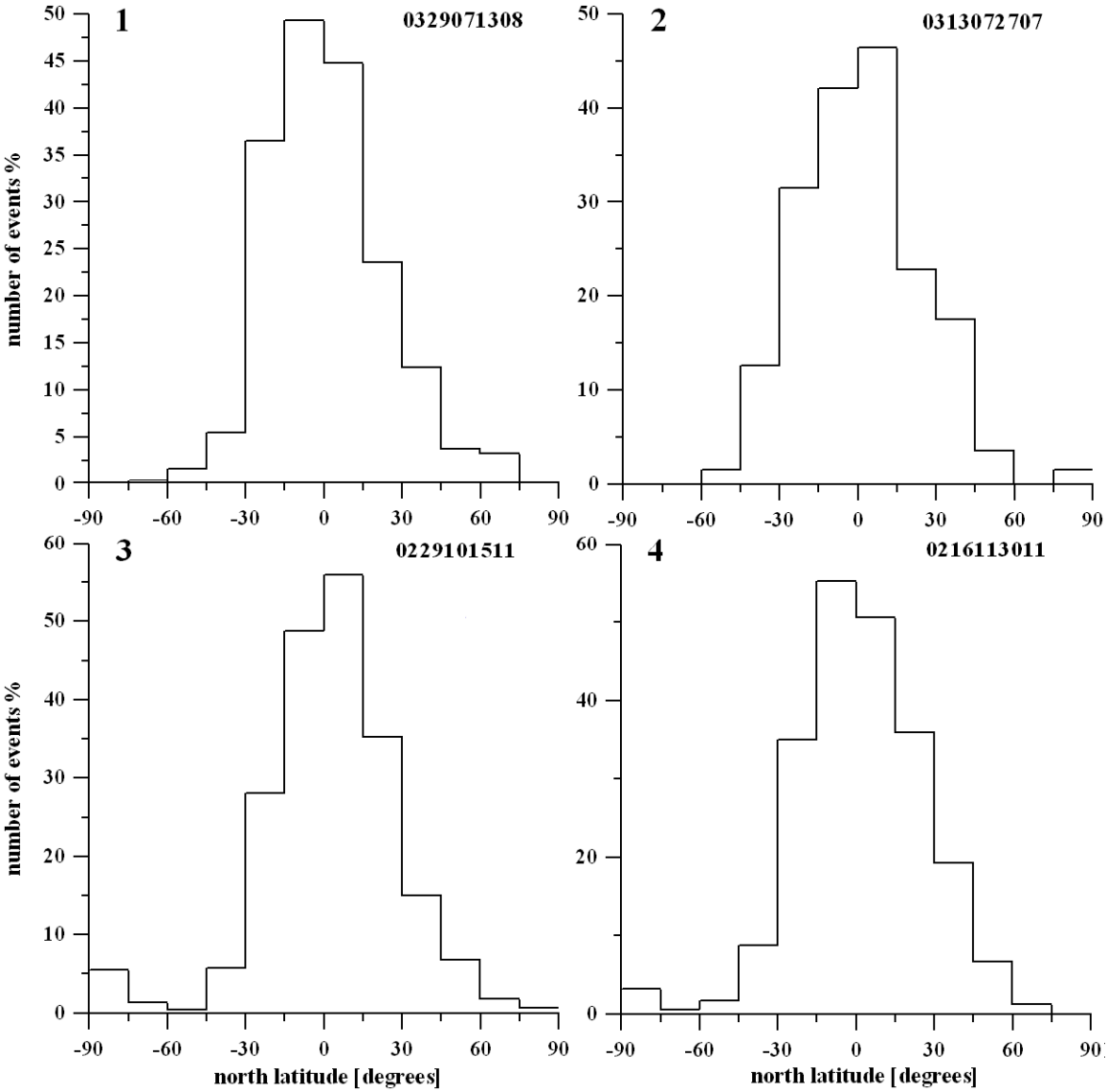

Fig. 3.12. Histograms of wave activity with amplitudes *q* greater than 0.24 N-units/km at the 20 km level for periods July 29 – August 13, 2003 (panel 1); July 13, 2003 – July 27, 2003 (panel 2); November 16, 2002 – November 30, 2002 (panel 3); October 29, 2002 – November 15, 2002 (panel 4).

small changes in the form of histogram maximums with period about one month (panels 1, 2; and 3, 4 in Fig. 3.12). The origin of these variations can be connected with different activity of the wave sources at the 20 km altitude in the atmosphere.

As follows from the analysis of Fig. 3.8 – 3.12, the latitudinal histograms can serve as important tools to better understand the general features of the internal wave activity in the atmosphere as compared with the detailed maps of the wave activity

DOI:10.2312/GFZ.b103-08040

shown in Fig. 3.5 – 3.7. A more detailed analysis of the global pictures of the internal wave activity and the study of the possible connections with the meteorological phenomena in the atmosphere are the tasks of the future.

As followed from Fig. 3.5–3.12, the wave activity in the atmosphere over a global scale can be characterized by a new RO index β: probability of strong wave amplitudes exceeding the fixed level of the vertical gradient of refractivity *q*. This index has a global importance for the description of the wave activity in the atmosphere as seen in Fig. 3.13– 3.18. The data demonstrated in Fig. 3.13– 3.18 have been obtained as a result of analysis of the CHAMP RO data for the time period 2001 – 2003. The magnitude β has been defined in this analysis as a ratio of numbers of intense wave amplitude greater than $q>0.6$ *N-units/km* for 12–16 km altitudes and with $q>0.24$ *N-units/km* for 18–26 km altitudes to general numbers of the measurements over the entire Earth. The value β is marked at the vertical axis in Fig. 3.13– 3.18. The smooth curves are obtained as an approximation of the experimental data (broken lines) by the least squares method. The used data are relevant to a three year interval September 2001–2003, without three periods: (1) from October 15, 2001 to February 28, 2002; (2) from May 16, 2002 to October 31, 2002; and (3) from January 01 to January 12, 2003.

A comparative analysis of the wave activity in the North and South Hemispheres of the Earth with a global coverage can be made by use of data shown in Fig. 3.13–3.16.

DOI:10.2312/GFZ.b103-08040

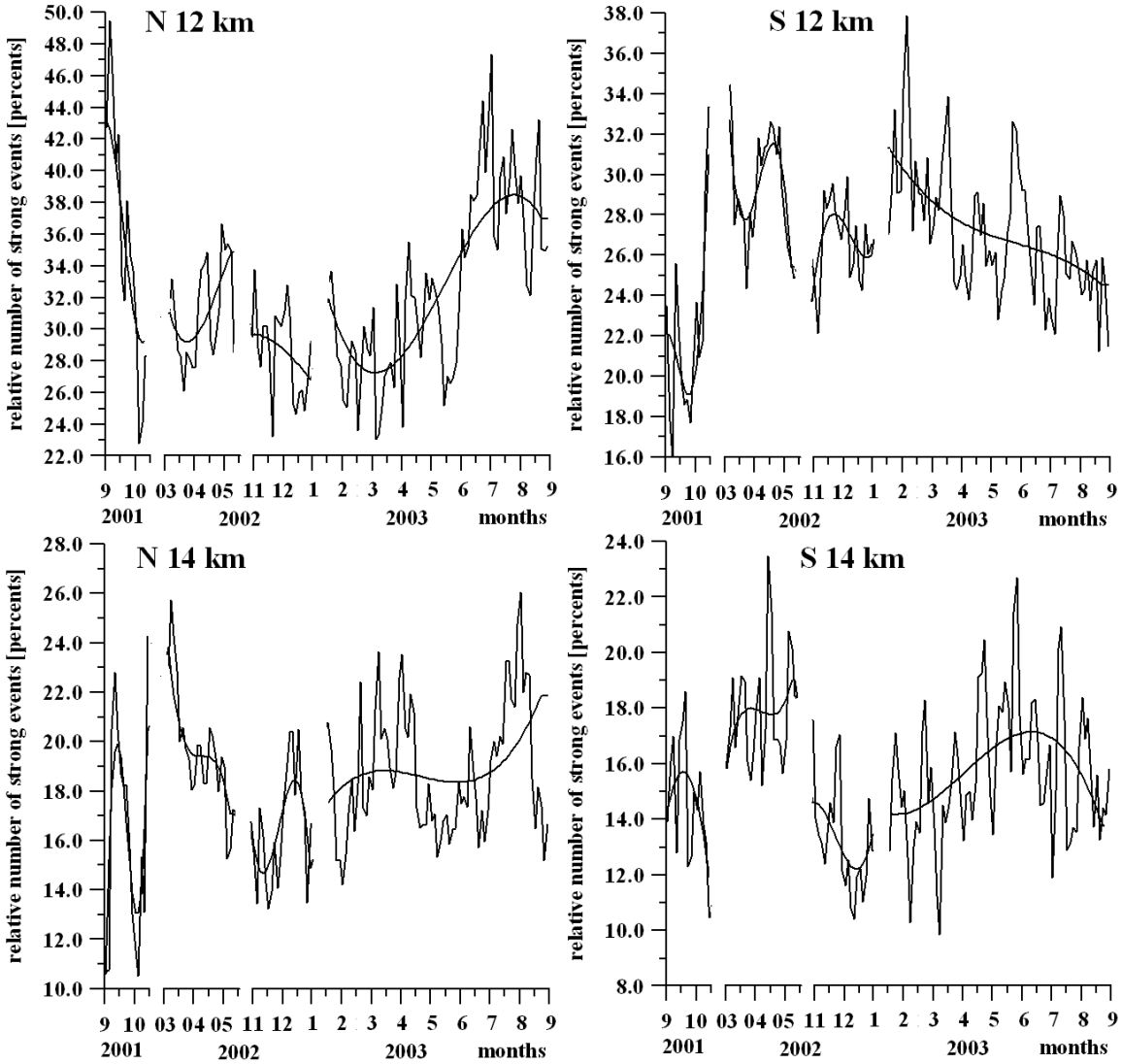

Fig. 3.13. Changes in internal wave activity (averaged over the Earth globe) during 2001 – 2003 at different altitudes in the atmosphere: 12 km and 14 km (top left and right panels, respectively), 16 and 18 km (bottom left and right panels, respectively).

The left panels in Fig.s 2.13 – 2.16 correspond to different altitudes in the 12–26 km interval in the North Hemisphere, and the right panels in the South Hemisphere. The opposite phase of the wave activity changes are clearly seen at the altitude 12 km (Fig. 3.13, top left and right panels). In the North Hemisphere, the maximum of the wave activity is observed in the beginning of September 2001. Then, the wave activity is diminishing till the middle of October 2001. In the South Hemisphere minimum of the wave activity is

DOI:10.2312/GFZ.b103-08040

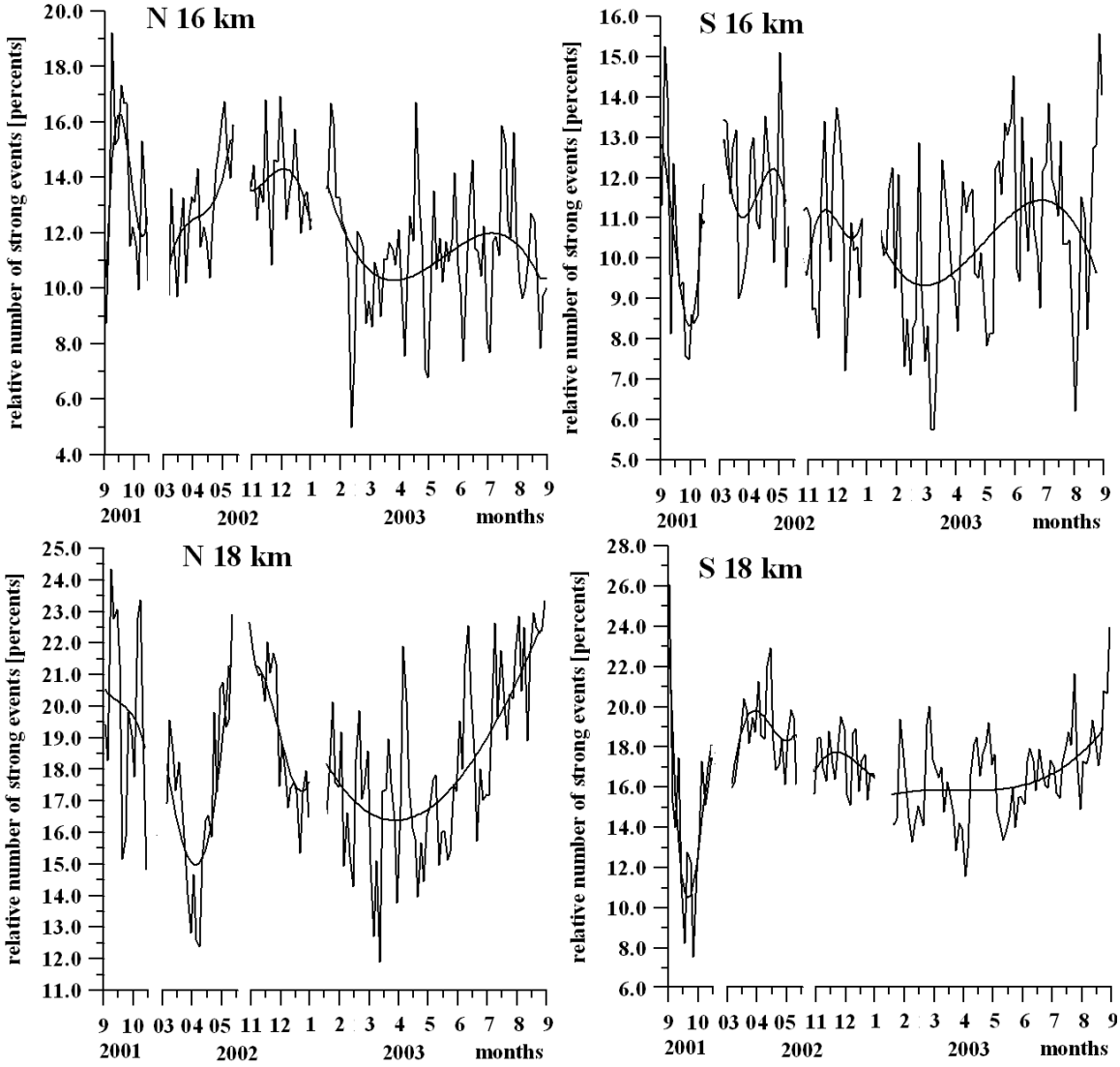

Fig. 3.14. Changes in internal wave activity (averaged over the Earth globe) during 2001 – 2003 at different altitudes in the atmosphere: 12 km and 14 km (top left and right panels, respectively), 16 and 18 km (bottom left and right panels, respectively).

is achieved in the beginning of October 2001. Then, the wave activity is increasing till the middle of October 2001. In both cases, there are significant evidences of two months periodicity in the wave activity during September-October 2001 (Fig. 3.13, top left and right panels). Two months periodicity can be noted for temporal periods March–May 2002. The maximum of the wave activity is

DOI:10.2312/GFZ.b103-08040

achieved

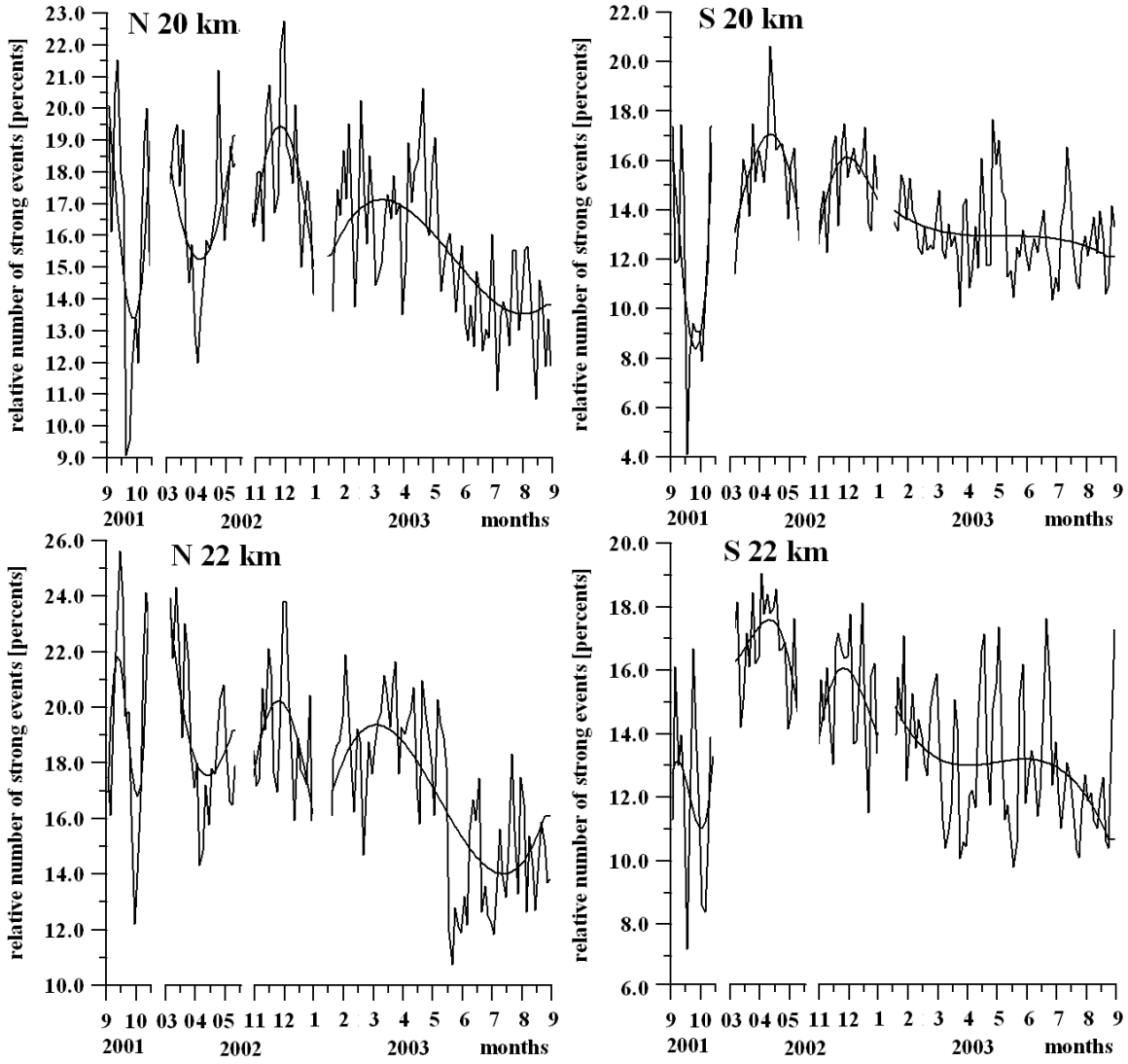

Fig. 3.15. Changes in internal wave activity (averaged over the Earth globe) during 2001 – 2003 at different altitudes in the atmosphere: 12 km and 14 km (top left and right panels, respectively), 16 and 18 km (bottom left and right panels, respectively).

in the South Hemisphere one half of month earlier than that in the North Hemisphere. In the temporal interval November 2002 – September 2003, the annual cycle is seen both in the North and South Hemispheres. In the North Hemisphere, the annual cycle is strongly pronounced and the phase of cycle is different by one half of period as compared with the

DOI:10.2312/GFZ.b103-08040

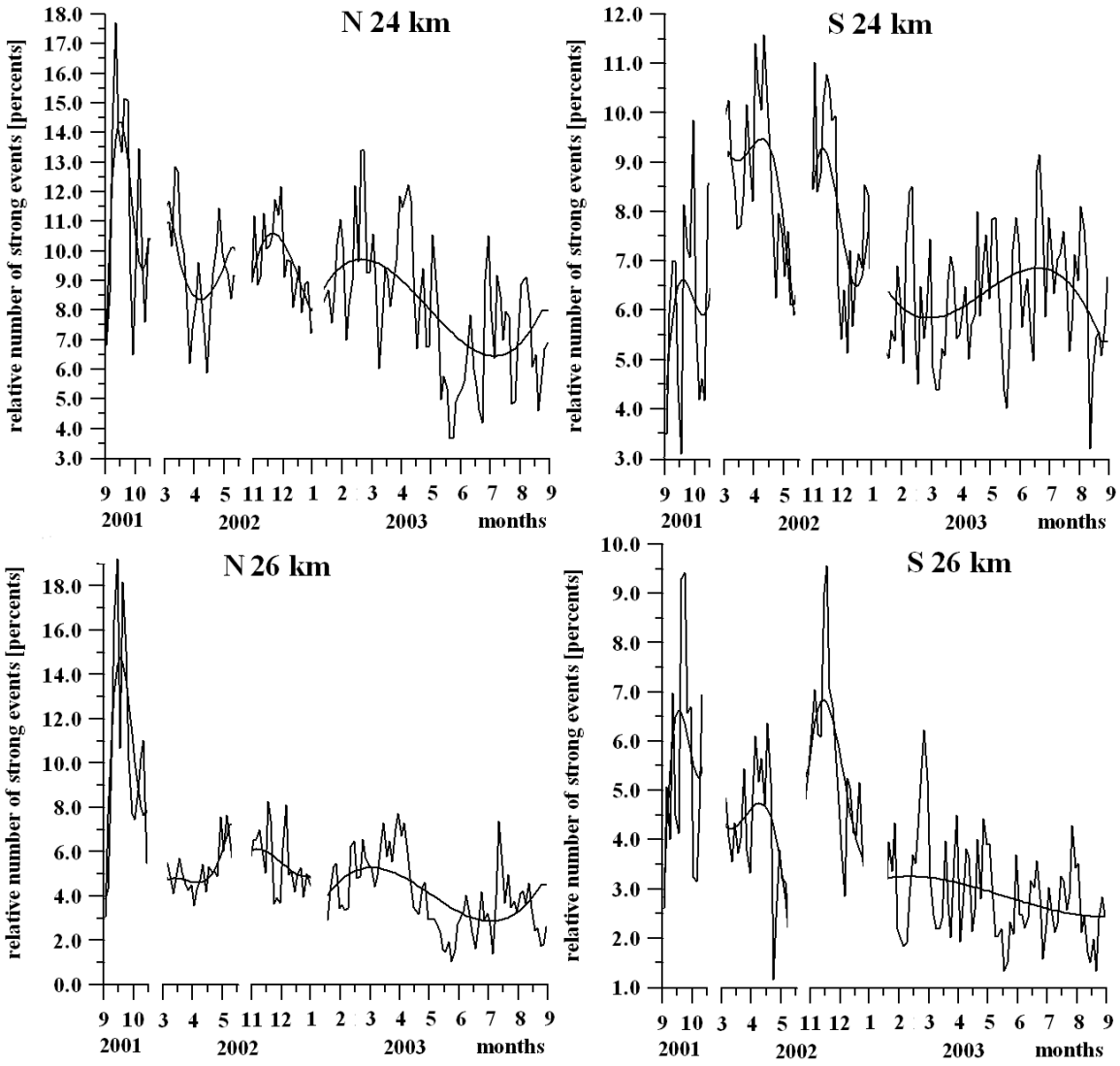

Fig. 3.16. Changes in internal wave activity (averaged over the Earth globe) during 2001 – 2003 at different altitudes in the atmosphere: 12 km and 14 km (top left and right panels, respectively), 16 and 18 km (bottom left and right panels, respectively).

South Hemisphere (Fig. 3.13, top left and right panels). The average level of the wave activity in the North Hemisphere at the altitude 12 km is about of 20% higher than that in the South Hemisphere. At the altitude 14 km, one can see in Fig. 3.13 (bottom left and right panels) the same regularities as at the height 12 km besides displacement in the cycles nearly by one forth of the period.

DOI:10.2312/GFZ.b103-08040

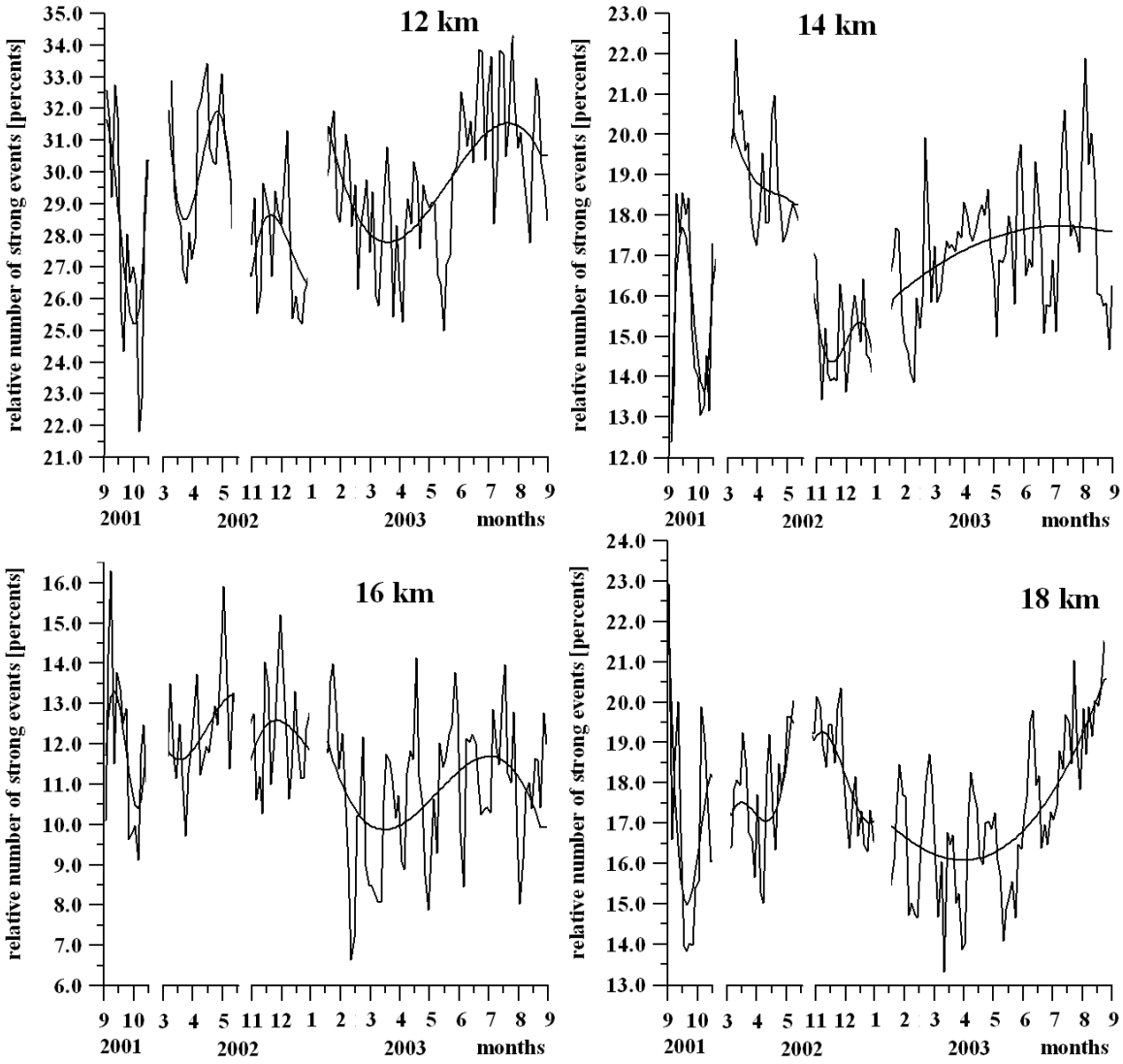

Fig. 3.17 . Changes in internal wave activity (averaged over the Earth globe) during 2001 – 2003 at different altitudes in the atmosphere: 12 km and 14 km (top left and right panels, respectively), 16 and 18 km (bottom left and right panels, respectively).

At the altitudes 16 and 18 km (Fig. 3.14, left and right panels), the temporal dependences of the wave activity are nearly the same in the South and North Hemispheres as opposite to the levels 12 and 14 km (Fig. 3.13, left and right panels). The annual cycle is seen during period November 2002 – September 2003 in both Hemispheres with nearly the same phase. The difference between wave activity in the North and South Hemispheres is greater during 2001 – 2002 as compared with 2003. The altitudes 16 km and 18 km can

DOI:10.2312/GFZ.b103-08040

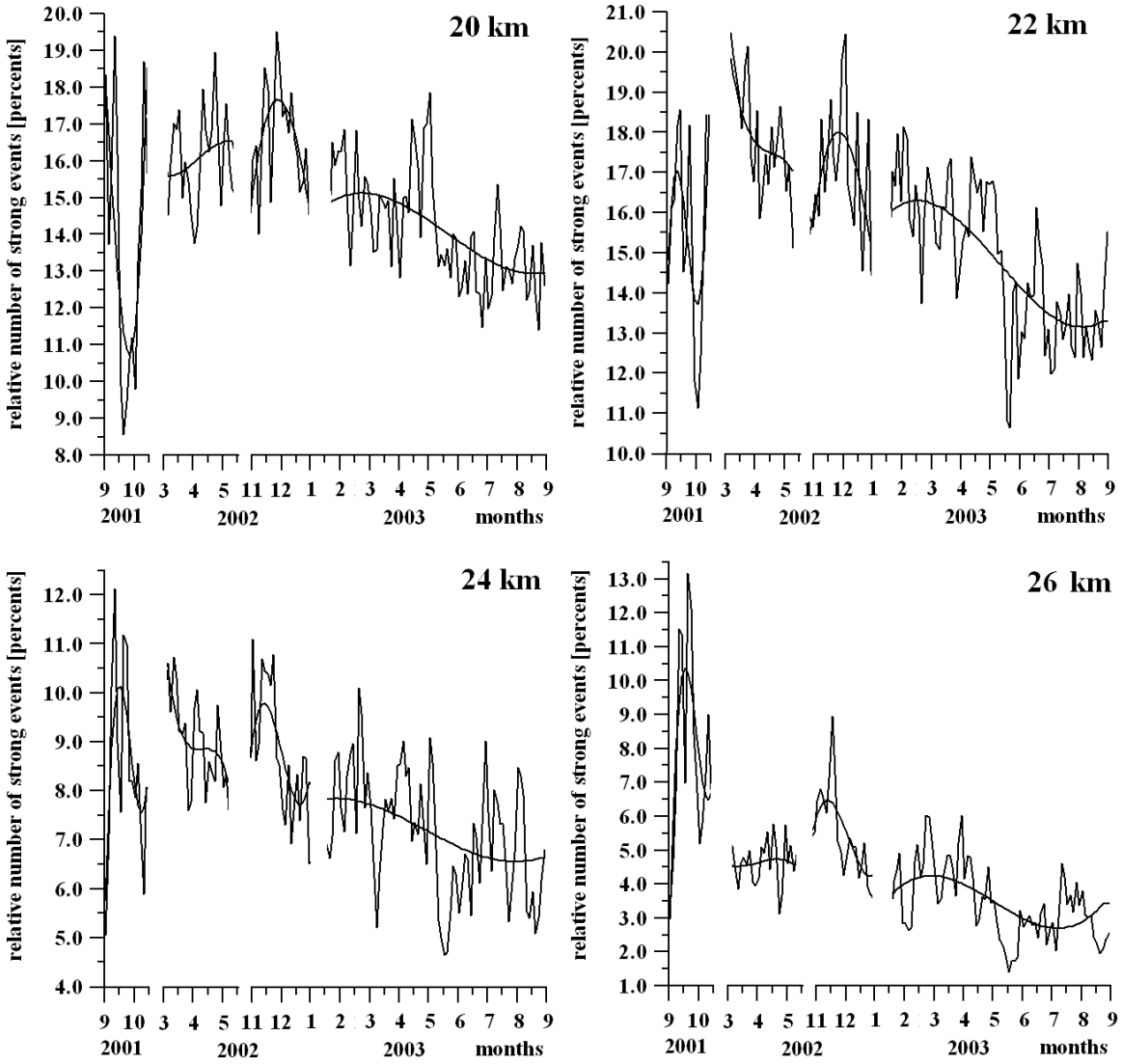

Fig. 3.18. Changes in internal wave activity (averaged over the Earth globe) during 2001 – 2003 at different altitudes in the atmosphere: 20 km and 22 km (top left and right panels, respectively), 24 and 26 km (bottom left and right panels, respectively).

be considered as intermediate to the 12 km and 20 km altitudes.

At the altitudes 20 km–25 km, the wave activity in the North and South Hemispheres are very similar (Fig. 3.15 and Fig. 3.16). The phases of two-month and annual periodicity are nearly the same. However, their amplitudes are different. Also, the level of the wave activity in the North Hemisphere is higher than in the South Hemisphere (Fig. 3.15 and Fig. 3.16) by 10% – 15% similar to those at the heights 16 km and 18 km (Fig. 3.14).

DOI:10.2312/GFZ.b103-08040

As follows form analysis of data shown in Fig. 3.13- 3.16, there are some differences in the wave activity in the North and South Hemispheres: (1) an average level of the wave activity is about of 20% higher in the North Hemisphere; (2) there are displacements in the phase of annual and two-month periodicities at level 12 km. However, there are common features in the wave activity in the North and South Hemispheres. In both Hemispheres, the annual and two-month periodicities in the variations of wave activity are seen. The maximum of the wave activity is clearly seen in September – October 2001. There is a gradual diminishing in the wave activity from 2001 to 2003, especially significant at the altitudes 20–26 km. The origin of this diminishing is not clear. It may be connected with different causes including diminishing in solar activity observed from 2001 up till 2003. As follows from the analysis of the wave activity at different altitudes in the North and South Hemispheres, the parameter of the wave activity β may be considered as a promising index, which is useful for description of the wave activity at different altitudes over Northern and Southern Hemispheres of the Earth.

The seasonal and annual changes of the wave activity are seen at all altitudes 12–26 km in Fig. 3.17 and Fig. 3.18. For example, changes with period of about 12 months are clearly seen at the altitudes 12, 16, and 20–26 km (Fig. 3.17 and Fig. 3.18) for period January – September 2003. The phases of one-year oscillations at altitudes 12 and 16 km are opposite to the phases of the wave activity variations at the heights 20–26 km (Fig. 3.17 and Fig. 3.18). The wave activity behavior at the altitudes 14 and 18 km is different from that at the heights 12, 16, and 20–26 km. The wave activity at the height 14 and 18 km is increasing when the time goes to the end of the considered period – September 2003. At the altitudes 12, 16, and 20–26 km, the wave activity is gradually diminishing by 10% – 40% when the time changes from September 2001 to September 2003. This diminishing may be connected with changes in the intensity of

DOI:10.2312/GFZ.b103-08040

the meteorological processes, types of the atmospheric circulations, and, very likely, with reduction in solar activity in the considered period of time.

4. S_4 INDEX AND MAPS OF THE IONOSPHERIC ACTIVITY

4.1. CONNECTION BETWEEN S_4 INDEX AND PHASE ACCELERATION

As stated above the amplitude scintillations are very important because in the case of layered structures they are directly connected from one side – with the phase acceleration and from another side – with the vertical gradients of refractivity in the plasma layers. The emphasis in the RO studies is now concentrating on the phase variations of the RO signals in the trans-ionospheric links because direct connection with total electron content [*Hocke and Tsuda*, 2001; *Hocke et al.*, 2001, 2002; *Wickert et al.*, 2004b] and on analysis of the amplitude variations owing to their dependence on the vertical gradient of refractivity [*Vorob'ev et al.*, 1999; *Igarashi et al.*, 2001, 2002; *Gorbunov et al.*, 2002; *Sokolovskiy et al.*, 2002; *Pavelyev et al.*, 2002, 2003, 2005a; *Liou et al.*, 2002, 2003, 2005]. However, the statistical analysis of the amplitude variations of the RO signals, having different origin, is now in the beginning stage [*Wickert et al.*, 2004a, 2004 b; *Pavelyev et al.*, 2005b, *Wu et al.*, 2005]. *Wu et al.* [2005] directed special attention toward the amplitude and phase variations caused by sporadic E_s layers in the ionosphere and excluded from analysis the amplitude and phase variations caused by the other factors. *Wickert et al.* [2004a, 2004b], *Pavelyev et al.* [2005b] considered the amplitude variations as a general characteristic of the ionospheric influence on the RO signal. They concluded that (1) the S_4 index of amplitude variations can be considered as an index of the ionospheric plasma influence on the RO signal in the trans-ionospheric satellite-to-satellite links in a like fashion with the S_4 index introduced formerly for the trans-ionospheric satellite-to-Earth links [e.g.,

DOI:10.2312/GFZ.b103-08040

Yeh and Liu, 1982]; (2) the S_4 index can be used in the satellite-to-satellite links as a radio-physical index of activity of plasma disturbances in the ionosphere; and (3) the relative number of GPS RO events with high values of the S_4 index in the satellite-to-satellite links can be used to establish a connection between the intensity of plasma disturbances and solar activity.

Below we will follow the point of view introduced by *Wickert et al.* [2004a], [2004b], *Pavelyev et al.* [2005b] for the analysis of the influence of the ionospheric plasma on the RO signal and revealing connections of the amplitude variations with solar activity. We will describe the amplitude variations of the RO signal by the magnitude of the S_4 scintillation index [e.g., *Yeh and Liu*, 1982; *Aarons*, 1982]:

$$S_4 = [<(I - <I>)^2>]^{1/2} / <I>, \quad (4.1)$$

where <> is the average relevant to the height $h(T)$ above 40 km, and $I(t)$ is the intensity of the RO signal. The S_4 scintillation index can be easily connected with the refraction attenuation $X-1$ and the phase acceleration variations a (Pavelyev et al., 2007, equation (1.15)):

$$S_4 = [<(X-1)^2>]^{1/2} = m[<a^2>]^{1/2}. \quad (4.2)$$

The relationships (4.2) give the new connection of the S_4 scintillation index with the phase accelerations, which may have a general significance. In particular, this connection can be important for the trans-ionospheric satellite-to-satellite and satellite-to-Earth links. It allows recalculating the phase variations in the RO signal to the amplitude variations and vice versa. This allows establishing the quantitative connection between the phase variations and amplitude variations of radio waves in the trans-ionospheric satellite-to-satellite links and, possibly, in satellite-to-Earth links. Below we will indicate that the S_4 scintillation index is a key parameter connecting the

DOI:10.2312/GFZ.b103-08040

amplitude and phase variations of the RO signal with space weather conditions on a global scale.

4.2. DEPENDENCE OF CHAMP RO SIGNAL ON SOLAR EVENT OCTOBER 28-31, 2003

Influence of sporadic solar activity can be considered in the case of solar flare during October 29 – 31, 2003. To analyze in more details the geographic and time distributions of the amplitude scintillations in the RO signal, we treat about 2000 CHAMP RO events from October 27 to November 9, 2003. The histograms of the integral distribution of the S_4 index, which have been obtained for each day of measurements, are shown in Fig. 4.1. The ratio R_i of the number of cases with the amplitude S_4 larger, than the value plotted on the abscissa, to the total number of measurements for the corresponding day, is plotted on the ordinates in Fig. 4.1. The histograms in the right-hand panel of Fig. 4.1 correspond to data of S_4 measurements on October 29–31, as well as on October 28, November 1, and November 4, 2003, performed during relatively intense and weak disturbances in the RO signal, respectively. The initial histogram values for the entire period of observations are coincident and correspond to an amplitude S_4 of ~2.8%, which depends on the level of fluctuations of receiver noise. Three days, October 29–31, with considerably higher S_4 levels than on the remaining days are distinguished in Fig. 4.1. The histograms for this time interval are much higher than for the remaining days.

DOI:10.2312/GFZ.b103-08040

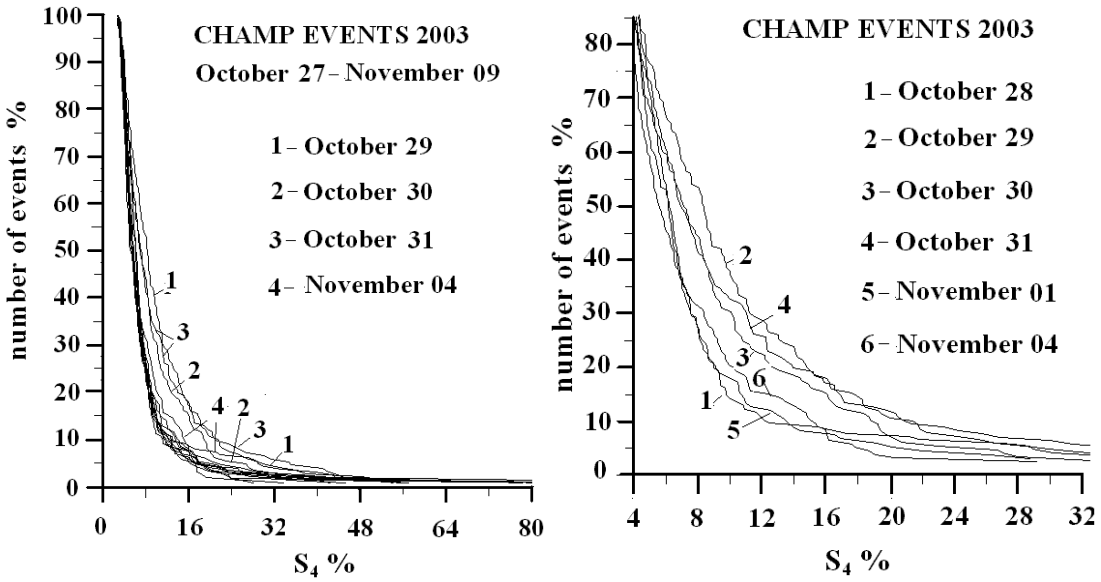

Fig. 4.1. Histograms of the S_4 index variations corresponding to perigee altitudes of the CHAMP RO signal trajectory (point *T* in Fig. 1) higher than 40 km. The curves corresponding to the histograms for October 27 and 28 and for November 1–3 and 5–9, 2003, are almost indiscernible in the left-hand panel. The right-hand panel demonstrates the histograms (curves 1-6) in more details.

The most difference between the histograms is observed in the 5%–19% interval of the S_4 index with maximum about of 12% (Fig. 4.1, left and right panels). The value 12% of the S_4 index is by a factor 4.3 greater than the level of the receiver's noise. Therefore, in the CHAMP RO experiments at the first GPS frequency the values of S_4 index in the 5%–19% interval can be considered as the most sensitive for estimation of the ionospheric influence on the RO signal. An analysis performed makes it possible to introduce the RO index of ionospheric activity R_i.

DOI:10.2312/GFZ.b103-08040

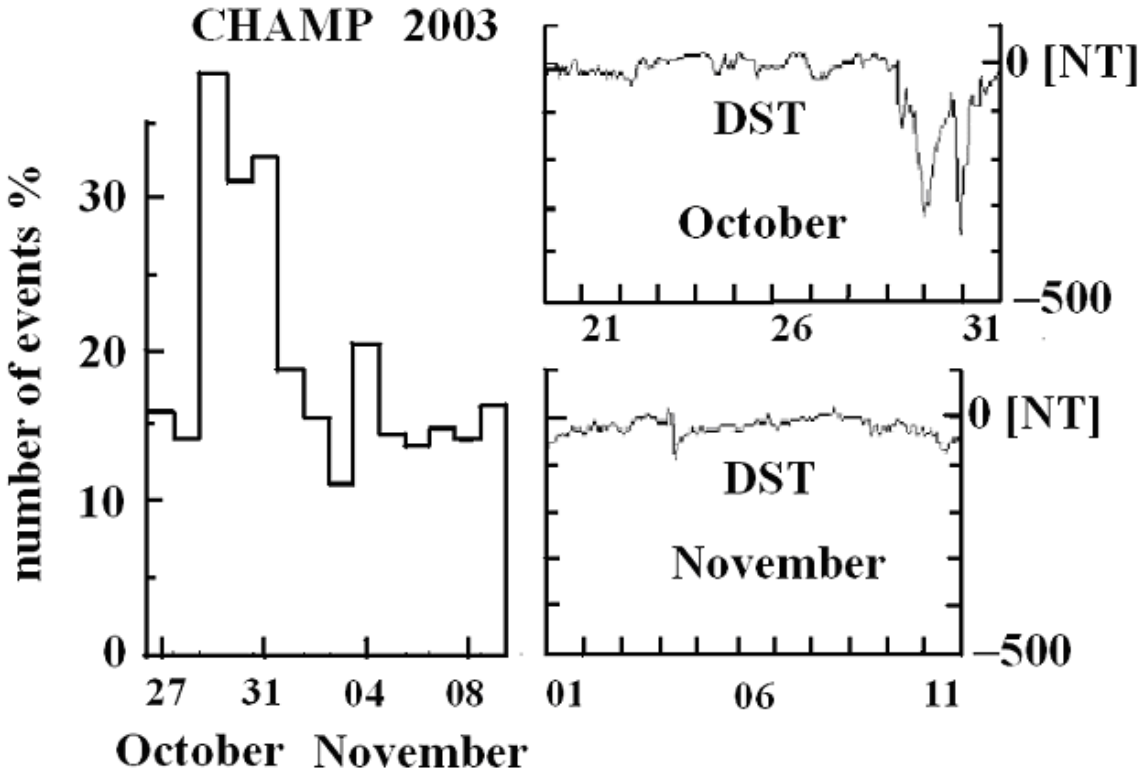

Fig. 4.2. Left-hand panel: the histogram of the RO events with S_4 index higher than 5% according to data of the CHAMP measurements performed from October 27 to November 9, 2003. Right-hand panel: the dynamics of the hourly index of the solar wind (*DST*, nT) according to data from http://swdcwww.kugi.kyoto-u.ac.jp/aeasy/index.html for October 26–31 (upper part of the right panel) and November 1–11, 2003 (bottom part of the right panel).

By definition, the R_i index is equal to the ratio of the number of RO events with the S_4 value of the RO signal at $h > 40$ km larger than three – four magnitudes of S_4 caused by technical noise of the transmitter– receiver system to the total number of RO events for a certain time interval (e.g., for a day). The R_i variations for the period from October 27 to November 9, 2003 are shown in Fig. 4.2 (left-hand panel). The histograms in Figs. 6 and 7 (left-hand panel) are in good agreement with the variations in the hourly index of the solar wind magnetic field (*DST*, nT) obtained from data of the satellite measurements. During October 26–28 and November 1–3 and 5–9, the *DST* index was almost constant, which corresponds to decreased values of the integrated distributions in the histograms (Fig. 4.1 and Fig. 4.2, left-hand panel). Abrupt changes in the index of the solar wind magnetic field were observed on October 29–31 and November 4,

DOI:10.2312/GFZ.b103-08040

which corresponds to a twofold increase in the number of events with increased (larger than 12%) S_4 index of the variations in the RO signal intensity (Fig. 4.2, left-hand panel).

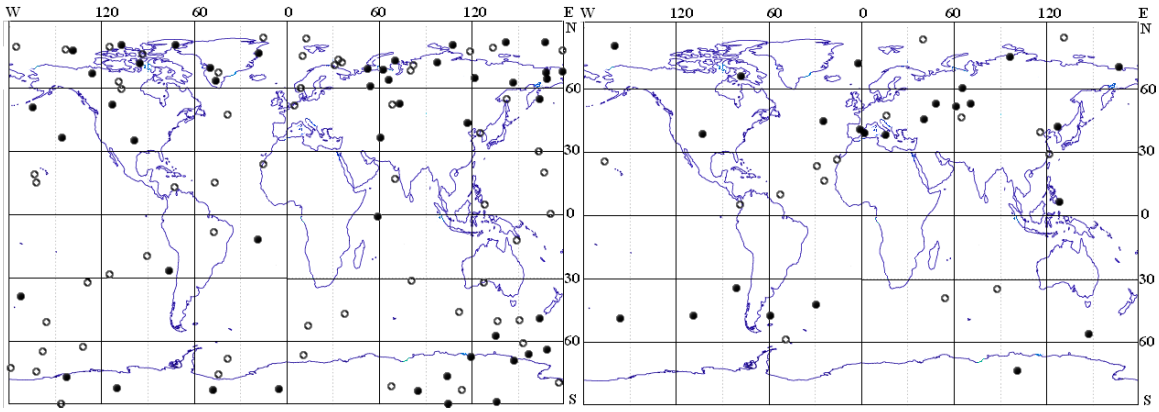

Fig. 4.3. The geographic distribution of the RO events with S_4 index value higher than 12% on October 26 – 28, 2003 (right panel) and October 29 – 31, 2003 (left panel). Open and filled circles correspond to the nighttime (from 2000 to 0800 LT) and daytime (from 0800 to 2000 LT) local time intervals, respectively.

The geographic distributions of increased (greater than 12%) S_4 index of the variations in the RO signal amplitude on October 26–28 (right panel) and on October 29–31, 2003 (left panel) are compared in Fig. 4.3. According to Fig. 4.3, the general number of events with S_4 index values greater than 12% increased by 2.5 times in period October 29 – 31 as compared with period October 26 – 28. The most important changes occurred mainly in the Polar Regions in Antarctica and in the Northern Hemisphere near geomagnetic South and North poles. It is interesting to note that ionospheric disturbances (Fig. 4.3, left and right panels) are concentrated above continents near coasts and in mountain regions (eastern coast of Asia, Japan, Kamchatka, western regions of South America, etc.). This corresponds to observations made previously by *Hocke et al.* [2001].

DOI:10.2312/GFZ.b103-08040

4.3. GEOGRAPHICAL AND SEASONAL DISTRIBUTIONS OF CHAMP RO EVENTS WITH INTENSE AMPLITUDE VARIATIONS

The geographical distributions of the intense ionospheric events (with the S_4 index greater than 0.12) for all types of the amplitude scintillations in the CHAMP RO signals at 1575.42 MHz are demonstrated in Fig. 4.4 and Fig. 4.5. The distributions of the ionospheric events indicate that they are concentrated in some regions (e.g., the equatorial and geomagnetic North and South polar zones in Fig. 4.4 and Fig. 4.5). High activity in some equatorial regions may be connected with the evening ionospheric disturbances that arise after sunset, 20-24 hours of local time, in accordance with the earth-based measurements reviewed earlier [e.g., *Yeh and Liu,* 1982]. Note that geographical distributions of the night- and day-time events are very different. The day-time events prevail in the North and South Polar zones. The night-time events are concentrated mainly in the equatorial and moderate latitude areas. The most significant difference in the geographical distributions of night-time (open circles) and day-time (closed circles) events is observed in April 2004 (Fig. 4.5, right bottom panel), and in October 2002 (Fig. 4.4, right top panel). This indicates the different origin of the day-time and night-time plasma disturbances in the ionosphere. The number and geographical distributions of intense ionospheric events depend on time.

DOI:10.2312/GFZ.b103-08040

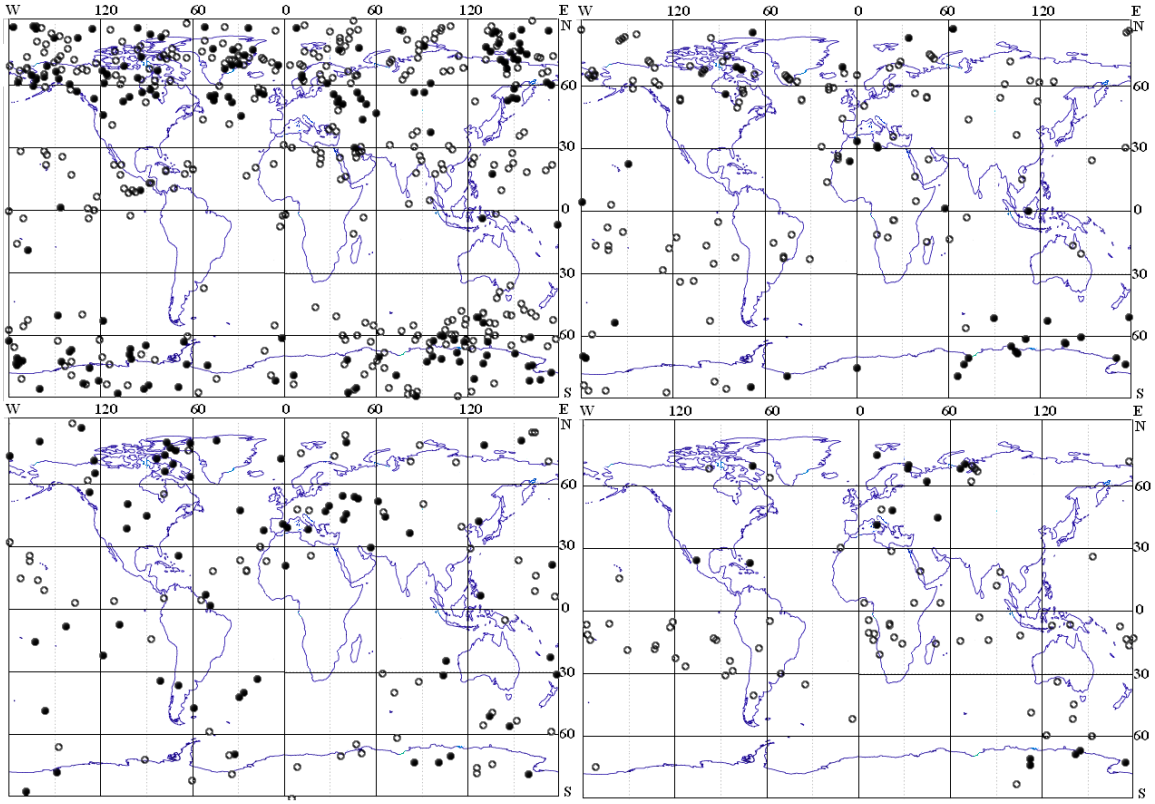

Fig. 4.4. Maps of intense ionospheric events with S_4 index greater than 0.12 for October 2001 (left top panel), October 2002 (right top panel), October 2003 (left bottom panel), and April 2004 (right bottom panel). The circles show the geographical position of the tangent point *T* (Fig. 1). The day-time events are marked by closed circles (local time 08–20 hours) and the night-time events are indicated by open circles (local time 20–08 hours).

The maximal number of events can be seen in May–July, October–December 2001 (Fig. 4.4, left top panel, Fig. 4.5, left and right top panels, respectively). The minimal number of events corresponds to October 2002 (right top panel in Fig. 4.4), and April and July 2004 (bottom right panels in Fig. 4.4 and Fig. 4.5, respectively). As seen in Fig. 4.4 and Fig. 4.5, the number of intense ionospheric events and their intensity decreases as time from May, July, and October 2001 to April–July 2004. This is possibly connected with a gradual diminishing in solar activity from maximal values in 2001 to minimal values in 2004.

DOI:10.2312/GFZ.b103-08040

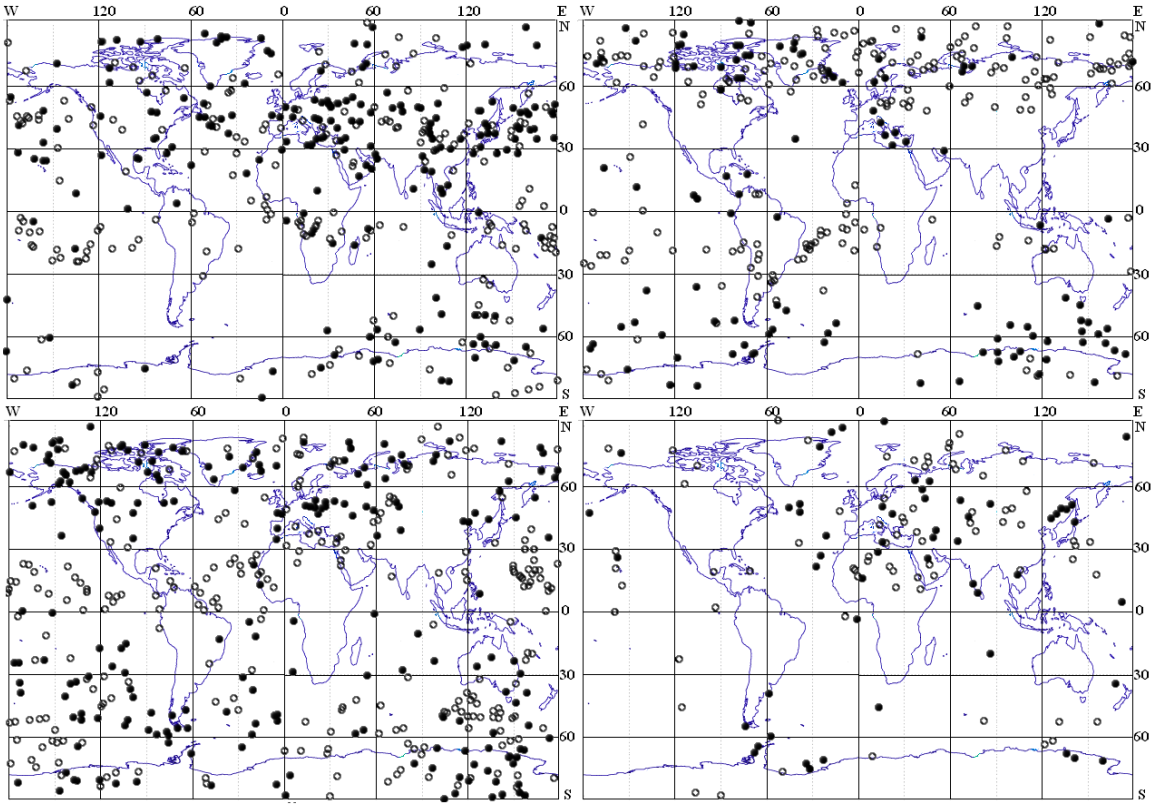

Fig. 4.5. Seasonal dependence of the global distribution of CHAMP RO events with intense amplitude variations (with magnitude of S_4 index greater than 0.2) for periods May 14-July 14, 2001, (left top panel), November-December 2001 (right top panel), October 28-November 26, 2003 (left bottom panel), July 2004 (right bottom panel). The day time events are marked by closed circles (local time 08-20 hours), the night-time events are indicated by open circles (local time 20-08 hours).

One can estimate the seasonal dependence in the geographical distributions of intense ionospheric events registered by the CHAMP satellite (Fig. 4.5). The seasonal displacement of the regions with intense ionospheric events in the south and north directions during the periods from May–July 2001 (Fig. 4.5, left top panel) to November–December 2001 (Fig. 4.5, right top panel), and to September 2001 (Fig. 4.4, left top panel) can be noted. The number of intense ionospheric events increases in the North Polar Region with latitudes greater than 60º N as the time changes from May–July 2001 to November–December 2001. Also the number of intense ionospheric events decreases at the moderate latitudes in the 30º – 60º N interval for the same time

DOI:10.2312/GFZ.b103-08040

interval. The possible cause of the seasonal dependence may be connected with two important mechanisms

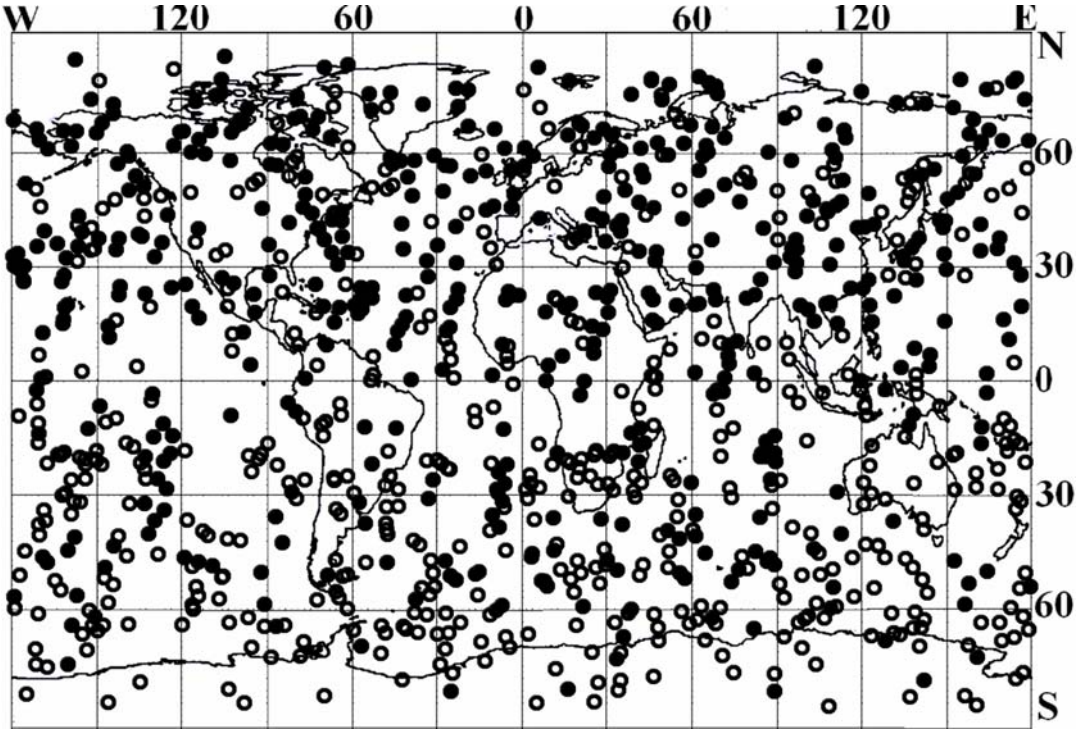

Fig. 4.6. Geographical distribution of FORMOSAT-3 RO events corresponding to June 01, 11, 12, 2007 (minimum of solar activity). The day time events are marked by closed circles (local time 08-20 hours), the night-time events are indicated by open circles (local time 20-08 hours).

governing the ionospheric disturbances. The first one is the ionizations caused by energetic electrons in the Polar Regions; the second is due to solar radiation. The influence of solar radiation has a seasonal character because ionization in the ionosphere follows annual and diurnal motion of the ionospheric sub-solar point. In Fig. 4.6 the geographical distribution of FORMOSAT-3 RO events corresponding to June 01, 11, 12, 2007 is indicated. In Fig. 4.7 the global distribution of FORMOSAT-3 RO events with intense amplitude variations (with magnitude of S_4 index greater than 0.24) for June 01, 11, and 12, 2007 (minimum of solar activity) is shown. It is clearly seen from comparison of Fig. 4.6 and Fig. 4.7 that the CHAMP RO events with strong scintillations mainly follow the tropical and moderate latitudes in the North Hemisphere, where the solar elevation angle is maximal. This indicates the solar

DOI:10.2312/GFZ.b103-08040

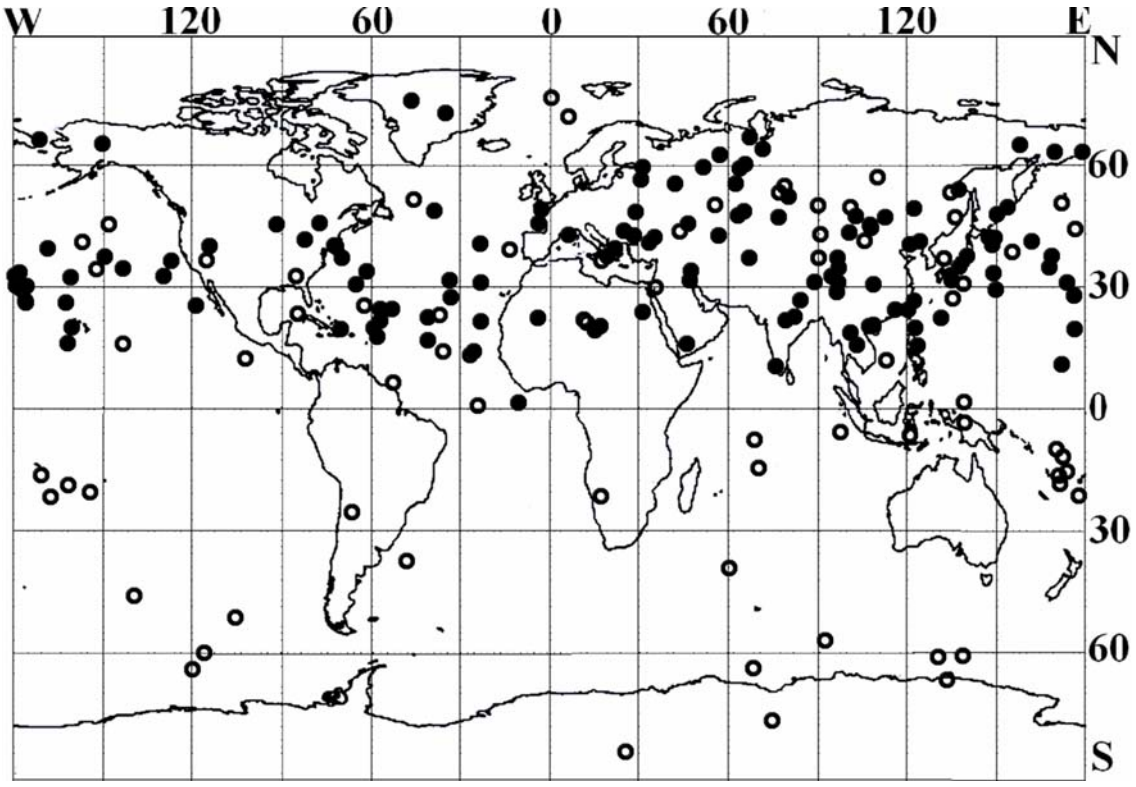

Fig. 4.7. Global distribution of FORMOSAT-3 RO events with intense amplitude variations (with magnitude of S_4 index greater than 0.24) for June 01, 11, and 12, 2007 (minimum of solar activity). The day time events are marked by closed circles (local time 08-20 hours), the night-time events are indicated by open circles (local time 20-08 hours).

ionization as the main factor for developing of sporadic E-layers in day time during the minimal level of solar activity. However the night scintillation events (Fig. 4.7) does not indicate direct connection with solar ionization.

As follows from this consideration, the amplitude part of the RO radio holograms is appropriate for studying the geographical and seasonal distributions of the ionospheric disturbances with global coverage and establishing their connections with solar activity.

DOI:10.2312/GFZ.b103-08040

CONCLUSIONS

High-precision and stable signals emitted by Global Positioning navigational System (GPS) satellites create favorable conditions both for radio holographic monitoring of the atmosphere and ionosphere as well as for investigation of the radio wave propagation effects in the trans-ionospheric satellite – to – satellite links.

1. Important connections between the phase and amplitude part of GPS radio-holograms as registered on board a LEO satellite are recovered. First of all the revealed connection between the phase acceleration and the refraction attenuation opens the way (1) to locate the layered structures in the atmosphere and ionosphere; (2) to separate effects of layers and irregularities in the RO signal; (3) to separate the effects of absorption and refraction attenuation in the RO measurements. Secondly a connection between the high-frequency parts in the variations of the refraction attenuation and phase path excess is revealed. This connection allows recalculating the normalized intensity variations to the phase path excess variations and vice versa. Both connections are validated by use of the CHAMP RO experimental data.

2. It is shown that the contribution of the lower ionosphere can be selected as the high-frequency part of the RO signal variations despite the many-times greater effect of the slow trend contribution of the upper ionosphere. This conclusion has been supported by analysis of the 684 CHAMP RO events. The offered technique of the analysis of the amplitude and phase data allows one to find out the weak sporadic layers in the ionosphere on a global scale and to define their characteristics.

3. New technique of the experimental determination of the IGW intrinsic frequency from the RO temperature or density (refractivity) vertical profiles is proposed for the case of positively identified wave that saturates via dynamical instability. The suggested method is most effective one in the case of low IGW frequencies ($\omega \sim f$), when

DOI:10.2312/GFZ.b103-08040

experimentally determined parameter a_e appreciably differs from unity. The analysis of RO data on the basis of the proposed method allows one to expand considerably the number of determined wave parameters. For example, it is possible to measure the IGW intrinsic frequency, the horizontal and vertical wind perturbations, vertical component of the kinetic momentum of IGW, i.e. parameters which are very important to study the energy and momentum vertical flow in the atmosphere.

4. Amplitude variations of the GPS occultation signals are very sensitive sensors and direct tool to study the internal waves in the atmosphere. The sensitivity of the amplitude method is inversely proportional to the square of the vertical period of the internal wave, indicating high sensitivity of the amplitude data to the wave structures with small vertical periods in the 0.8-4 km interval. In the first time in the RO practice examples of the internal wave breaking at the altitudes between 38 and 50 km are demonstrated. The introduced analytic method demonstrates its capability to retrieve the radio image of the internal wave – wave portrait using the amplitude data of the RO signals. The wave portrait can be restored using the Hilbert transform in the form of the analytic signal and contains the amplitude and phase of the internal wave as functions of the height. The analytic form of the internal wave presentation can be implemented in the case of GW for determining its intrinsic phase speed and the horizontal wind speed perturbations associated with the GW influence.

5. The amplitude GPS occultation method presents a possibility to obtain the geographical distribution and seasonal dependence of the atmospheric wave activity with global coverage. Asymmetry in the distribution of the wave activity at the 12 km level in the atmosphere is revealed. The maximal wave activity occurs in the summer polar region. At the 14 – 16 km levels, the wave activity is centered in the middle latitudes both in the Northern and Southern Hemisphere. At 18 – 20 km levels, most of

DOI:10.2312/GFZ.b103-08040

the internal wave's energy is concentrated in the equatorial areas. The local seasonal dependencies are clear for some regions, e.g. Siberia at the height of 14 km in the winter, owns a low wave activity and a high wave activity in the summer. Therefore, the amplitude method has a promise to be effective in investigating the climatology of the wave activity in very large height intervals in the upper troposphere and stratosphere.

6. RO signal variations are an indicator of plasma disturbances in the near-Earth space. An analysis of the histograms of the RO signal amplitude variations corresponding to the solar event October 29-31, 2003 indicates a possibility to introduce the RO index of ionospheric activity R_i, which is in good agreement with changes in the hourly index of *DST* related to the solar wind. This index can be introduced on the basis of the well-known index S_4, which is widely used as a measure of the amplitude of scintillations in the trans-ionospheric satellite-to-Earth links. The R_i index is equal to the ratio of the number of the RO events with the S_4 value, averaged at the altitudes above 40 km, and greater than the selected level, to the total number of RO events in the investigated area for a certain time interval (e.g., for a day). The maps of the geographical and seasonal distribution of the intense RO amplitude scintillations with high values of the index S_4, relevant to the time period May 2001-July 2004, indicate the areas with intense ionospheric disturbances and demonstrate the connection with solar activity. The analysis indicates the importance of GPS RO studies for revealing the interrelations between solar activity and natural processes in the ionosphere and mesosphere.

ACKNOWLEDGMENTS

We are grateful to the GeoForschungsZentrum Potsdam (Germany), NSPO (Taiwan) and UCAR (U.S.) for the provision of CHAMP and FORMOSAT-3 GPS RO data.

REFERENCES

Aarons J., Global Morphology of Ionospheric Scintillations, Proc IEEE, 70, 360-378, 1982.

Alexander, M. J., T. Tsuda, R. A. Vincent Latitudinal Variations Observed in Gravity Waves with Short Vertical Wavelengths, *J. Atmos. Sci,* V.59, 1394 1405, 2000.

Alexander, M. J., and K. H. Rosenlof, Gravity-wave forcing in the stratosphere: Observational constraints from the Upper Atmosphere Research Satellite and implications for parameterization in global models, *J. Geophys. Res.*, *108*(D19), 4597, doi:10.1029/2003JD003373, 2003.

Anthes, R. A., C. Rocken, and Y.-H. Kuo, Applications of COSMIC to meteorology and climate, *TAO*, **11**, 115-156, 2000.

Cot, C., and J. Barat, Wave-turbulence interaction in the stratosphere: a case study, *J. Geophys. Res., 91* (D2), 2749-2756, 1986.

Dunkerton, T. J., Inertia-gravity waves in the stratosphere, *J. Atmos. Sci., 41*, 3396-3404, 1984.

Eckermann, S. D., and P. Preusse, Global Measurements of Stratospheric Mountain Waves from Space, *Science* **286**, 1534-1537, 1999.

Eckermann S. D., I. Hirota, and W. A. Hocking, GW and equatorial wave morphology of the stratosphere derived from long-term rocket soundings. *Q. J. R. Met. Soc.*, **121.** 149-186, 1995.

Ebel, A., Contribution of GWs to the momentum, heat and turbulent energy budget of the upper mesosphere and lower thermosphere. *J. Atmos. Terr. Phys.* **46**, No. 9, 727-737, 1984.

Feng, D. D., and B. M. Herman, Remotely sensing the Earth's atmosphere using the Global Positioning System (GPS) – the GPS/MET data analysis, *J. Atmos. Ocean Technol.*, **16**, 990-1002, 1999.

Fritts, D. C., and M. J. Alexander, Gravity wave dynamics and effects in the middle atmosphere, *Rev. Geophys.,* **41**, **3**-1-**3**-64, 2003.

Fritts, D. C., and P. K. Rastogi, Convective and dynamical instabilities due to gravity motions in the lower and middle atmosphere: Theory and observations, *Radio Sci., 20* (6), 1247-1277, 1985.

Fritts, D. C., A review of gravity wave saturation processes, effects, and variability in the middle atmosphere, *PAGEOPH, 130,* 343-371, 1989.

Fritts, D. C., Gravity wave saturation in the middle atmosphere: A review of theory and observations, *Rev. Geophys. Space Phys., 22,* 275-308. 1984.

McFarlane, N. A., The effect of orographically excited gravity wave drag on the general circulation of the lower stratosphere and troposphere, *J. Atmos. Sci., 44,* 1775-1800, 1987.

Gardner, C. S., S. J. Franke, W. Yang, X. Tao, and J. R. Yu, Interpretation of gravity waves observed in the mesopause region at Starfire Optical Range, New Mexico: Strong evidence for nonseparable intrinsic (m, ω) spectra, *J. Geophys. Res., 103* (D8), 8699-8713, 1998.

Gorbunov, M. E., Gurvich, A. S., and A. V. Shmakov, Back-propagation and radio-holographic methods for investigation of sporadic ionospheric E-layers from Microlab-1 data, *Int. J. Remote Sensing, 23*(4), 675-685, 2002.

Hajj, G. A., and L. J. Romans, Ionospheric electron density profiles obtained with the global positioning system: Results from the GPS/MET experiment, *Radio Sci., 33*, 175–190, 1998.

Hajj, G. A., C. O. Ao, B. A. Iijima, D. Kuang, E. R. Kursinski, A. J. Mannucci, T. K. Meehan, L. J. Romans, M. de la Torre Juarez, and T. P. Yunck, CHAMP and SAC-C atmospheric occultation results and intercomparisons, *J. Geophys. Res.*, 109, D06109, doi: 10.129/2003JD003909, 2004.

Hajj, G. A., E. R. Kursinski, L. J. Romans, W. I. Bertiger, and S. S. Leroy, A Technical Description of Atmospheric Sounding by GPS occultation, *J. Atmos. Solar-Terr. Phys***.** V. 64, 451-469, 2002.

Heise, S., N. Jakowski, A. Wehrenpfennig, C. Reigber, and H. Lühr, Sounding of the Topside Ionosphere/Plasmasphere Based on GPS Measurements from CHAMP: Initial Results, *Geophys. Res. Lett.,* 29(2), 1699, doi:10.1029/2002GL014738, 2002.

Hocke, K., A. Pavelyev, O. Yakovlev, L. Barthes, and N. Jakowski, Radio occultation data analysis by the radioholographic method, *J. Atmos. Sol.-Terr. Phys., 61*, 1169-1177, 1999.

Hocke, K., and T. Tsuda, Gravity waves and ionospheric irregularities over tropical convection zones observed by GPS/MET radio occultation, *Geophys. Res. Lett.*, 28, 2815–2818, 2001.

Hocke, K., K. Igarashi, and A. Pavelyev, Irregularities of the topside ionosphere observed by GPS/MET radio occultation, *Radio Sci., 37*(6), 1101, doi:10.1029/2001RS002599, 2002.

Hocke, K. Igarashi, M. Nakamura, P. Wilkinson, J. Wu., A. Pavelyev, and J. Wickert, Global Sounding of Sporadic *E* Layers by the GPS/MET Radio Occultation Experiment, *J. Atmos. Sol.-Terr. Phys. 63*, 1973–1980, 2001.

Igarashi, K., A. Pavelyev, K. Hocke, D. Pavelyev, and J. Wickert, Observation of wave structures in the upper atmosphere by means of radio holographic analysis of the RO data, *Adv. Space Res.*, **27**, No. 6-7, 1321-1327, 2001.

Igarashi, K., A. Pavelyev, K. Hocke, D. Pavelyev, I.A. Kucherjavenkov, S. Matygov, A. Zakharov, and O. Yakovlev, Radio holographic principle for observing natural processes in the atmosphere and retrieving meteorological parameters from RO data. *Earth Planets Space*, **52**, 968-875, 2000.

Igarashi, K., A. Pavelyev, J. Wickert, K. Hocke, and D. Pavelyev, Application of radio holographic method for observation of altitude variations of the electron density in the mesosphere/lower thermosphere using GPS/MET radio occultation data, *J. Atmos. Sol. Terr. Phys., 64*, 959– 969, 2002.

Jensen, A. S., M. S. Lohmann, H. H. Benzon, and A. S. Nielsen, Full spectrum inversion of radio occultation signals, *Radio Sci.*, 38(3), L1040, doi:10.1029/2002RS002763, 2003.

Kelly, M. C. (1989), The Earth's Ionosphere, Int. Geophys. Ser., vol. 43, Elsevier, New York, 1989.

Kelley, M. C., V. K. Wong, G. A. Hajj, and A. J. Mannucci, On measuring the off-equatorial conductivity before and during convective ionospheric storms, *Geophys. Res. Lett.*, *31*, L17805, doi:10.1029/2004GL020423, 2004.

Kunitsyn, V. E., and E. D. Tereshchenko, Ionospheric Tomography, Springer Verlag Series: Physics of Earth and Space Environments, XII, pp 260, ISBN: 3-540-00404-1, 2003.

Lindzen, R. S., Turbulence and stress owing to GW and tidal breakdown. *J. Geophys. Res.* **86**, No. C-9, 707-714, 1981.

Kuo, Y.-H., S. Sokolovskiy, R. A. Anthes, and F. Vandenberge, Assimilation of GPS radio occultation data for numerical weather prediction, *TAO*, **11**, 157-186, 2000.

Liou, Y. A., A. G. Pavelyev, C. Y. Huang, K. Igarashi, and K. Hocke, Simultaneous observation of the vertical gradients of refractivity in the atmosphere and electron density in the lower ionosphere by RO amplitude method. *Geophys. Res. Lett.*, **29**, No. 19, 43-1 –43-4, 2002.

Liou, Y. A., A. G. Pavelyev, C. Y. Huang, K. Igarashi, K. Hocke, and S K. Yan, Analytic method for observation of the GW using RO data, *Geophys. Res. Lett.* **30**. 20. ASC 1-1 – 1-5, 2003.

Liou, Y. A., A. G. Pavelyev, J. Wickert, T. Schmidt, and A. A. Pavelyev, Analysis of atmospheric and ionospheric structures using the GPS/MET and CHAMP radio occultation database: a methodological review, *GPS Solutions*, v. 9, № 2, p. 122-143, 2005.

Liou, Y. A., A. G. Pavelyev, J. Wickert, S. F. Liu, A. A. Pavelyev, T. Schmidt, and K. Igarashi, Application of GPS radio occultation method for observation of the internal waves in the atmosphere, *J. Geophys. Res.*, *111*, D06104, doi:10.1029/2005JD005823, 2006.

Marquardt, C., and S. B. Healy, Measurement Noise and Stratospheric Gravity Wave Characteristics obtained from GPS Occultation Data, *J. Met. Soc. Jpn*, *83* (3), 417-428, 2005.

Martini, E., A. Freni, L. Facheris, and F. Cuccoli, Impact of tropospheric scintillation in the Ku/K bands on the communications between two LEO satellites in a radio occultation geometry, *IEEE Trans. Geosci. Remote Sens.*, vol. 44, no. 8, pp. 2063–2071, 2006.

Pavelyev, A., A. V. Volkov, A. I. Zakharov, S. A. Krytikh, and A. I. Kucherjavenkov, Bistatic radar as a tool for Earth investigation using small satellites, *Acta Astronautica.*, 39, 721–730, 1996.

Pavelyev A. G., A. I. Zakharov, A. I. Kucherjavenkov, A. I. Sidorenko, I. L. Kucherjavenkova, and D. A. Pavelyev : The features of propagation of radio wave reflected from terrestrial surface at small elevation angles on radio telecommunication link low orbital satellite-GEO, *J. Comm. Techn. and Electr*., V.42. No 1. P. 51-57, 1997.

Pavelyev, A. G., Y. A. Liou, C. Y. Huang, C. Reigber, J. Wickert, K. Igarashi, and K. Hocke, Radio holographic method for the study of the ionosphere, atmosphere

and terrestrial surface from space using GPS occultation signals. *GPS Solutions*, No. 6, 101-108, 2002.

Pavelyev, A. G., T. Tsuda, K. Igarashi, Y. A. Liou, and K. Hocke, Wave structures in the electron density profile in the ionospheric D and E-layers observed by radio holography analysis of the GPS/MET radio occultation data, *J. Atmos. Solar-Terr. Phys***,** V. 65, No.1, 59-70, 2003.

Pavelyev, A. G., J. Wickert, T. Schmidt, V. N. Gubenko, S. S. Matyugov, and A. A. Pavelyev, *Radio* holographic methods for atmospheric, ionospheric and stratospheric waves, 94pp., Scientific Technical Report STR04/18, GFZ Potsdam, Germany, 2004.

Pavelyev, A. G., K. Igarashi, C. Reigber, K. Hocke, J. Wickert, G. Beyerle, S. Matyugov, A. Kucherjavenkov, D. Pavelyev, and O. Yakovlev, First application of radioholographic method to wave observations in the upper atmosphere. *Radio sci., 37*(3), 15-1 –15-11, 2002.

Pavelyev, A. G., Y. A. Liou, and J. Wickert, Diffractive vector and scalar integrals for bistatic radio holographic remote sensing, *Radio Sci.,* **39**(4), RS4011, 1-16, doi:10.1029/2003RS002935, 2004.

Pavelyev, A. G**.**, J. Wickert, Y. A. Liou, Ch. Reigber, T. Schmidt, K. Igarashi, A. A. Pavelyev, and S. S. Matyugov, Different mechanisms of the ionospheric influence on GPS occultation signals, *GPS Solutions*, V.9, № 2, p. 96-104, 2005a.

Pavelyev, A. G., J. Wickert, T. Schmidt, Ch. Reigber, S. S. Matyugov, A. A. Pavelyev, Y. A. Liou, and K. Igarashi, Effect of Solar Activity in Late October 2003 on Radio Occultation Signals from the CHAMP German Satellite *Geomagnetism and Aeronomy*, V. 45, No. 1, pp. 134–139, 2005b.

Rabiner L. and B. Gold, Theory and Application of Digital Signal Processing, Prentis Hall, 1978.

Reigber, C., H. Lühr, P. Schwintzer, and J. Wickert (Eds.), Earth Observation with CHAMP: Results from Three Years in Orbit, Springer, Berlin, Heidelberg New York, ISBN 3-540-22804-7, 2005.

Schreiner, W. S., S. V. Sokolovskiy, C. Rocken, and D. C. Hunt, Analysis and validation of GPS/MET radio occultation data in the ionosphere, *Radio Sci.*, *34*(4), 949–966, 1999.

Senft, D. C., and C. S. Gardner, Seasonal Variability of Gravity Wave Activity and Spectra in the Mesopause Region at Urbana, *J. Geophys. Res., 96,* Sept. 20, 17,229-17,264, 1991.

Sokolovskiy, S., W. Schreiner, C. Rocken, and D. Hunt, Detection of high-altitude ionospheric irregularities with GPS/MET, *Geophys. Res. Lett., 29*(3), 1033, doi:10.1029/2001GL013398, 2002.

Squires, G. L., *Practical Physics*, 246 pp., McGraw-Hill, London, 1968.

Steiner, A.K., and G. Kirchengast, GW spectra from GPS/MET occultation observations. *J. Atmos. Ocean. Tec.,* **17**, 495-503 (2000).

Tsuda, T., M. V. Ratnam, P. T. May, M. J. Alexander, R. A. Vincent, and A. MacKinnon, Characteristics of gravity waves with short vertical wavelengths observed with radiosonde and GPS occultation during DAWEX (Darwin Area

Wave Experiment), *J. Geophys. Res.*, *109*, D20S03, doi:10.1029/2004JD004946, 2004.

Tsuda, T., M. Nishida, C. Rocken, and R. H. Ware, A global morphology of GW activity in the stratosphere revealed by the GPS occultation data (GPS/MET). *J. Geophys. Res. 105*, 7257-7273, 2000.

Tsuda, T., and K. Hocke, Vertical wave number spectrum of temperature fluctuations in the stratosphere using GPS occultation data. *J. Met. Soc. Jpn.*, **80**, No. 4B, P. 228-241, 2002.

Vorob'ev, V. V., A. S. Gurvich, V. Kan, S. V. Sokolovskiy, O. V. Fedorova, and A. V. Shmakov, Structure of the Ionosphere from the radiooccultation GPS-''Microlab-1'' satellite data: Preliminary results, *Earth Obs. Remote Sens.*, 15, 609– 622, 1999.

Wang, L., M. A. Geller, and M. J. Alexander, Spatial and Temporal Variations of Gravity Wave Parameters. Part I: Intrinsic Frequency, Wavelength, and Vertical Propagation Direction *J. Atmos. Sci.*, 62, 125–142, 2005.

Ware, R., M. Exner, D. Feng, M. Gorbunov, K. Hardy, B. Herman, Y.-H. Kuo, T. Meehan, W. Melbourne, C. Rocken, W. Schreiner, S. Sokolovskiy, F. Solheim, X. Zou, R. Anthes, S. Businger, and K. Trenberth, GPS soundings of the atmosphere from low earth orbit: Preliminary results, *Bull. Am. Meteor. Soc.*, **77**, 19-40, 1996.

Wickert, J., C. Reigber, G. Beyerle, R. König, C. Marquardt, T. Schmidt, L. Grunwaldt, R. Galas, T. K. Meehan, W. G. Melbourne, and K. Hocke, Atmosphere sounding by GPS radio occultation: First results from CHAMP, *Geophys. Res. Lett.*, *28*(17), 3263– 3266, 2001.

Wickert J., A. G. Pavelyev, Y. A. Liou, T. Schmidt, C. Reigber, K. Igarashi, A. A. Pavelyev, and S. S. Matyugov, Amplitude scintillations in GPS signals as a possible indicator of ionospheric structures, *Geophys. Res. Lett.*, 31(24), L24801 doi:10.1029/2004GL020607, 1-4, 2004a.

Wickert J., O. I. Yakovlev, A. G. Pavelyev, S. S. Matyugov, L. N. Samoznaev, and V. A. Anufried, Ionospheric Fluctuations of Decimetric Radio Waves Along Satellite-to-Satellite Paths, *J. Comm. Tech. and Electr.*, 49(10), pp 1109-1116, 2004b.

Wu D. L., C. O. Ao, G. A. Hajj, M. de la Torre Juarez, and A. J. Mannucci, Sporadic E morphology from GPS-CHAMP radio occultation, *J. Geophys. Res.*, *110*, A01306, doi:10.1029/2004JA010701, 1-18, 2005.

Yeh, K. C., and C. H. Liu, Radio wave scintillations in the ionosphere, *Proc. IEEE*, 70(4), 324–360, 1982.

Yizengaw, E., M. B. Moldwin, P. L. Dyson, and T J. Immel, Southern Hemisphere ionosphere and plasmasphere response to the interplanetary shock event of 29–31 October 2003, *J. Geophys. Res.*, 110, A09S30, doi:10.1029/2004JA010920, 2005.

Yizengaw, E., M. B. Moldwin, A. Komjathy, and A J. Mannucci, Unusual topside ionospheric density response to the November 2003 superstorm, *J. Geophys. Res.*, 111, A02308, doi:10.1029/2005JA011433, 2006.